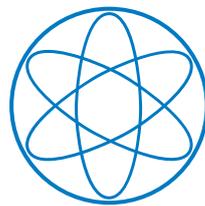# Technische Universität München

Physik Department E20

Molecular Nanoscience and Chemical Physics of Interfaces

Hexagonal Boron Nitride Monolayers as Templates for Molecular Nanostructures

Dissertation

Sushobhan Joshi

Technische Universität München

Lehrstuhl E20 - Molekulare Nanowissenschaften und Chemische Physik von Grenzflächen

Hexagonal Boron Nitride Monolayers as Templates for Molecular Nanostructures

Sushobhan Joshi

Vollständiger Abdruck der von der Fakultät für Physik der Technischen Universität München zur Erlangung des akademischen Grades eines Doktors der Naturwissenschaften (Dr. rer. nat.) genehmigten Dissertation.

Vorsitzender: Prof. Dr. Björn Garbrecht

Prüfer der Dissertation: 1. Prof. Dr. Wilhelm Auwärter

2. Priv.-Doz. Dr. Friedrich Esch

Die Dissertation wurde am 01.09.2017 bei der Technischen Universität München eingereicht und durch die Fakultät fur Physik am 09.10.2017 angenommen.

To my family

Contents

Contents

List of Figures

Abstract

This thesis is a detailed story of boron nitride (BN) grown on a Cu(111) single crystal surface and the studies of organic molecules on it. The results can be summarized in four segments in this thesis, comprising of the growth of BN on Cu(111), study of porphine molecules on BN/Cu(111), film of oligophenylenes on BN/Cu(111) and finally metal coordination of the oligophenylenes on the model substrate. As the first part, atomically thin sheet of BN was grown successfully on Cu(111). Using a scanning tunneling microscope (STM), the ultrathin sheet was demonstrated to be a topographically planar but with a periodic modulation of surface potential, making the spacer-layer a unique electronically corrugated model template. For the second part, the template property of the BN was demonstrated by depositing increasing coverage of porphine molecules on BN. The porphines not only organize on the two-dimensional periodic array on BN, but also demonstrate their electronic gap tunability, a feature assigned to the modulation of surface potential of the BN. Further, a film of oligophenylenes namely quaterphenyl dicarbonitriles was studied on the BN substrate. This highly ordered layer of the molecules demonstrates not only the surface induced spatial modulation of the conductance but also variations in a second level vibronic conductance. For the last part, cobalt coordination of the oligophenylenes were studied on BN. Originally studied on metal surfaces for growing metal-organic framework, the linker molecules form a four-fold coordination motif on BN, illustrating the validity of a previous density functional theory prediction. Alongside, the molecules also demonstrate a model bistable switch mechanism.

1 Introduction

1.1 Nanotechnology

The world of nanotechnology is still very much in its infancy as we are still struggling to understand the intrinsic properties of matter at this scale. It has been an ultimate desire for mankind to comprehend and control matter towards the fabrication of artificial devices for future applications. This is however quite challenging as matter exhibits strikingly different properties at the nanoscale ($1nm = 1 \times 10^{-9}\,m$) as compared to the bulk state. Gold (Au) for instance has been a highly treasured coinage metal for millennia due to its superior malleability, inertness and attractive shiny yellow luster. However, the same metal exhibits catalytic activity, nonmetallic behavior and wine red to violet color when reduced to nanoclusters. [1] In a recent publication, it was even reported to have record high catalysis when reduced to clusters at picoscale ($1pm = 1 \times 10^{-12}\,m$). [2] Therefore, the pursuit of broader understanding of the nature of materials and proper establishment of their fundamentals at the atomic and molecular level is an ongoing process today. The formularies mankind had amassed as scientific knowledge so far needs to be rewritten.

For the past few decades in the semiconductor industry, ever growing demand for high-speed information processing and high-density storage of data has contributed to significant miniaturization of fabricated structures in devices. The traditional means of achieving such tiny structures (for e.g. 22 nm transistors, source: www.intel.com) is the top-down approach of lithography, which is on the verge of its physical limits. However, an alternative solution had already been suggested in 1959 by Feynmann in his clichéd "There's Plenty of Room at the Bottom" talk, where he advised a bottom-up approach of manipulation and control of "things at small scale" for information storage. The notion thus suggests the design and fabrication of further miniaturized structures are possible by using minute atoms and molecules as building blocks in the bottom up approach. For comprehension, an analogy would

be the building of a complex structure using various Lego blocks in children's play. This new endeavor can be considered the dawn of nanotechnology.

1.2 The advent of scanning tunneling microscope

In a true sense, the era of nanotechnology began only in the early 1980s when Binnig and Rohrer invented the scanning tunneling microscope (STM) at the IBM lab in Zurich. This is a powerful machine with imaging and characterization capabilities of objects as minute as atoms and molecules. After the famous publication of atomic resolution in a Si(111)-7x7 reconstruction [3], the STM then onwards has been established as a paramount tool for study and manipulation of systems at the nanoscale, leading nanoscience and applications. For instance, the STM was later used to move single atoms to create artificial quantum coral structures [4] and inducing chemical reactions [5] on surfaces. However, such labor intensive manipulation techniques are good for the understanding and experimental demonstration of physical phenomenon only. Also from the aspect of ease of experimental reproduction as well as potential manufacturability, control of the molecular and atomic building blocks need to be at a much greater mesoscopic scale. In order to truly fabricate artificial structures for applications, an alternative solution needed to be found. It was quite a challenge to devise a strategy for creating well-ordered arrays of nanostructures on a surface, built from desired atoms and/or functionalized molecules. And the answer lay in biology, where mother nature has been utilizing a fascinating *self-assembly* process to fabricate natural structures for 'devices' for her own creation: life. Since the big-bang of life on earth, organic molecules have been assembling into a broad variety of complex structures like that of proteins, DNA, lipid membranes etc., [6] formulating the diversity in life itself from simple microbes to something as complex as the human brain. Mimicking the self-assembly process in nature, innumerous studies have been done in chemistry, biology and material science. With a greater understanding of the phenomenon and the advent of STM, significant interest therefore to apply it for fabrication of novel technologies has been triggered; utilizing specifically designed molecules with functional properties along with atoms. As a result, using self-assembly protocols, tremendous progress towards further understanding and growth of molecular nanostructures of various configurations on surfaces has been made. [7, 8]

1.3 Self-assembly and the role of the substrate

On a surface, specifically designed organic molecules are used as tectons (build-ing blocks) to fabricate the desired artificial structures. Under thermodynamic equilibrium, when these tectons are deposited on a surface, they adsorb and or-ganize spontaneously into unique 2-D structures and patterns. [7] The self-assembly processes are usually driven by reversible non-covalent inter-molecular interactions: electrostatic forces like π-π interactions, van der Waals forces and hydrogen bond-ing. However, from an application perspective, such weakly bound structures are fragile and undesirable. In order to make the acquired structures robust, the metal-coordinated assembly has attracted great attention for some time. This incorporates the use of the tectons with specifically designed terminations that bond with transi-tion metal atoms like iron (Fe), [9–11] copper (Cu), [12–14] cobalt (Co) [15–17] and recently also a lanthanide cerium (Ce) etc. [18] Significant progress has also been made towards the fabrication of self assembled structures through stronger covalent bonding. However, the success has been only limited to smaller local scale. [19, 20]

So far, the major focus had been only in the supramolecular chemistry of the func-tionalized molecules and/or the metal atoms in use. Nevertheless, an essential goal of the self-assembly studies is also to establish the fundamental properties of the ingredients (molecules, atoms) involved and their interaction with the environment (substrate and co-adsorbates). So far most studies using STMs with cryogenic ultra-high vacuum (UHV) systems have been done on metal surfaces due to various rea-sons like the structural homogeneity (single crystals), ease of repeated cleaning (via sputtering techniques) and to promote catalytic activities. However, a major dis-advantage of using metal crystals as substrates is the strong adsorbate-substrate interaction which might bring an electronic as well as a conformational change in the subject probed. Therefore, most experiments related to the construction of 2-D supramolecular architectures are conducted on coinage metal (Ag, Cu and Au) substrates [8] which are relatively inert.

An important aspect of the establishment of self-assembly protocols is the inter-molecular interaction, which too is eclipsed by the strong influence of the metal support. So for a holistic characterization, it is necessary to conduct the supramolec-ular science on a platform which decouples the adsorbates from the metal and is at the same time compatible with the state-of-the art nanotechnology instrumentation (STM). Therefore, various insulating spacer-layers that reduce molecule-metal sub-

strate interaction like alkaline halides, [21, 22] oxides, [23] graphene [24–26] and recently boron nitride [27–29] have been reported. Nonetheless, most of these epitaxially grown ultrathin layers have inherent drawbacks like strong polarity, non-planarity and inhomogeneity.

1.4 Boron nitride monolayers as substrates

Atomically thin boron nitride (BN) grown epitaxially and studied on several transition metals has been demonstrated as a promising new breed of ultrathin insulating layers. Its diverse topographical features on these non-noble transition metals make it lucrative as substrate or template for supporting various adsorbates [24, 27–30] or other 2D sheet materials like graphene. [31–36]

In this thesis, a detailed STM study of the growth and properties for the BN on a metal surface Cu(111) is presented. As shown in our recent publication, the ultrathin layer exhibits a rather unique, topographically planar, but electronically corrugated feature on Cu(111). [37] Apart from being an interesting spacer-layer to study inherent characteristics of organic molecules the BN/Cu(111) itself has a periodically modulated surface potential, which is observed in the STM images as contrast invertible moiré patterns of various sizes or periodicities. This provides an interesting landscape for studying the behavior of organic molecules under such environment. Next, a detailed study of free-base porphine (2H-P) on BN/Cu(111) is presented where we show how a molecule divulges its true character when placed on such a distinctive substrate as compared to the adsorption on metal surfaces like Ag(111) and Cu(111). We demonstrate confined growth of 2H-P nanostructures on BN proving the spacer-layer as a special template for assembly of molecules. Furthermore, ditopic linear quaterphenylene dicarbonitrile molecules were studied on the BN surface. The molecules were already previously studied on Ag(111) and exhibit interesting porous networks both with/without metal-coordination. Following the same protocol on BN it is found that the quaterphenylenes exhibit non-planarity on the insulating layer and form a metal-ligand framework with an additional binding motif to a cobalt atom, corroborating a previous DFT prediction. [16] Furthermore, for all the molecules mentioned above, the inhomogeneous BN template also induces an intriguing 2D modulation of the energy of unoccupied and/or occupied molecular orbitals.

1.5 Layout of thesis and author contribution

This thesis will continue along the following layout:

In Chapter 2, fundamental concepts and theory of the main tool scanning tunneling microscopy used in the research will be briefly discussed. This will be followed by the brief theory of scanning tunneling spectroscopy which is a powerful complementary tool of the STM that enables a deeper understanding of the electron density, charge distribution, interaction of the molecule with each other, substrate etc. Basics of field emission resonances will also be discussed briefly, which is an important tool to empirically measure and compares spatial workfunction differences on the surface.

In Chapter 3, concise description of the experimental setup, mainly the STM, its different components and a special description of the main precursor material borazine will be made. Alongside, sample preparation for the experiments, including BN growth will be briefly discussed.

Chapter 4 is based on published paper Joshi *et al.*, Nano Lett. 2012, 12, pp 5821–5828 and deals with details of growth and characterization of BN on Cu(111). The BN was demonstrated as unique topographically planar but electronically corrugated surface. This is the foundation work of the whole thesis where subsequent chapters will be follow-up research advancements. All experiments, analysis and conclusions drawn from this work described in the chapter were conceived, conducted and written by our research group at E20, Physik Department, Technische Universität München. The author of the thesis was the main research Ph.D. candidate for the project. Complementary theoretical calculations of this work were done by partners in Physikalisch-Chemisches Institut, Universität Zürich under Chair of Professor Jürg Hutter.

Chapter 5 is based on published paper Joshi *et al.*, ACS Nano, 2014, 8 (1), pp 430–442 and deals with control of molecular organization and energy level alignment of free-base porphine molecules on the BN monolayer. It offers details of how the BN offers an interesting templating and band-gap tunability property to adsorbates on it. Like in Chapter 4, the author was the main Ph.D. researcher for the project. The same partners at Universität Zürich contributed to the complementary theoretical calculations.

Chapter 6 is based on published paper Palma, C., Joshi, S. *et al.*, Nano Lett., 2015, 15 (4), pp 2242–2248 and deals with studies of conjugated oligophenylene film on BN.

The story of two level spatial modulation of vibronic conductance observed in the molecules on BN is described here in detail. The author of this thesis was again the main Ph.D. researcher carrying out the main experimental and analytical work while guiding an undergrad student Tobias Hoh in his supervision. Extensive theoretical simulations and calculations that advanced the work further to the level published in the above-mentioned paper were done by Dr. Carlos-Andres Palma at E20. Both Dr. Palma and the author have been mentioned as an equally contributing author in the paper.

Chapter 7 represents a draft manuscript (in preparation) Joshi *et al.* It describes metal-coordination, characterization and model functionality study of the oligopheny-lene molecule on BN. The author of the thesis was again the main research Ph.D. candidate for the project. Complementary theoretical calculations of this work were done by collaborator Dr. Jonas Björk in Department of Physics, Chemistry and Biology, IFM, Linköping University, Sweden.

Chapter 8 is a segment dedicated to conclusions and perspectives for further research on the field related to studies of BN and molecules on it.

The author has also contributed significantly in other research projects including studies of Functionalized Pyrene molecules on metal and BN. This work is published as paper Kaposi, T., Joshi, S. *et al.*, ACS Nano, 2016, 10, 7665-7674. This is however not included as a part of this thesis. Furthermore, several other contributions from the author have resulted in published papers listed in the List of Publications section at the end of the thesis.

2 Scanning Tunneling Microscopy and Spectroscopy

The concept of an STM was presented to the world by the team of Binnig and Rohrer at IBM Zurich in 1981. [38] Subsequently, they demonstrated atomic resolution of metal surfaces along with answers to complex physical questions, [3, 39] demonstrating the true capabilities of the STM. The technique comprises of an atomically sharp tip brought to a distance $z \leq 10$ Å from a surface in order to probe the physical properties of atoms or molecules on the surface. The probe is piezoelectrically positioned in three dimensions, normally comprising a ratio between the piezoelectric bias voltage and expansion of $\sim 1\,V$ and ~ 10 Å. Of course, this ratio is temperature dependent and can vary slightly with variations in it. In this way, it is used to scan along a two-dimensional grid and the information collected can be processed into an image. To extract the information of the object while scanning, the STM uses the tunneling effect to acquire a current between a sharp tip and the sample. And, the current is generated when a bias voltage is applied between the two electrodes (tip and sample). By coupling the piezoelectric tip control to the measured current, the microscope can be operated in two modes - the constant current and the constant height mode.

As demonstrated in the schematic sketch in Figure 2.1a, scanning along the x-axis parallel to the periodically varying metal surface induces a corresponding periodic variation of the tip-sample height z in the constant current mode. This is recorded as a change in voltage applied to the piezos. The voltages are then processed into topographic profiles in STM images (Figure 2.1a*). In this case a feedback loop is implemented that applies a regulating voltage to a piezo mechanism to alter the tip-surface height thus maintain the contant current. However, the variations in tip height are not only topography but also enfluenced by the electronic structure of the tip and sample (for more details, see section 2.1, *vide infra*). In contrary, a periodical variation of the current is recorded in the constant height mode (Figure

2.1b). Variations in tunneling current are processed into surface profiles (Figure 2.1b*). In fact, this mode is appropriate for imaging clean, flat and smooth surfaces due to a higher risk of tip crashing into the surface. In this mode, a feedback loop is opened to maintain a constant tip-surface height z. A full image is attained once sub-sequential line scans cover every lateral position x, y at respective height z.

This chapter gives a concise information of the theoretical aspects of the STM along with spectroscopy. For a more detailed study of the theories associated with the STM, readers are advised to consult the references. [40–42]
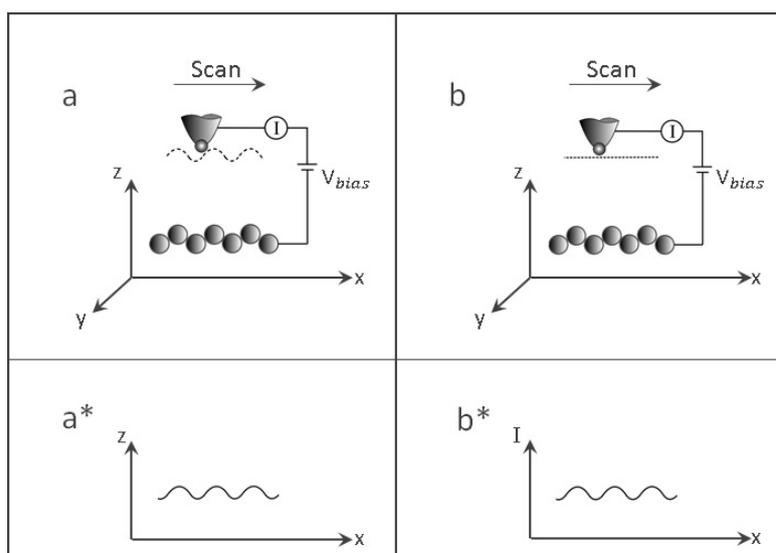
Figure 2.1: Schematic sketch of the operating concept of an STM. (a) Scanning in the constant current mode and (b) the constant height mode. Sketches (a*) and (b*) show the corresponding modulation plots.

2.1 Quantum tunneling

What happens if some hungry mice face a high wall as a barrier between them and cheese? Well, they try to dig a tunnel in the wall to get to the cheese (see Figure 2.2). Provided that the wall is not so 'thick' and that the mice are 'determined', a few of them might indeed succeed in tunneling through. This is analogous in the case of electrons as well. Generally, at the presence of conducting physical media, electrons flow easily with the application of a small bias voltage between two electrodes. But when a barrier like a vacuum is present in between, the energy required for electrons

to cross the barrier is higher than the potential of the barrier itself. Only upon exceeding the required potential of the barrier, can electrons propagate forward and this regime of election exiting from an electrode is known as field emission in Physics. In our analogy with the mice above, the 'height' of the wall can be compared to the potential of the barrier and the 'determination' of the mice as the applied bias.

Fortunately, in quantum mechanics exists a phenomenon known as quantum tunneling in which, when the two electrodes are brought extremely close together, there is a viable possibility for the electrons to tunnel through the barrier without having to exceed the barrier potential. A significant role in the electron propagation through the barrier thus is played by the gap between the two electrodes; needless to say the thinner the gap, better the chances of tunneling. This, in our mice analogy again can be seen as when the thickness of the wall is small enough, determined mice can dig a 'tunnel' through the wall to reach the cheese, without having to surmount the high wall. This will be elaborately explained using schematics a rectangular potential barrier in following section (*vide infra*).
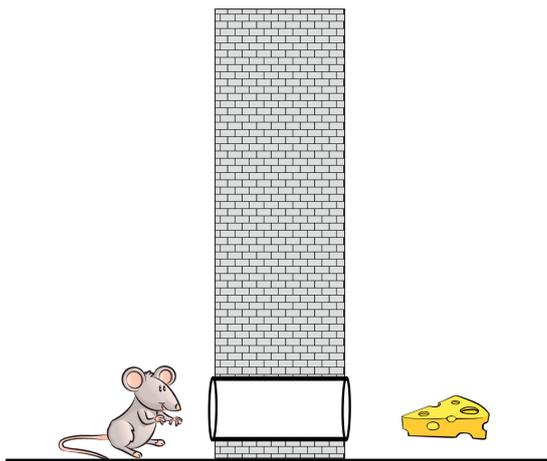
Figure 2.2: The concept of tunneling. A mouse can dig a tunnel right through a wall that prohibits it from getting to a cheese.

In classical mechanics, the energetics of any particle is represented as $E_{tot} = E_{pot} + E_{kin}$. As it is quite evident from the equation, it is impossible for the particle to overcome a potential barrier which is higher than its total energy. This means that the particle would need to have a negative kinetic energy in order to surmount the barrier, which is impossible ($\because E_{kin} \geq 0$). However, from the dawn of quantum mechanics, it was understood that an electron has a wave-particle duality and its

wave function $\Psi(x)$ has a nonvanishing probability to exist in the forbidden regions of the barrier. In essence, a particle can tunnel right through the potential barrier. Schematically, if we consider a rectangular potential barrier (illustration Figure 2.3a) with width d, an incident particle wave Ψ_o (black wave left of the barrier) doesn't abruptly end but exponentially tapers off (red curve). However, when the wave Ψ_o encounters a thin barrier with width d^*(in the range of some angstroms) some of the particles can indeed get transmitted through the barrier, resulting in a wave Ψ_T (blue wave, Figure 2.3b) even though the energy of the particle is too small to overcome the barrier.

a b
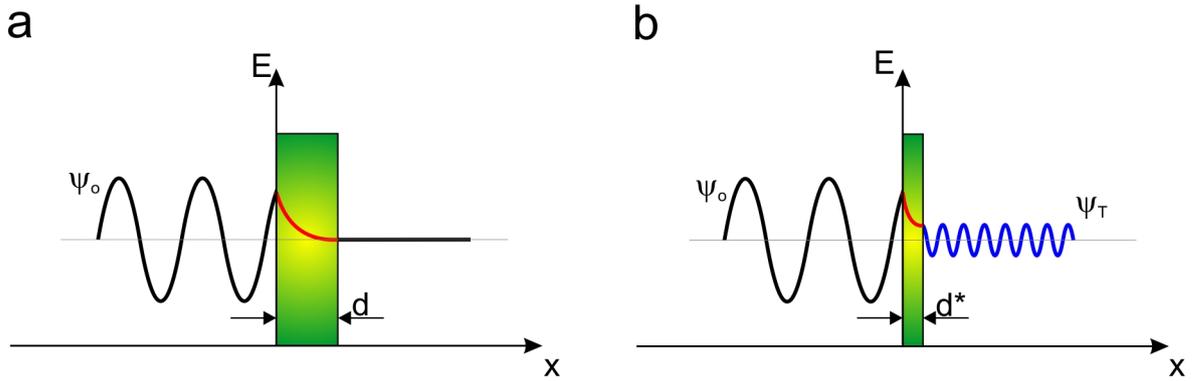
Figure 2.3: Schematics of tunneling. (a) A thick rectangular potential barrier with width d. The incoming particle wave dissipates within the barrier. (b) When the barrier is thin enough with width $d*$, there is a chance for the particle wave to be transmitted.

The wave nature of the quantum mechanical particle (electron in our case) is described by the Schrödinger equation shown below.

$$-\frac{\hbar^2}{2m}\frac{d^2}{dx^2}\Psi(x) + U(x)\Psi(x) = E\Psi(x) \tag{2.1}$$

Here $\hbar$ is the reduced Planck constant, U is the potential of the barrier, m and E are the mass and energy of the electron respectively. For a case without significant barrier to overcome $(E > U)$ the solution to the equation is given by

$$\Psi(x) = \Psi(0)\,e^{\pm i\frac{\sqrt{2m(E-U)}}{\hbar}x} = \Psi(0)\,e^{\pm ikx}, \tag{2.2}$$

where k is the wave vector and $\Psi(0)$ the wave function at $x = 0$. However, in case of classically forbidden regions with an insurmountable potential barrier $(U > E)$, the solution can be written as

$$\Psi(x) = \Psi(0)\, e^{-\frac{\sqrt{2m(U-E)}}{\hbar}x} = \Psi(0)\, e^{-kx} \qquad (2.3)$$

Herewith, the probability P of finding the electron in the forbidden zone is non zero as depicted by the following equation.

$$P = \mid \Psi(x) \mid^2 = \mid \Psi(0) \mid^2 e^{-2kx} \qquad (2.4)$$

According to the equation, along with a finite possibility for the electron's presence in the barrier, it also shows that the probability decays exponentially in the barrier along the positive x-direction. This also implies that when the barrier is thin enough, the electrons are likely to tunnel through the barrier to the other side (electrode). In an STM perspective, the two ends of the barrier are the two electrodes (tip and sample) separated by very narrow space (vacuum) or liquid (in a solid-liquid STM) and the barrier height is given by the workfunctions; Φ_t and Φ_s for the tip and sample respectively. When a bias voltage U_b is applied an energy $E = eV$ is provided to the electrons. When a sufficient bias voltage is applied $(U_b \gg E)$ and also $(\Phi \gg eV)$, tunneling can occur from tip to sample or vice-versa, depending on the polarity of the applied bias voltage. Under the circumstance, the probability of an nth state electron existing in the energy range between the Fermi level E_F and $E_F - eV$ to successfully tunnel through the barrier (sample to tip) is

$$P_n(x) = \mid \Psi_n(x) \mid^2 = \mid \Psi_n(0) \mid^2 e^{-2\frac{\sqrt{2m\Phi}}{\hbar}x} \qquad (2.5)$$

The tunneling current I is then in essence proportional to the summation of all electronic states Ψ_n existing in the energy range E_F to $E_F - eV$.

$$I \propto \sum_{E_F - eV}^{E_F} P_n(x) = \sum_{E_F - eV}^{E_F} \mid \Psi_n(x) \mid^2 = U_b \rho_s(0, E_F)\, e^{-2\frac{\sqrt{2m\Phi}}{\hbar}x} \qquad (2.6)$$

here ρ_s is the local density of states (LDOS) of the sample at $x = 0$. It is quite evident from the above equation that the tunneling current is directly dependent on the LDOS as well so an STM image is not purely topographic information but a

convolution of electronic states as well. On the other hand, the equation also depicts exponential decay with the tip sample distance (represented by x). This means that for the change of an angstrom (Å) in the tip-sample distance, the tunneling current changes by roughly an order of magnitude. This gives an STM the kind of sensitivity necessary to probe objects as small as atoms.
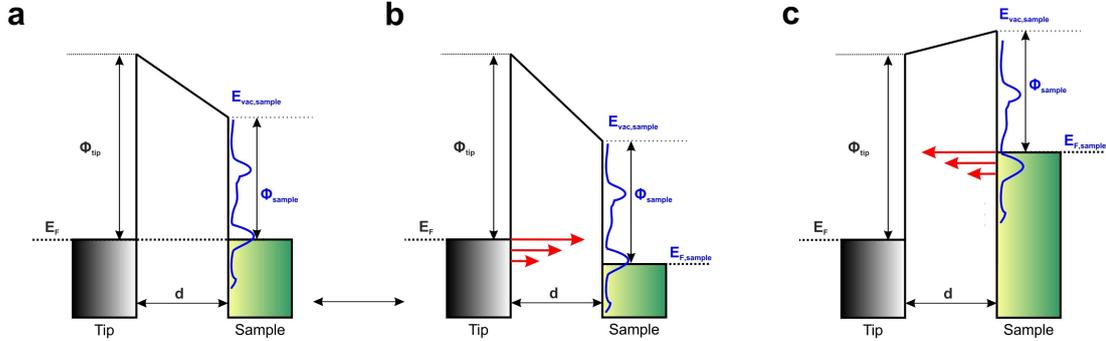
Figure 2.4: Energy level diagrams at the tip-sample interface separated by the vacuum potential barrier. Energy level diagrams at the tip-sample interface separated by the vacuum potential barrier. (a) Tip and sample are connected with no potential difference and only separated by a small vacuum gap. The corresponding Fermi levels are aligned and the sample vacuum level $E_{vac,sample}$ is lowered forming a trapezoidal barrier shape. (b) Induced by the application of positive bias voltage, $U_b > 0$, with the ground at the tip, electrons tunnel from occupied states of the tip to unoccupied states in the sample. (c) The application of negative bias, $U_b < 0$, reverses the process. The contributing electron energy states to the current flow are indicated by the colored vectors with their length being proportional to the electrons energy and to the transmission probability Γ.

A proper illustration of the process is schematically shown in Figure 2.4. In Figure 2.4a, the tip and the sample are in thermodynamic equilibrium with the distinctive alignment of the tip and sample Fermi levels. A total separation of the tip and sample would lead to a vacuum level alignment of the tip and sample. However, upon bringing the two electrodes close together, an electronic contact of the tip causes the separation of the vacuum levels $E_{vac}(t)$ and $E_{vac}(s)$. No bias voltage is applied in this case and the barrier width (d) is substantially small to allow tunneling.

The application of a positive bias voltage tunes the interface structure (Figure 2.4b), causing a lowering of the sample Fermi level $E_{F,sample}$, and concomitantly the sample vacuum level, by the net bias voltage $|eV|$. As discussed above, only electrons with

energies $E_F - eV$ and E_F can contribute to the tunneling process. In this case, the electrons tunnel from occupied states of the tip to unoccupied states in the sample.

At negative bias, $E_{F,sample}$ is shifted upwards and thereby reversing the process. The electrons tunnel from occupied states of the sample to unoccupied states of the tip. Since the electrons for the tunneling exist in the range from $E_F - eV$ to E_F, electrons with energy states near the Fermi level of the electrode from which the electrons tunnel have a higher energy and are likely to contribute to the tunneling current. In Figures 2.4b and c, the tunneling direction is indicated by the vectors colored in red for both $U_b > 0$ and $U_b < 0$ with their length shown proportional to the transmission probability Γ(*vide infra*, equation 2.12).

The equation above (2.6) for the tunneling current is, however, a rather simple model, as for example the real (complex) geometry of a tip is neglected. A better model to describe the tunneling mechanism is based on the Bardeen formalism [43] wherein independent wave functions for tip Ψ_t and sample Ψ_s are taken into account. Along with that a tunneling matrix element M_{ts} is included that connects the two wave functions and describes overlap of them departed by a surface S in the barrier. Herewith, the tunneling current from tip to sample states can be written as:

$$I = \frac{2\pi e}{\hbar} \sum_{t,s} f(E_t) \left[1 - f(E_s + eV)\right] \mid M_{ts} \mid^2 \delta(E_t - E_s) \qquad (2.7)$$

where the $\delta-$function ensures the energy conservation, including the elastic processes only. Here the $f(E)$are Fermi functions of quantum state energy level E and the Fermi level E_F with $f = 1/(1 + exp(E - E_F)/kT)$. And, the tunneling matrix (as shown by Bardeen) can be given by following expression integrated over the separation surface S of the barrier with infinitesimally small surface element dS.

$$M_{ts} = \frac{\hbar^2}{2m} \int_S \left(\Psi_t^* \nabla \Psi_s - \Psi_s \nabla \Psi_t^*\right) dS \qquad (2.8)$$

Now, when the Fermi functions are replaced by unit step functions (approximation to their zero temperature expression) for small voltage U_b the tunneling current expression can be written as

$$I = \frac{2\pi e^2 U_b}{\hbar} \sum_{t,s} \mid M_{ts} \mid^2 \delta(E_t - E_F) \delta(E_s - E_F) \qquad (2.9)$$

This was further adapted by Tersoff and Hamann [44, 45] in 1983 where they evaluated the matrix element for the tip and sample wave functions. They assumed an s-wave spherical tip with radius R and the same workfunction Φ for both the tip and sample. And for small voltage bias U_b and the matrix element is proportional to the amplitude of Ψ_s and the tip is at a distance r_o from the sample; the tunneling current forms as

$$I \propto U_b e^{2kR} \rho_t \left(E_F\right) \rho_s \left(r_o, E_F\right) \tag{2.10}$$

or

$$I \propto U_b \sum_s \mid \Psi_s \left(r_o\right) \mid^2 \delta \left(E_s - E_F\right) \propto LDOS_s \left(r_o, E_F\right) \tag{2.11}$$

Here, the expression shows how the tunneling current is proportional to the bias voltage U_b, the tip sharpness and their the importance in lateral resolution (as the center of tip lies at a distance $R + d$ above the sample), the tip sample distance d and finally the LDOS of the tip and importantly the sample. In this model, the above expression signifies that a constant current STM micrograph corresponds to a surface of constant DOS at E_F, thereby making the STM image a convolution of topographic as well as electronic information as mentioned before.

As this thesis mainly deals with the growth and characterization of insulating BN monolayer on Cu(111) and later the study of adsorbates on it, a brief insight into the imaging and tunneling process through an insulator is presented. At first, one may think that it would be impossible to image an insulating object atop a metal surface, owing to the poor contribution of the insulator to the LDOS. This contributes to the transparency of the insulator. But when they are ultrathin films (up to only a few layers) insulators have to considered as one more barrier layer; after all the vacuum itself is an insulator. For successful imaging of any insulating layer one strategy is to apply a significantly high bias voltage. This facilitates the electrons to tunnel into the conduction band of the insulator, probing the density of states. Another strategy, especially for a submonolayer coverage, may be to tunnel into the image states through which the contrast between the insulating island and the metal substrate underneath can be tuned.

2.2 Scanning tunneling spectroscopy

The model above is still crude as in real STM measurements, the tip sample separation is so small that their wavefunctions cannot be considered as independent. This would only be true for the approximation of this approach with large tip-sample gap d. Also, the simplistic spherical s-wave model of the tip needs to be updated to a more realistic tip structure. This was done by Chen [46] by including d and p states which corresponds better to the d-band W, Pt-Ir metal tips in actual STM measurements. Nevertheless, as the tunneling is limited to the E_F, the energy dependence of the tunneling current can not be extracted from it. But the dependence of the tunneling current on the LDOS of the sample gives us a possibility to extract spectroscopic information on the local electronic structure of the sample. For this the tunneling expression of the Tersoff-Hamann approach can be generalized by including several different states lying between the eV and E_F. In essence, the tunneling current is acquired with integration of both tip and sample density of states over energy range covered by applied bias voltage V. Furthermore, the expression is complimented with the tunneling transition probability Γ. This transition probability is dependent on factors like barrier gap d, energy of the electron E, bias voltage V, workfunctions of the tip and sample Φ_t & Φ_s respectively. [47]

Overall, Γ is given as:

$$\Gamma = exp\left(-2d\sqrt{\frac{m}{\hbar^2}}\sqrt{\Phi_t + \Phi_s - 2E + eV}\right) \tag{2.12}$$

Finally, the tunneling current can be expressed as:

$$I \propto \int_0^{eV} \rho_s\left(E\right)\Gamma\left(E, eV, d\right) dE \tag{2.13}$$

From the equation above, simply taking a voltage derivative of the tunneling current gives a differential conductance: [48]

$$dI/dV = \rho_s\left(eV\right)\Gamma\left(eV\right) + A\left(V\right) \tag{2.14}$$

Thus the dI/dV is directly dependent on the LDOS of the sample and Γ. The additional term $A(V)$ describes the voltage dependence of the transmission function

Γ.To further cancel out tip-sample variations and energy dependent transmission dependencies, the dI/dV is normalized by dividing by I/V.

$$\frac{dI/dV}{I/V} \propto \rho_s\left(eV\right) \tag{2.15}$$

In practice, to characterize the distribution of the local density of states of the sample in a quantitative way, the differential conductance as a function of the applied bias V can either be acquired by numerically differentiating I/V or by recording the dI/dV in an STM using a lock-in detection technique. This is known as scanning tunneling spectroscopy (STS). The numerical differentiation technique is not so popular due to a limited signal to noise ratio. On the other hand, using a lock-in amplifier increases the ratio significantly; thus facilitating faster data acquisition and reduced impact of tip drift problem. The tip is kept at a constant height by switching the feedback loop off while the tip makes voltage scan across the sample.This also has an advantage as it allows atomic scale lateral-dependent spectroscopy.

The dI/dV information harnessed from points in a two-dimensional grid of a surface can also be plotted to create differential conductance maps. Of course, in this case, the measurement has to be set at a fixed voltage. This yields rich spatially distributed information of the sample.

Another method of STS is to keep the feedback loop on and move the tip in the z direction (varying the tip-sample distance d) during the measurement. In essence, the tip is made to approach really close to the sample and by gradually increasing the tip-sample distance, dI/dz is measured. This is a constant voltage mode and the exponential variation of the tunneling current is recorded in the process. At the low voltage limit, equations 2.12 and 2.13 are simplified to

$$I \propto \rho_s\left(E_F\right)exp\left(-2d\sqrt{\frac{m}{\hbar^2}}\sqrt{\Phi_t + \Phi_s}\right) \tag{2.16}$$

From the above expression it is evident that the current I depends on the tip and sample workfunctions $\Phi_{t,s}$.

$$\frac{dI/dz}{I} \propto \sqrt{\frac{2m}{\hbar^2}\left(\frac{\Phi_t + \Phi_s}{2}\right)} \tag{2.17}$$

The expression above shows how the local workfunctions of the two electrodes can

be extracted with the method. [49] Moreover, as the workfunction of the tip is considered to be constant the dI/dz spectroscopy is useful to empirically measure the local workfunction of a sample.

2.3 Field emission resonances

For measuring a system over significantly high voltage ($V \geq \Phi$), field emission resonances (FER) can be used as a probe. This technique is especially suitable for characterizing insulating layers with less contribution to the LDOS. Generally, it is a constant current mode where the STM feedback loop is kept active and the tip probes a point on the sample for voltage range up to 10 V. As the bias voltage rises, the tip-sample distance increases by the help of the feedback loop to maintain the constant current. When the applied bias voltage is higher than the average workfunction, the energy region above vacuum level becomes accessible. This phenomenon is known as field emission and the electrons do not need to undergo the tunneling process. Under such circumstances, a triangular quantum well is formed in the tunneling junction. This can be seen in the schematic sketch (Figure 2.5a) as sharp valley formed between the dotted black line and its junction at the sample. However, due to the presence of image charges for both tip and sample at this voltage range, the shapes of the quantum wells are distorted mainly in the regions near the boundaries as shown by the curved solid black line in Figure 2.5a. Alongside, the electrons trapped in the quantum well behave like free particles and are scattered by the sample tunneling junction. This then acts like a resonator where the incident and reflected electron waves form standing wave patterns due to quantum interference. Only standing wave pattern oscillations with small state number n are affected by the distortion of the barrier at the sample junction (*vide infra* for details).

In a numerical expression, the voltages for the resonances is given by: [50]

$$V_n = \Phi + (\frac{\hbar\pi}{\sqrt{2me}}\frac{3}{2}F)^{2/3}n^{2/3} \tag{2.18}$$

where Φ is an average of the tip and sample workfunctions, n is a quantization number and F is the strength of local electric field ($F = V/d$). The tip sample separation is given by d. We can simply write the above equation further as:

$$V_n = \Phi + \alpha F^{2/3} n^{2/3} \tag{2.19}$$

where $\alpha = 4.39 V^{1/3} \mathring{A}^{2/3}$ is a constant. It is noteworthy that the images states are dependent on the workfunction Φ. Therefore the FERs can be used to extract information on the local workfunctions in a sample. An example is shown in Figure 2.5b where the FERs on h-BN and Cu(111) are shown as orange and black spectra respectively. The spectra show sharp peaks for various quantization numbers. However, the peaks' energy positions are different due to variation in the workfunction of the two different surfaces. A successive plot (Figure 2.5c) of Energy (eV) versus $n^{2/3}$ shows two different datasets for the two surfaces. It has to be noted that the first few points in the plot originate from the barrier height modified (distorted) regions, contributing to nonlinear fit of the plots. However, latter points are from the normal triangular well and exhibit linear increments with the quantization numbers n. The linear segments of both the curves can be extrapolated to intercept the ordinate (Energy) and thus the disparity of the workfunction of the metal and the insulator can be estimated.
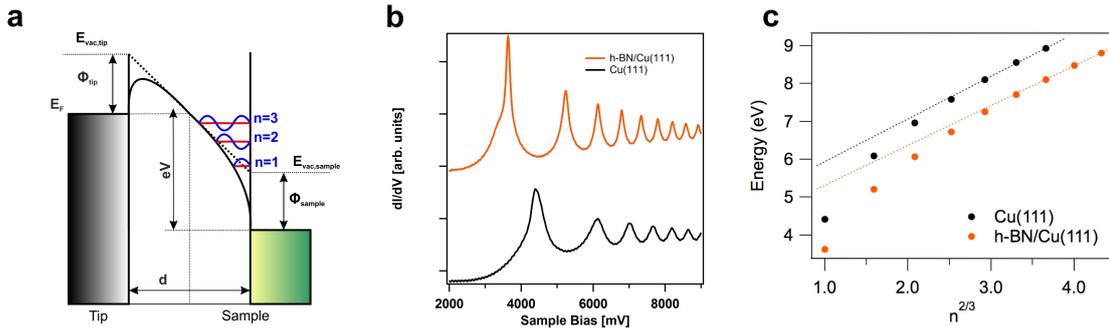
Figure 2.5: Field emission resonances. (a) Energy diagram showing the creation of triangular potential well formed in vacuum. The electrons trapped in the potential well form distinct quantized resonances. (b) Differential conductance spectra taken on BN and Cu(111) exhibit the FERs with their characteristic resonance peaks and shifts. (c) The energy of each resonances plotted against $n^{2/3}$ results in characteristic linear distribution for both BN and Cu(111). The first few points on the plot are non-linear due to the curvature in the junction of the potential well.

3 Experimental Setup

All experiments conducted during the research leading to this thesis were done at the low-temperature STM lab in Garching, where a commercial Createc machine ($www.lt-stm.com$) operating under ultra-high vacuum (UHV) and 6 K is installed. The machine is constantly operated and maintained at a base pressure of about $1x10^{-10}$ mbar to keep the sample as clean as possible. In order to achieve stability and sub-molecular resolution of adsorbates probed, the sample is cooled to such low temperatures. The whole setup is mounted on four vibration dampers so that the system is decoupled from external vibrations. In this chapter, a basic introduction to the main components of the STM is provided.

3.1 The Createc low temperature STM

The STM can be nicely seen in Figure 3.1 where all the main components of the machine are highlighted by numbers and in a color coded depiction. 1) Various pumps setup to maintain UHV are shown in purple. 2) & 3) The main housing of the machine is parted by a gate valve where two separate vacuum chambers are maintained. One of them is called the STM chamber (yellow) which houses the STM. To support the UHV in this chamber an ion getter pump is installed. The other chamber is used for preparing the samples and is therefore called the Preparation chamber (shown in blue). This chamber also houses the main pumps responsible for maintaining the UHV of the whole machine. As the name suggests, this chamber houses other essential units necessary for cleaning the sample substrates and depositing the adsorbates on it. Further, the section also contains a parking lot to hold different sample holders for various metal single crystals and spare tips. 4) To control and transfer the samples, a manipulator arm enters the Preparation chamber at the end opposite to the STM chamber. The manipulator is shown in the figure as green. The arm can be moved along its long axis to bring the sample in and out of the

STM chamber. For manipulation of the sample within the Prep. chamber, the arm can also move in two perpendicular directions in a plane normal to the long axis. 5) A cryostat needed to cool the system to low temperatures are shown in red. 6)The four vibration dampers that carry the whole machine is shown in orange. These are based on a pneumatic system to isolate the system from external vibrations. In order to achieve a noise free measurement and to further isolate the setup from external vibrations, the scanner is hung on springs (see schematics in Figure 3.2). Also in measurement position, it is stabilized by an eddy current damping mechanism.
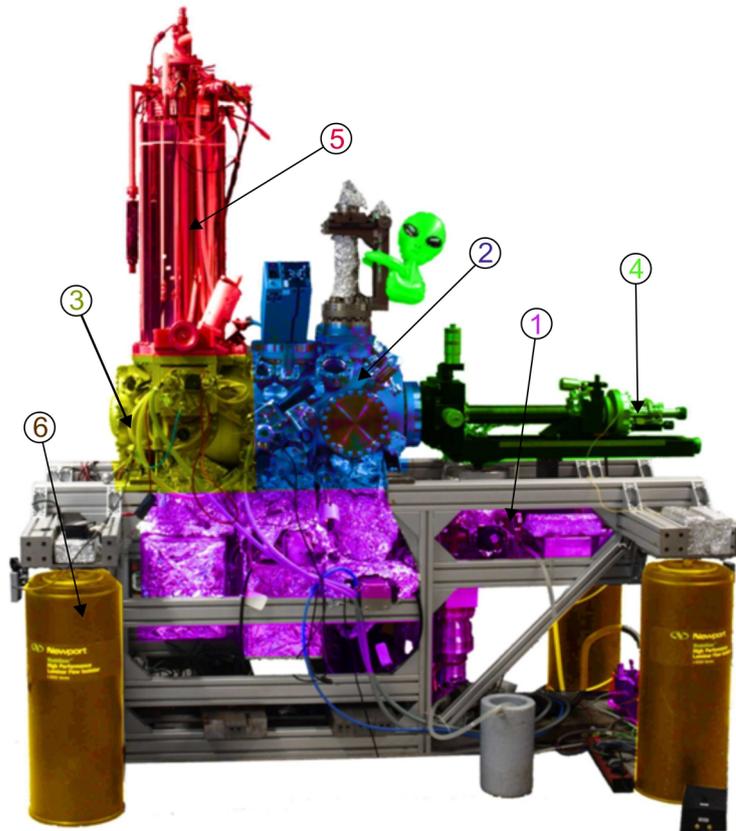
Figure 3.1: The Createc low temperature STM. (1) represents pumping system, (2) preparation chamber, (3) STM chamber, (4) the manipulator, (5) cryostat and (6) vibration dampers. Image courtesy: Dr. Knud Seufert.

3.2 Cryogenic system

To have a stable sample (without thermal vibrations and diffusion) the sample needs to be cooled. For that, a bath cryostat maintained at 6 K is mounted above the STM

chamber (see Figure 3.2). A sample also needs to be brought in thermal equilibrium with the cryostat in order to take stable STM measurement and also to avoid piezo drift during measurement. The cryostat is basically composed of two concentric cylinders isolated by UHV (see schematic Figure 3.2). To maintain the operating temperature the cryostat is filled with liquid helium (purple) in the inner cylinder. But to minimize the consumption of the expensive liquid helium, a second stage cooling is done by filling the outer cylinder with liquid nitrogen (blue).The UHV isolation between the two cylinders prevents possible thermal transport through convection. The sample and the scanning unit is then in contact with the liquid helium chamber via cables connecting them. This ensures a direct conduction cooling of the sample to liquid helium temperature.
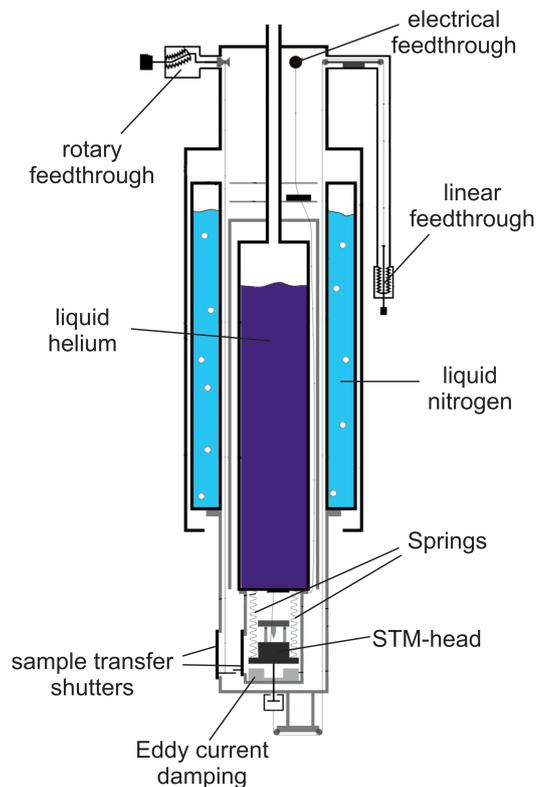
Figure 3.2: Schematic diagram of the cryostat and STM. The purple cylinder and the outer blue cylinder of the cryostat are filled with liquid helium and liquid nitrogen respectively. The STM-head hangs with springs and is in conductive contact with the inner liquid helium cylinder. Various feedthroughs are also shown. Adapted from dissertation: [51]

3.3 Pumping system

Any surface is prone to attract adsorbates very quickly. For instance, a clean surface is covered by gas molecules and other contaminants within 3 seconds at 1 x 10^{-6} mbar. [52] On the other hand, sensitive measurements with adsorbants as small as atoms and molecules mandate a clean surface. Therefore the sample preparation and measurement is conducted under UHV. For this, a series of pumps are implemented in the STM. First, the chamber is connected to a rough vacuum rotary pump that decreases the system pressure to about 1 mbar. This low pressure is a prerequisite to sustaining a turbo molecular pump which then reduces the pressure further to the 10^{-6} mbar range. This fore vacuum is then converted to the UHV of range 10^{-10}mbar with a powerful second turbo molecular pump directly connected to the Preparation chamber. Complementarily, there are two ion getter pumps installed in both the chambers. These pumps provide a further reduction in pressure and are effective in maintaining a low pressure even when the turbo pumps are switched off. For further improvement, especially before a sample preparation, a titanium sublimation pump and a cooling trap are installed. An additional cerium evaporator is also present in the Preparation chamber. These are also useful to deposit the Ce metal atoms for self-assembly purposes when needed. But once operated, the cerium coats the chamber walls and aids in reducing the pressure further.

3.4 Preparation chamber and supporting systems

The Preparation chamber is basically a UHV room in the STM set for cleaning the crystals and depositing the adsorbates to be studied. For the purpose, several instruments necessary are installed in it. Foremost, to clean the sample, an ion gun that uses argon gas to sputter the crystal is present. There are also leak valves that are used to have controlled inlet of other gases and vapors required for preparing a sample. Borazine, which is a precursor vapor necessary for growing the BN monolayers relevant for this thesis is also deposited through such a leak valve *(vide infra)*. A movable parking platform is present in the Preparation chamber where unused sample crystals and spare tips are parked. Additionally, a mass spectrometer is also installed in order to monitor and analyze the residual gas in the chamber. For depositing metal atoms and other desired molecular adsorbates on the sample, some molecular beam evaporators and organic molecular beam evaporators

(OMBE) are installed. The OMBE comprises of three heatable quartz crucibles to store depositable molecules and a metal filament setup to deposit metal atoms.

3.5 STM chamber and scanner setup

The STM chamber houses an STM scanner and an in situ OMBE. However, the main component of the STM chamber is the STM scanner (Figure 3.3). This alone is the necessary unit required to scan and acquire data from the sample. It consists of a base-plate (Figure 3.3a) that holds three outer piezos with sapphire spheres each at their top. On top of the three piezos spheres resides an approach-plate with three distinct ramps cut in it. Each of the ramp covers 120° of the approach-plate's circumference and has a 2° inclination of their bottom profile (see Figure 3.3a). The three sapphire spheres touch a ramp each. At the center of the approach-plate is a central inner piezo that is attached to the STM tip.
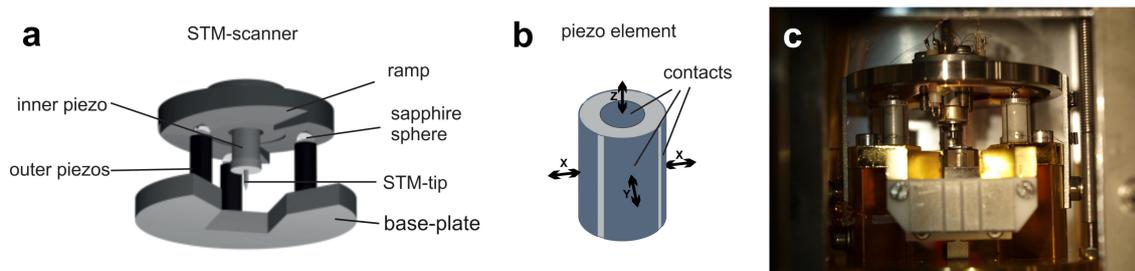
Figure 3.3: The STM scanner. (a) Schematic figure of the STM scanner with base-plate and three outer piezos (black cylinders) with sapphire spheres on top. Inner piezo holds STM tip and is located at center of the top approach-plate. (b) The piezo element with six electrical contacts that allows actuation in all six directions. (c) A photograph of the STM scanner setup. A sample holder is already placed on the base-plate. Adapted from dissertation: [53]

The piezo elements have the special property of controlled contraction and expansion when a voltage is applied. This property of the piezos is the reason behind the precision of motion and controlled maneuverability of an STM tip. As seen in the Figure 3.3b the piezo tubes have four external and an inner section. The external sections provide motion in x and y directions upon application of a voltage via contact electrodes and the inner cylinder contact is used to control the motion in z direction. In the STM scanner, the three outside piezos are used to approach

the tip to the sample. This is why they are called coarse piezos as well. Once in the tunneling regime, the inner piezo is then used to have precise lateral as well as vertical movement during the scan. The sample holder (Figure 3.3c) stays underneath the tip in close proximity. For this, the sample holder is placed on a rectangular table that sits under the base-plate which is in thermal contact the cold liquid helium container. Finally, the STM measurements can begin after the steady state cold temperature has been reached.

3.6 Sample preparations

Cleaning metal single crystals

The work involved in this thesis is beased on growth of BN as a substrate grown on a Cu(111) surface and two different organic molecules studied on it. In either case, the metal crystal had to be cleaned thoroughly before every sample preparation. It is done by sputtering the metal crystals using a sputter gun and argon gas. The argon gas is fed through a leak valve into the chamber at a pressure of 2.5 x 10^{-5}mbar. The ion gun ionizes the gas when subjected to 800 V and the Ar+ is bombarded into the sample usually for 30 minutes. During the bombardment, the adsorbates on the surface are removed; but alongside the metal atoms on the surface are also removed and the surface roughness is increased. Therefore although free of adsorbates the sample surface profile is full of bombardment holes. To make the surface smooth again the sample is annealed around 725 K. This allows the surface atoms to diffuse around the surface and aids in the recovery of the surface smoothness.

Hexagonal boron nitride

Like in the isomorphs of carbon, BN is known to have various crystalline entities e.g. amorphous, hexagonal, cubic (diamond like) and wurtzite lattices. In bulk state, hexagonal BN (h-BN, see Figure 3.4) has a structure similar to that of its carbon based analogue: graphite. In Figure 3.4a we see how the h-BN sheets are stacked together with van der Waals forces. Individual monolayers of both h-BN and graphite (graphene) are two-dimensional layers with a hexagonal honeycomb lattice as seen in Figures 3.4b-c. Instead of carbon atoms in the graphene, BN h-BN monolayers have alternating boron and nitrogen atoms in the lattice.
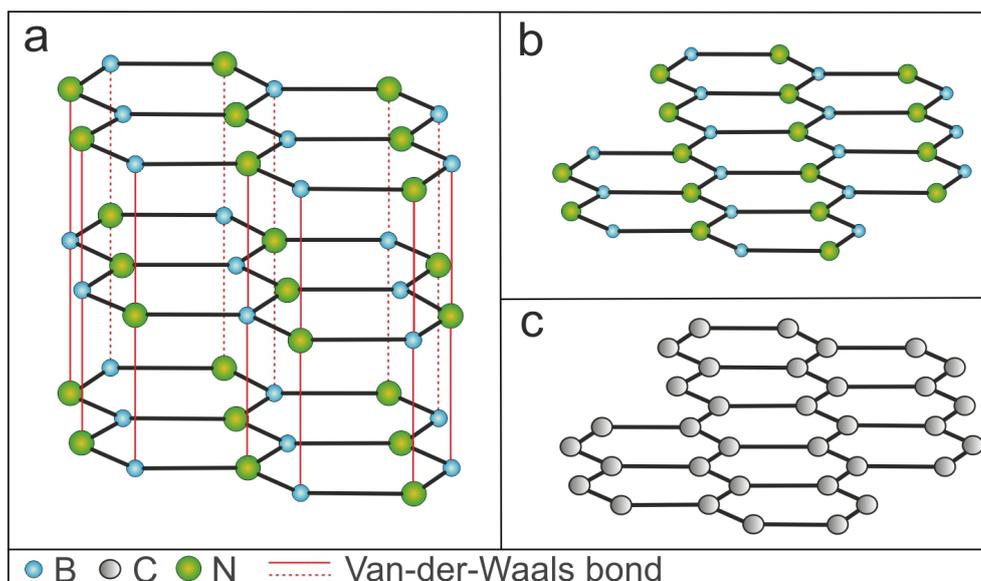
Figure 3.4: BN analogy to graphene. (a) Like in graphite, the BN monolayers stacked together by van der Waals bond. (b & c) Close resemblance of the two materials, both sp^2 bonded 2-D monolayers. graphene is composed of only carbon atoms instead of alternating boron and nitrogen atoms.

Growth of BN

The BN monolayers were grown and extensively characterized on a Cu(111) surface using benzene like borazine (HBNH)$_3$ as a precursor material. Borazine is a cyclic compound as seen in Figure 3.4a composed of alternating boron (blue) and nitrogen (green) atoms, terminated by hydrogens (white). BN was grown following a chemical vapor deposition (CVD) method described by Nagashima *et al.* [54] and Auwärter *et al.* [55] where the borazine vapor was released into the preparation chamber around the partial pressure of 1 x 10^{-6} mbar for a few minutes. The sample (Cu(111) crystal) temperature for the preparation were maintained in the range of 983 K to 1120 K. The duration of the borazine deposition depended on the coverage of BN desired. For instance, at a 40 L dosage (*Langmuir* = 1 x 10^{-6} torr s), we got only under 0.5 % coverage whereas, for a full coverage, we need to dose around 800 L. The BN film is synthesized when the precursor borazine reacts with hot metal substrate wherein the terminal hydrogens are released and the nascent borazine rings merge to form a continuous film (Figure 3.4a, underneath).
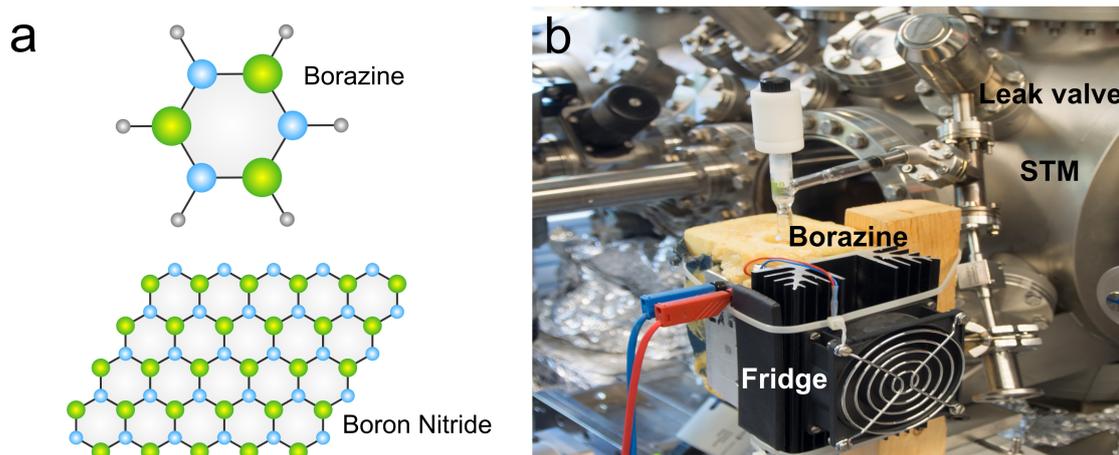
Figure 3.5: Borazine setup. (a) Single borazine molecule with alternating boron (blue sphere) and nitrogen (green sphere). Underneath a BN sheet after the CVD of borazines. (b) Experimental setup of borazine deposition. Borazine is stored in the hermetically sealed tube cooled with a home built fridge. The borazine dosed via a leak valve connected to the preparation chamber of the STM.

To expose the Cu(111) surface to the borazine, a leak valve as shown in Figure 3.5b is used. To prevent unwanted polymerization of the precursor material, it is stored in a hermetically sealed tube. It is also kept cold by cooling it with a home built fridge as shown above. The borazine is cleaned with a few cycles by freezing the liquid material (using liquid nitrogen) and pumping the vapor out using an external pumping station. Finally, the film is grown by exposing the vapor to a Cu(111) annealed at around 983 K and above (upto 1120 K) temperature in the preparation chamber. In our observation, the quality of the BN were better with preparations at higher sample temperatures.

The film growth rate decreases sharply once a full monolayer has been achieved. This is caused by a strong reduction of the surface reactivity for borazine towards a BN surface as compared to a hot metal surface. The BN is an insulating and chemically inert ultrathin layer. Thus the CVD of borazine to produce BN monolayers is a reliable quasi-self terminating preparation method.

Deposition of adsorbates

Once the metal sample has been cleaned and/or coated by BN monolayer, organic molecules and metal atoms were deposited on the sample for the following investigations. The molecules are housed in quartz crucibles in the OMBE. Before depositing the molecules on the surface, it is important to degas the crucibles for some time

(up to a few hours) in order to remove unwanted contaminants that generally reach sublimation temperature earlier than the actual molecules. Finally, the molecules are heated via resistive heating to their sublimation temperatures and are allowed to sublime out of the crucibles. The sample is placed in a position facing the OMBE so that the molecules flying out of the OMBE are adsorbed on the sample surface. For this, the sample is usually held at ambient temperature or lower (as specified in corresponding chapters). For deposition of metal atoms, desired metal wires are wound around a heating filament and housed in an evaporator. During the deposition, the sample is exposed to the heated filament with the valves of the evaporator open. One of such metal filaments (cobalt) is housed in the OMBE and others are built in separate evaporators in the preparation chamber.

Finally, when the sample adsorbates have been deposited by controlling the flux of the sublimation, the sample is cooled to around 150 K with liquid helium through the manipulator. The sample is then transferred to the STM and cooled further to 6 K, whereby the sample reaches a thermal equilibrium with the STM and the measurements are begun.

4 Boron Nitride on Cu(111): An Electronically Corrugated Monolayer

Ultrathin films of boron nitride (BN) have recently attracted considerable interest given their successful incorporation in graphene nanodevices and their use as spacer-layers to electronically decouple and order functional adsorbates. Here, we introduce a BN monolayer grown by chemical vapor deposition of borazine on a single crystal Cu support, representing a model system for an electronically patterned but topographically smooth substrate. Scanning tunneling microscopy and spectroscopy experiments evidence a weak bonding of the single BN sheet to Cu, preserving the insulating character of bulk hexagonal boron nitride, combined with a periodic lateral variation of the local workfunction and the surface potential. Complementary density functional theory calculations reveal a varying registry of the BN relative to the Cu lattice as the origin of this electronic moiré-like superstructure.

4.1 Introduction

Atomically thin layers of carbon (graphene) and hexagonal boron nitride (h-BN) can be grown on various transition metal supports with exquisite control of the interface structure. [56] In analogy to graphene, a two-dimensional atomically thin boron nitride film is named boronitrene layer or BN monolayer. [57] These sp^2-hybridized sheets currently attract considerable attention, both for the fascinating properties of the individual monolayers and for the promising characteristics of systems combining graphene and h-BN. In case of h-BN, the bulk compound has excellent properties like inertness, high temperature stability, low dielectric constant, large thermal conductivity and high mechanical strength. [58, 59] Additionally, crystalline h-BN is

a 5.97 eV direct band gap insulator and can emit photons in the far-ultraviolet range. [60–62] Thus, ultrathin layers of boron nitride are promising functional materials. In a nano and surface science context, two applications make BN monolayers highly relevant: First, their combined use with graphene in atomically defined bi- or multilayer heterostructures and second their role as templates to support, decouple and order individual adsorbates or nanostructures. The structural similarity of two-dimensional graphene and h-BN expressed by a small lattice mismatch (<2%) [33] makes h-BN a promising substrate for graphene electronics. [36] Indeed the functional characteristics of graphene on h-BN are drastically improved compared to conventional SiO_2 substrates. [32, 34, 35] Furthermore h-BN allows to tune the band gap of graphene in heterostructures [33, 63] or in hybridized single-layer systems. [64] Regarding the use of epitaxial BN monolayers as templates, several recent reports highlight functionalities gained by the decoupling and ordering properties of BN. [27, 65–68]

4.2 Previous STM studies of BN on metal surfaces

The successful growth of single BN layers by chemical vapor deposition (CVD) or subsequent chemical reactions has been reported e.g. on various 3d, 4d and 5d transition metals. [69–73] Depending on lattice mismatch, symmetry of the supporting surface and interaction strength between BN and metal, a variety of morphologies can be achieved: Uniform commensurate layers (Ni(111)), [54, 55, 74] films exhibiting moiré patterns (Pd(111), Pt(111), Pd(110)), [75–77] strongly corrugated nanomesh topologies (Rh(111), Ru(0001)) [66, 78] or one-dimensional superstructures (Cr(110), Fe(110)). [79, 80] For all the substrates addressed in a recent density functional theory (DFT) study, the N atom in the BN layer is repelled from the metal while the B is attracted. [81] Accordingly, the registry of the (B, N) units to the surface metal atoms is crucial for the bonding strength. Considerable geometric corrugations can only be achieved by a large lattice mismatch combined with strong electronic BN/metal interactions, which are dictated by the filling of the metal d shell. According to theoretical reports, BN thus has a very low binding energy on Ag(111) and Cu(111), consistent with experimental evidence of a weak interaction in both systems. [73, 82] In analogy to the Ni(111) case, where the small

lattice mismatch of -0.4 % leads to a commensurate 1x1 structure, [55, 83] a slightly stretched commensurate 1x1 overlayer was proposed for Cu(111) which has a 2.6 % larger lattice constant than Ni(111). [82]

Compared to other transition metal substrates, Cu(111) has so far received very little attention for h-BN adsorption. This is surprising, as Cu foils are emerging as highly important substrates for mass production of large scale h-BN films [59, 84] which in turn are crucial ingredients in graphene based devices *(vide supra)*. [85] Here, copper is attractive due to its high purity, relative cheapness and etchability. Consequently, it is of eminent importance to characterize the BN/Cu(111) interface in detail, as it serves as a model system for h-BN overlayers on copper. In contrast to the BN case, graphene growth on Cu single crystals is well documented. [86–88]

In this chapter, we present a thorough characterization of a BN monolayer grown on Cu(111) using CVD of borazine (HBNH)$_3$ under well-defined ultra-high vacuum (UHV) conditions. Using low-temperature scanning tunneling microscopy (STM), spectroscopy (STS), and complementary DFT calculations (using the cp2k code, www.cp2k.org), we show that a BN monolayer interacts very weakly with the supporting Cu surface and thus keeps the intrinsic insulating properties of h-BN. In contrast to previous studies, [82] our data evidence a non-commensurate overlayer structure. Importantly, we report a considerable electronic corrugation of the BN monolayer on Cu(111), caused by a mismatch in the registry to the substrate. Compared to other BN/metal systems, this superstructure is not linked to a strong geometric corrugation. This makes BN/ Cu(111) unique.

4.3 Morphology of BN monolayer on Cu(111)

The initial growth phase of boron nitride on Cu(111) was studied by applying sub-monolayer coverages. Such incomplete layers allow for a direct comparison of BN terminated surface areas with bare Cu(111). Figure 4.1 shows STM images recorded after exposing the Cu substrate to 42 L of borazine at 980 K. At a sample bias of 4 V BN islands of irregular shape are observed (Figure 4.1a). The BN exhibits a moiré-type corrugation featuring protrusions, labeled "hills (H)" and depressions, referred to as "valleys (V)". At lower bias voltages, the BN appears transparent in STM images and is nearly indistinguishable from the Cu substrate, mainly the island boundaries are discernible (Figure 4.1b). The apparent height of the BN layer

is plotted in Figure 4.2c depending on the sample bias. In a large voltage range (-4 V < V_b < 3 V) the apparent height is below 0.3 Å, while at 4 V and 6 V it exceeds 4 Å.
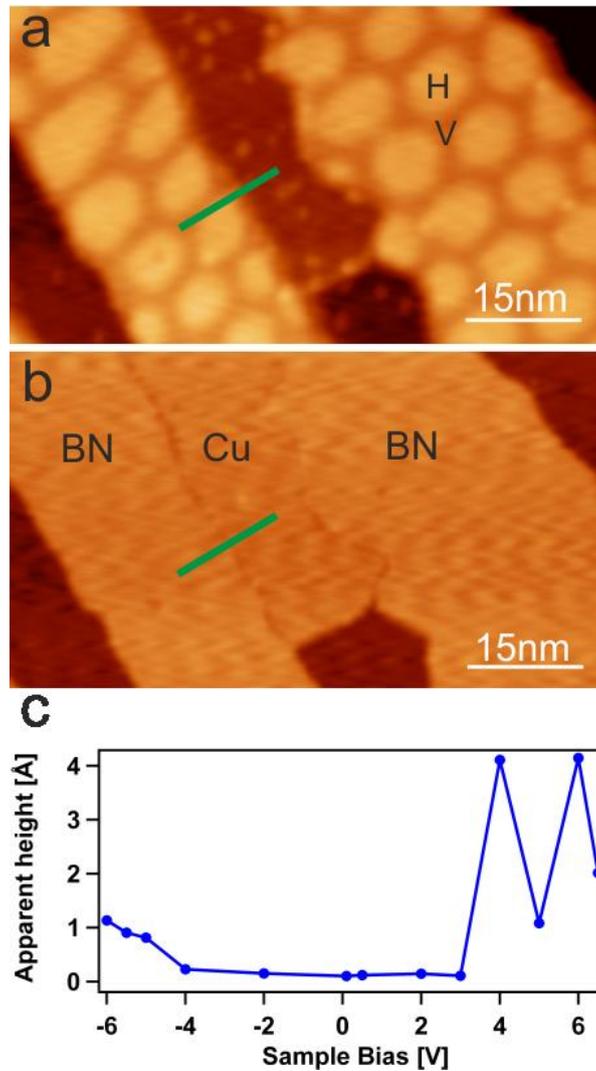
Figure 4.1: Characterization of BN islands on Cu(111). (a) High-bias STM image of the Cu substrate partially covered by BN. A moiré-like superstructure distinguishes the BN regions. Here, the bright areas are labeled "hill (H)" and the surrounding dimmer spaces are named "valleys (V)" (V_b = 4 V, I = 50 pA). (b) STM image of the same area recorded at lower bias voltage (V_b = 1 V, I = 50 pA). The BN islands are transparent and reveal the underlying Cu(111) terraces. The green line highlights the position used to determine the apparent height of the BN island relative to the Cu(111) support. (c) Averaged apparent height of the BN sub-monolayer as a function of sample bias voltage.

This clearly indicates that STM images do not reveal the true topographic height of the BN islands, which is close to 3.0 Å *(vide infra)* but are rather dominated by electronic effects. Indeed, given the insulating property of h-BN, we do not expect a contribution of BN to the local density of state (LDOS) within the band gap. Accordingly, the BN islands appear nearly transparent in STM data covering an extended voltage range around the Fermi level (E_F). The large apparent height of BN layers at high positive sample bias voltages, representing unoccupied electronic states, emerges from tunneling into field emission resonances (FER) [89][50] and will be discussed below. The contrast at high negative bias voltages is tentatively assigned to the valence band of BN (see Figure 4.7 later)

Images taken in the gap revealing the Cu terraces and step edges underneath the BN islands show that the latter mainly follow the shape of the Cu island they reside on (Figure 4.1b). This suggests that the BN facilitates material transport of Cu atoms on the surface at the growth temperature. The BN "rides" on mobile Cu atoms and stabilizes the underlying Cu islands.

4.4 Incommensurate stacking of BN/Cu(111)

Figure 4.2a shows a large-scale STM image of a complete BN monolayer on Cu(111) recorded at 4 V. As in the sub-monolayer case, the BN is characterized by moiré patterns. Independent of the preparation conditions (i.e. growth temperature and borazine partial pressure), we always observed the coexistence of such quasi-hexagonal patterns exhibiting different periodicities and orientations (Figure 4.2b). However, higher temperature growth of the BN layers seems to increase the domain size. For the highest quality BN film grown at 1120 K altogether thirteen different moiré patterns with periodicities ranging from 5 nm to nearly 13 nm were identified. Figure 4.2b shows four of these moiré domains labeled α, β, γ and δ, respectively. The occurrence and coexistence of moiré superlattices is well documented for both BN and graphene overlayers on metallic substrates [75, 87, 90] but also for graphite, where so-called supergiant lattices with periodicities up to 15 nm were reported. [91] Generally the moiré patterns are caused by a rotational misalignment and/or a different periodicity of the overlayer compared to the supporting lattice. [90, 92] As control experiments omitting the borazine dosage yield a bare Cu(111) surface without any moiré-like structures, we exclude that graphene islands induced by a

potential carbon contamination contribute to the observed surface structures.

To rationalize the emergence and coexistence of the different moiré patterns, we applied a geometrical model overlay of two hexagonal grids representing the BN and the Cu(111) lattice, respectively. This simple approach proved to be successful in describing moiré patterns of epitaxial graphene or BN on various transition metal surfaces including Cu(111). [75, 87] Concerning the BN lattice, it is sufficient to include one atomic species in the modeling, as pointed out in earlier reports. [75, 90, 93] The Cu(111) grid is determined by a lattice constant of 2.556 Å. Neither a rigid BN overlayer with the room-temperature bulk lattice constant of 2.50 Å [94] (2% lattice misfit), nor a BN grid expanded to fit the Cu(111) periodicity (0% lattice misfit) were able to reproduce the experimentally observed moiré patterns: The periodicity and orientation of the moiré domains did not match for any rotation angle between the two grids. However, when the BN lattice was slightly stretched (1.8% lattice misfit), [81] both the measured orientations and periodicities of the moirés are nicely described by the model overlay applying only minute rotation angles between the two grids. Three cases are highlighted in Figure 4.2c-e where rotation angles from 0° to 3° cover the complete range of periodicities observed in the experiments. For example the model in Figure 4.2d represents the β domain. The successful description of the experimental data recorded at 6 K by our model relying on a 1.8% lattice misfit might be attributed to the negative in-plane thermal expansion coefficient of h-BN [94] and a deviation of the monolayer lattice constant from the bulk value.

Of course this simple model should not be overinterpreted: Experimental data show, e.g. a distortion of the hexagonal symmetry near domain boundaries (see Figure 4.2b), indicating some strain in the h-BN layer. [95] Nevertheless, it can be concluded that BN on Cu(111) forms domains with different orientations similar to the Ag(111) case [73] and does not adapt a commensurate 1x1 structure as on Ni(111). [55] This finding is in agreement with the observation of randomly oriented triangular BN islands within the same grain of a Cu foil [59] but obviously conflicts with a report claiming a commensurate 1x1 BN monolayer on Cu(111). [82] This discrepancy might be explained by the coexistence of BN domains exhibiting large periodicities and minute rotation angles could be elusive to LEED observations and only result in broadened integer 1x1 spots.
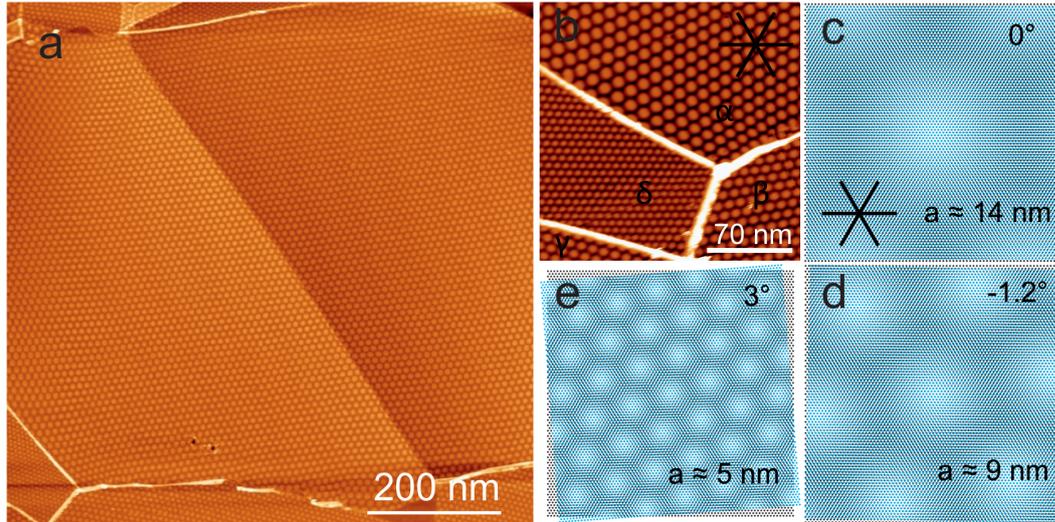
Figure 4.2: Complete BN monolayer on Cu(111). (a) STM image evidencing coexisting BN domains comprising different moiré superstructures (V_b = 4 V, I = 40 pA). The central domain extends to the μm range. (b) Enlarged image highlighting four moiré phases (labeled α, β, γ and δ, respectively) separated by domain boundaries (V_b = 4 V, I = 0.6 nA). Each phase is characterized by a different orientation and periodicity of the pattern. The star represents the dense-packed directions of the Cu(111) lattice. (c-e) Moiré models based on an overlay of two grid patters representing the Cu(111) lattice (black) and a slightly stretched BN overlayer (1% mismatch, blue). Minute misalignment angles below 3° reproduce the full range of periodicities and orientations observed in the experiments. For example the structure presented d) corresponds to the β domain.

4.5 Electronic corrugation of BN/Cu(111)

Figure 4.3 reveals that the contrast and corrugation of the moiré patterns drastically depends on the applied bias voltage. Following the trends in apparent height (compare Figure 4.1c), the measured corrugation is hardly resolved in a voltage range from -4 V to 3 V (Figure 4.3d). At 4 V it reaches a maximum of approximately 1.5 Å, above 4.5 V a contrast inversion is observed, i.e. the regions representing protruding "hills" at and below 4 V (Figure 4.3a) are imaged as depressions above 4.5 V (Figure 4.3c). This peculiar behavior is explained by spatial variations of the voltage where the first field emission resonance occurs *(vide infra)*. Importantly, this measurement leads us to conclude that the moiré patterns are not purely topographic features but instead mainly an electronic effect.
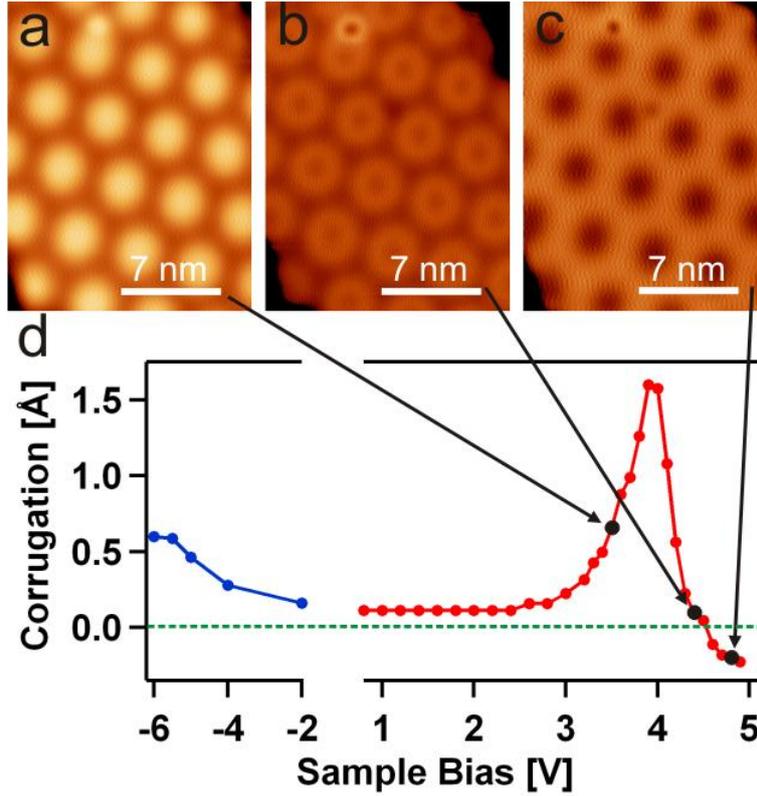
Figure 4.3: Electronic origin of the moiré superstructure. (a) In a large bias voltage range, the moiré is resolved as quasi-hexagonal array of protrusions ("hills)" in STM images (V_b = 3.7 V, I = 50 pA). (b) Around 4.25 V the contrast changes (V_b = 4.25 V, I = 50 pA). (c) At higher voltages, a contrast inversion is observed: Now the connecting "valley" regions appear brighter than the "hills" (V_b = 4.9 V, I = 50 pA). (d) Plot of the moiré corrugation vs. sample bias voltage. The apparent corrugation including the contrast inversion is related to the appearance of the first field emission resonance peak (*vide infra*, compare Figure 4.5c).

An additional feature related to the electronic structure of BN/Cu(111), an electronic interface state, can be probed at low bias voltages, where the BN overlayer appears transparent (compare Figure 4.1c). Figure 4.4a shows an STM image of a Cu region partially covered by a BN island discernible by the characteristic moiré pattern. Differential conductance (dI/dV) maps recorded at low bias voltages (Figure 4.4b) visualize standing wave patterns both on the bare Cu(111) area and on the BN covered region. On Cu they represent the well-known Shockley-type surface state electrons scattered by defects, [96] whereas on BN they are assigned to an interface state band. [97] It should be noted that the latter does not correspond to an intrinsic BN related band, but only represents a modification of the Cu(111)

surface state upon BN adsorption. A close inspection of Figure 4.4b reveals a larger wavelength of the standing wave pattern under the BN (region marked in green) than on the bare Cu (red region).
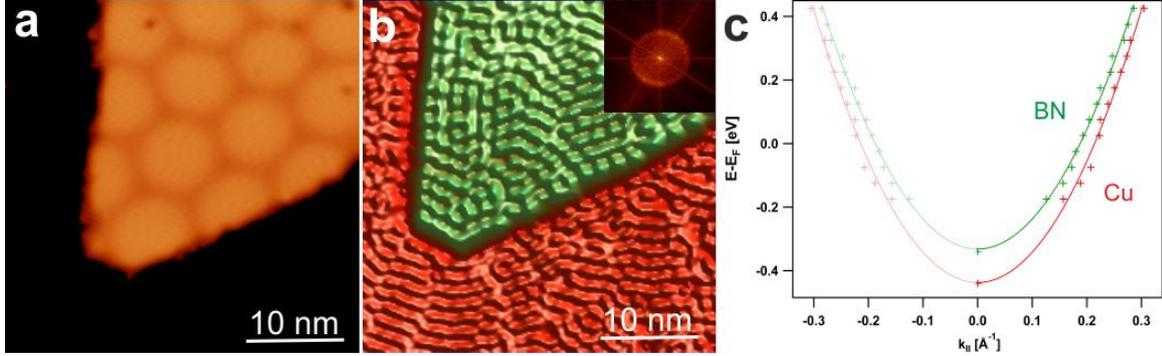
Figure 4.4: Modification of the Cu(111) surface state upon BN adsorption. (a) STM image of a triangular shaped BN island in Cu(111) (V_b = 4 V, I = 50 pA). (b) dI/dV map of the same area recorded at 0.075 V (I = 0.1 nA). Standing wave patterns are resolved on the bare Cu region (red) and under the BN (green). The wavelength of the BN/Cu(111) interface state is larger than that of the native Cu(111) surface state. The inset shows an FFT image used to extract $k_{\parallel}$. A comparison to a) reveals that the moiré features have no discernible impact on the standing wave pattern. (c) The dispersion (E vs $k_{\parallel}$) of the interface state band (green) reveals an upshift compared to the surface state (red). The data points extracted from dI/dV maps ($k_{\parallel} \neq 0$) and point spectra ($k_{\parallel} = 0$) fit a parabolic dispersion (see text for discussion).

In order to determine the dispersion of the surface and interface state band a series of dI/dV maps was taken in a voltage range from -0.175 V to 0.425 V. For every voltage the wave vector $k_{\parallel}$ was extracted from the fast fourier transform (FFT) of the dI/dV maps for both the bare Cu(111) and the BN regions. A typical FFT image is shown in the inset of Figure 4.4b. The resulting dispersion plots (energy versus $k_{\parallel}$) are displayed in Figure 4.4c together with parabolic fits based on the equation $E = E_o + (\hbar k)^2/2m*$. [98] For the bare Cu(111) area, both the band onset ($E_o = -0.44V$) and the effective mass ($m* = 0.40 \pm 0.02\ m_e$) match the literature values. [97, 99] Underneath the BN, the band is clearly upshifted by about 106 meV while the effective mass is hardly changed ($m* = 0.41 \pm 0.02 m_e$). It is instructive to compare these values to related systems: A Xe layer adsorbed on Cu(111) induces an upshift of the surface state band of 130 meV, [100] for NaCl/Cu(111) a value of 230 meV is reported. [97] This suggests a weak interaction between the BN and the

Cu support. More general, according to an empirical rule postulated by Ziroff *et al.* [101] for physisorbed overlayers, the upshift of the energy (ΔE) can be directly correlated to the adsorption energy per surface area (V_R), with the expression $V_R \propto \Delta E$ using a proportionality constant of 0.106 $\mathring{A}^{-1}$. [101] Accordingly an energy upshift of 106 meV yields an estimated adsorption energy per surface area of roughly 11.24 meV/$\mathring{A}^2$ or 59.7 meV/unit cell.

From the perspective of theory, previous studies using density functional theory on a commensurate lattice revealed a strong dependence on the functional employed, e.g. the local-density approximation (LDA) yielded an adsorption energy of 190 meV/unit cell and the generalized gradient approximation (GGA) values as low as 10 meV/unit cell. [81] Our own GGA+vdW calculations include hitherto neglected van der Waals (vdW) contributions and consider a number of different adsorption registries of the BN, focusing on one BN ring (1x1 adsorption). In particular, the strongest binding (with an energy of 270 meV/unit cell) occurs when the B atoms reside in the fcc positions and the N atoms are placed atop Cu atoms in the top layer of the (111) surface ("$B_{fcc}N_{top}$"). The lowest value of the binding energy, 234 meV/unit cell is found for the $B_{fcc}N_{hcp}$ configuration, where both B and N occupy hollow sites (compare Figure 4.6). The higher adsorption energies compared to previous results can be rationalized with the use of our vdW correction, which seems to lead to overbinding when compared to the value estimated from the experiments. Looking only at the uncorrected GGA adsorption energies (with unchanged geometries), we find the $B_{fcc}N_{top}$ configuration to be more stable than $N_{hcp}B_{fcc}$ by 120 meV/unit cell. In both cases, however, the adsorption energies are negative (i.e. non-binding), which highlights the importance of our vdW correction.

Both our experimental and calculated adsorption energies indicate that BN has a very weak interaction with the underlying substrate. This supports the findings of earlier DFT calculations claiming that BN/Cu(111) has one of the lowest binding energies as compared to other non-noble transition metals. Clearly, the existence of the diverse moiré patterns induced by various rotational domains of the BN on Cu(111) is facilitated by this weak interaction. However, it is important to note that the moiré features have no obvious influence on the interface state standing wave pattern (compare Figure 4.4a and b), i.e. we do not observe a quenching of the Shockley surface state at any region. This excludes strong site-specific interactions of the BN with the Cu surface and thus makes a pronounced geometric corrugation of the BN sheet rather unlikely.

4.6 Electronic structure of BN/Cu(111)

As mentioned before, the BN layers appear spatially inhomogeneous due to the presence of moiré features with predominantly electronic character. To verify the proposed spatial electronic modulation and to characterize the BN in comparison to Cu(111), we performed two sets of experiments yielding information on the surface potential. First, we determined the apparent barrier height Φ, which is related to the local workfunction and thus the surface potential, by measuring the tunneling current I as a function of tip sample distance z. Figure 4.5b shows $I(\triangle z)$ curves representing characteristic locations of the sample indicated in Figure 4.5a, namely the bare Cu(111) surface (red), the "hills H" (blue) and the "valleys V" (green) of the BN. The relation $I \propto exp(-2\kappa z)$, where is the decay coefficient, [102] was used to fit the experimental data and to extract κ and Φ. [103] This procedure yields the following values: $\kappa_{Cu} = 0.97 \pm 0.02 \mathring{A}^{-1}, \kappa_V = 0.91 \pm 0.02 \mathring{A}^{-1}$ and $\kappa_H = 0.89 \pm 0.01 \mathring{A}^{-1}$. Hereby, hundreds of $I(\Delta z)$ curves taken on different, but equivalent locations were averaged. κ_{Cu} agrees reasonably well with previously published values ($\kappa_{Cu} = 1.01 \pm 0.03 \mathring{A}^{-1}$). Following a protocol discussed by Vitali $et\ al.$ [104] the κ and Φ values are used to determine the relative variation of the workfunction between bare Cu, the "H" and "V" regions, respectively, which is independent from the tip workfunction. This approximation combined with the reported workfunction of 4.94 eV for bare Cu(111) [54] yields a workfunction of 4.1 eV for the BN "V" position and 3.8 eV the "H" locations. Thus, the workfunction on BN is clearly reduced compared to bare Cu(111), confirming the trends observed at all BN/transition metal interfaces. [54] However, our estimated values based on local measurements indicate a more pronounced shift than inferred from space-averaging methods. [82] Importantly, these results point to a spatial variation of the workfunction and thus to a variation of the surface potential of the BN monolayer.

To further corroborate this spatial modulation of the electronic structure in BN on Cu(111), we performed a second set of experiments sensing the surface potential. As a probe, we used field emission resonances (FERs). The energies, at which FERs are observed in dI/dV spectra are related to the surface potential, as the FERs are based on image potential states. [50, 89, 105] Figure 4.5c shows dI/dV traces recorded with closed feedback loop for the three characteristic positions highlighted in Figure 4.5a using the very same STM tip. Clearly, a series of well-defined FERs is observed at all location. Importantly, the spectra show significant shifts of all peaks

depending on the probed region. As seen in Figure 4.5c the first resonance appears clearly above 4 V at the bare Cu(111) (red), below 4 V on the "valley V" (green) and is shifted to even lower voltages on the "hills H" (blue). As the first peak of the FERs appears at voltages around the local workfunction of the sample, [105–107] these data confirm a workfunction lowering on the BN compared to Cu(111) and corroborate the spatial modulation of the surface potential on the BN. Figure 4.5c also reveals that the appearance of the moiré patterns, including the observed contrast inversion at high bias voltages (compare Figure 4.3), is directly related to the spatial variation of the energy at which the first FER occurs: When increasing the bias voltage, the differential conductance first rises in the "H" area resulting in a larger apparent height of the "hills" in the STM images. When the bias voltage is augmented further, it matches the energy of the first peak in the "V" region, inducing a bright appearance of the "valley" regions, while the "hills" appear dim.
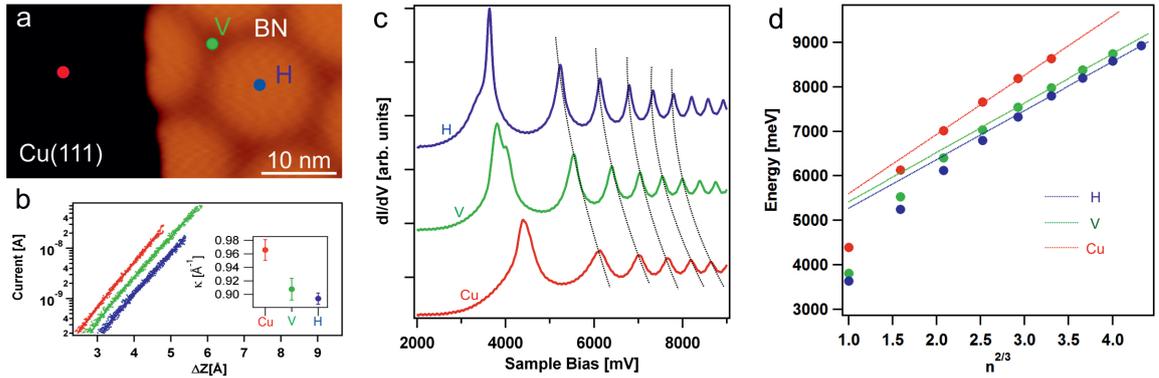
Figure 4.5: Electronic superstructure of BN/Cu(111). (a) STM image representing the three decisive positions to characterize the local surface potential at the BN/Cu(111) interface: Bare Cu (red marker), BN valley (H, green) and BN hill (H, blue), respectively (V_b = 4 V, I = 50 pA). (b) $I(\Delta z)$ approach curves at the three points represented in logarithmic scale. The red line exhibits the largest slope followed by green and blue (Curves are laterally offset for clarity). The inset shows the corresponding κ values extracted from the fits in b), reflecting a spatial variation of the local workfunction. (c) dI/dV spectra showing series of field emission resonances (FERs) representing the same three positions ence a clear shift in the energy of all resonances, confirming a spatial modulation of the surface potential (see text for discussion). The dashed curves serve as guide to the eye. (Starting parameters: V_b = 1 V, I = 0.1 nA). (d) Energy vs $n^{2/3}$ plots of "H" (blue), "V" (green) and Cu (red) locations in a). The extrapolation of linear fits give approximate workfunction differences between the points.

Another method to empirically approximate the workfunction difference between the BN "H", "V" areas and the Cu(111) substrate is to extrapolate the linear plots described in section 2.3 where the energy (eV) of the FERs are plotted against factor $n^{2/3}$. In Figure 4.5d, we see the plots of the BN hill (blue dots), valley (green dots) and Cu (red dots) corresponding to respective location in Figure 4.6a. As the intial few points deviate from the linear trend due to the modified barrier height (see Figure 2.5a and following description), only the latter points (higher n) are fitted to a linear plot (dotted lines of respective colors). Finally, an extrapolation of the linear fits yield workfunction differences $\triangle_{Cu-H} = 330\,meV$ and $\triangle_{V-H} = 140\,meV$. This agrees well with the trend of workfunction change approximated by $I(\triangle z)$ method described above and the following DFT calculations.

Finally, we introduce an additional experimental insight into the electronic structure of the BN/Cu(111) interface. Figure 4.6b represents a series of 81 dI/dV spectra recorded along a line across the surface, plotted in an energy vs. distance map, where the dI/dV intensity is color-coded. The spectral features, appearing as bright bands in the map reflect field emission resonances (FERs, see Figure 4.5c). As the energy of the FERs is related to the local workfunction and the surface potential, [50, 89, 105, 108] we conclude that the BN/Cu(111) interface is characterized by a smooth, continuous lateral variation of the surface potential and the local workfunction. Figure 4.6b reveals considerable energy shifts of the FER's by ≈ 300 meV. In agreement with our previous report, the low local workfunction regions correspond to the H areas. [37] However, it should be noted that the energy shift of single FERs does not directly reflect the local workfunction difference. Only an evaluation of several resonances yields an estimate for this quantity. [50] Consistent with our previously published experimental values, the local workfunction on the H regions is ≈ 300 meV lower than on the B or V regions. We assign all spectral features in Figure 4.6 to FER's and exclude important contributions of localized interface states as all peaks show consistent energy shifts when changing the tip-sample distance (see Figure 4.7).
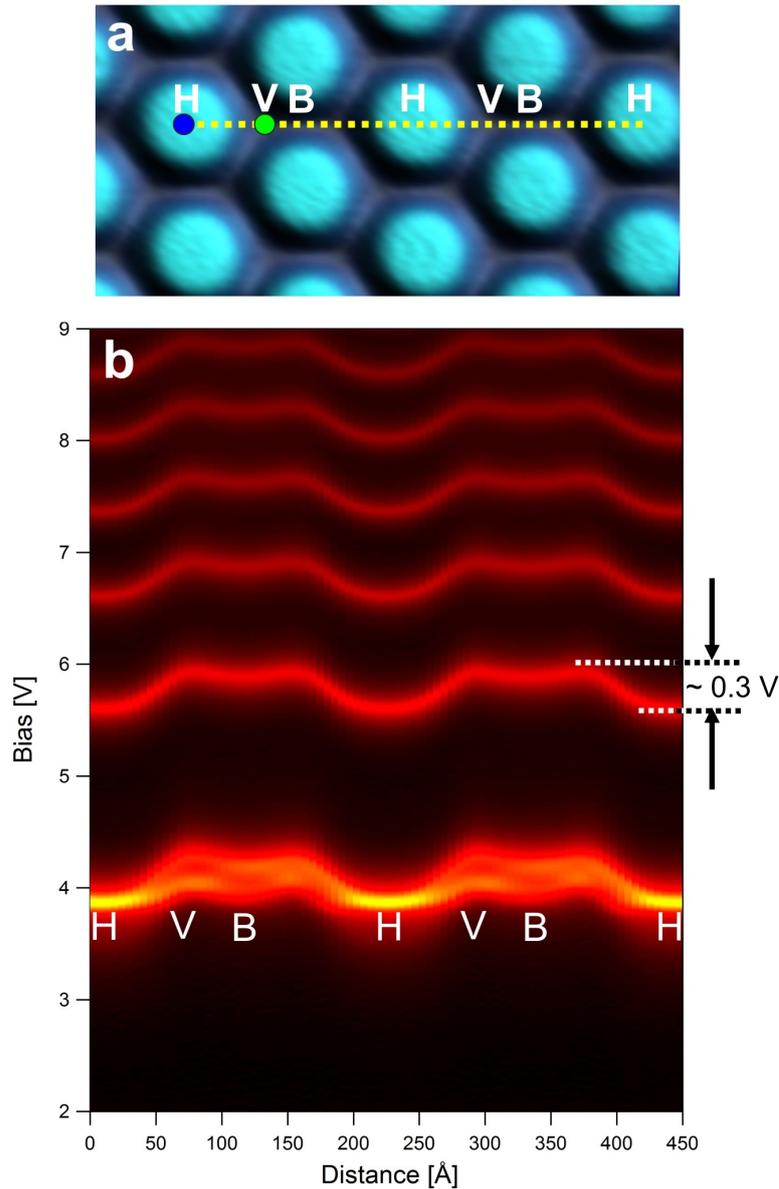
Figure 4.6: Electronic superstructure of the BN/Cu(111) interface. (a) STM image recorded at a bias of 4.0 V revealing circular protrusions (labeled "hills" H or moirons) separated by dimmer regions ("valley" V and "bridge" B, respectively) (I = 50 pA).The dotted line represents the positions of 81 *dI/dV* spectra taken across this moiré-like superstructure. The colored dots mark two characteristic positions (H (blue) and V (green)) to describe the local surface potential at BN/Cu(111). Corresponding *dI/dV* spectra are shown in (4.5c). (b) Energy vs. distance map of the *dI/dV* spectra revealing a continuous spatial modulation of surface potential along the line plotted in (a). The bright bands represent field emission resonances (FERs), evidencing an energy variation of about 300 meV between H and V areas.
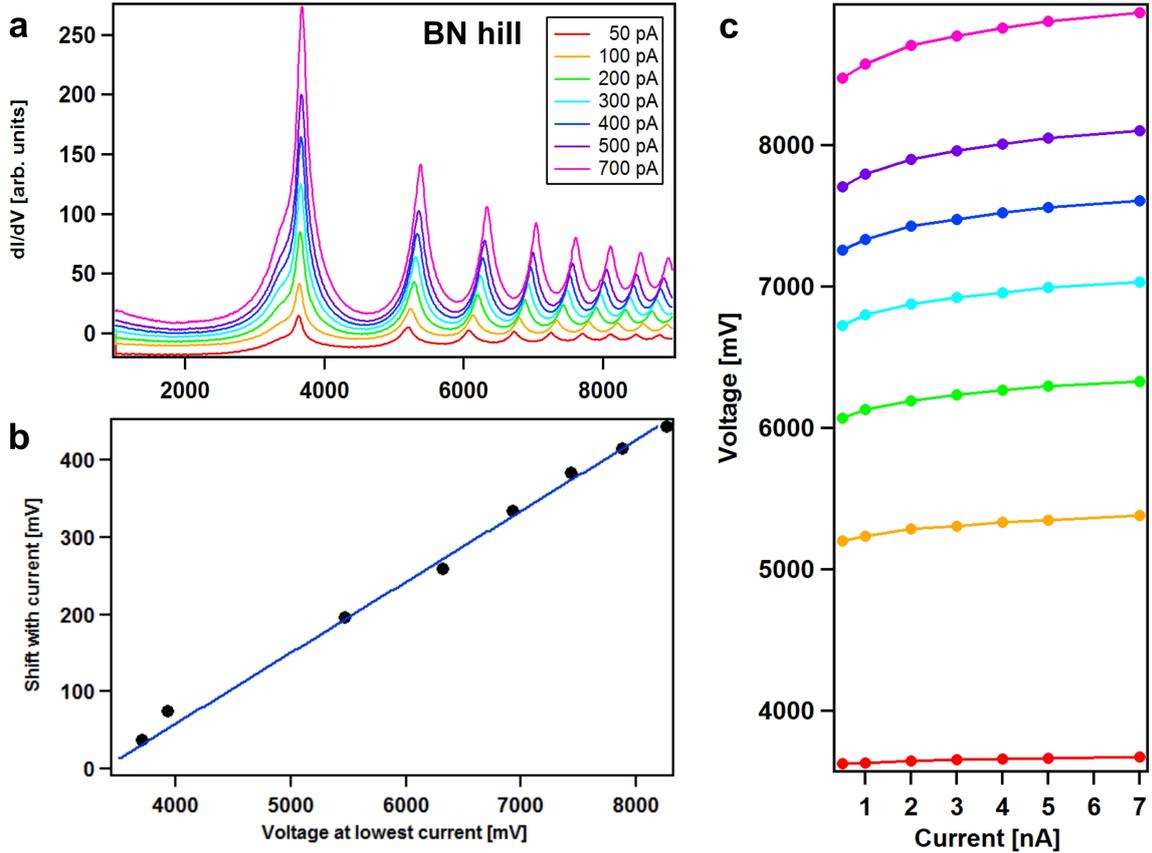
Figure 4.7: Current dependent shifts of the field emission resonances (FERs) measured on BN/Cu(111). (a) A set of FER spectra measured at the same location between 50 pA (red) and 700 pA (pink), representing a considerable range in tip-sample separations. (b) The energy shift in the spectra changes linearly with the voltage. (c) Voltages of the first seven FER as function of current. All resonances show a similar trend for increasing voltage/decreasing tip-sample distance. Consequently, we assign all observed spectral features to FERs.

4.7 Theoretical calculations of BN/Cu(111)

In order to model this spatial variation of the electronic landscape theoretically, we studied a 23x23 4-layer Cu(111) slab with an adsorbed 24x24 BN layer which was rotated by 2.11° (further details and results on this system will be published elsewhere). This arrangement leads to a moiré-type pattern where the adsorption registry spatially varies across the layer with a periodicity of 59 Å. After optimization of the structure the average distance between the monolayer and the surface was

3.0 Å, with a small difference of 0.16 Å between the closest and farthest atoms. Consequently, with BN we present a two-dimensional crystal that interacts only weakly with the Cu(111) support but nevertheless is topographically planar, i.e. withstands instabilities as considerable rippling characteristic for other quasi-freestanding ultra-thin films. [109] The electrostatic potential of the system exhibits spatial variations across this surface, following the change in adsorption registry. In the regions where BN is adsorbed in an $B_{fcc}N_{top}$ fashion, the electrostatic potential (and thus the workfunction) is 0.13 eV lower than around the $B_{fcc}N_{hcp}$ configuration. In between those two extremes the workfunction varies in approximately circular patterns. This difference of the workfunction agrees reasonably well with our experimental estimate, as well as with our results from the 1x1 adsorption, where $B_{fcc}N_{top}$ and $B_{fcc}N_{hcp}$ differ by 0.08 eV. Compared to the bare Cu surface, BN adsorption lowers the calculated workfunction by 1.21 eV in the former case, and 1.13 eV in the latter. Figure 4.8 summarizes the theoretical findings, comparing the two extreme registries ($B_{fcc}N_{top}$ versus $B_{fcc}N_{hcp}$) of the BN monolayer on Cu(111).

The experimental and theoretical observations outlined above give indications that serve to rationalize the notable electronic corrugation of the BN/Cu(111) system. In particular it is important to appreciate that the electronic corrugation is present even though the monolayer is only very weakly corrugated structurally. It appears that the spatial variation of the adsorption registry is responsible for the modulation of the workfunction. As BN in the $B_{fcc}N_{top}$ registry interacts stronger with the surface it can change the electronic structure of the substrate, resulting in a stronger lowering of the workfunction. The small difference in adsorption energy seems to be amplified in the workfunction. This change of electronic structure is also evidenced by a change in the local density of states of the N atoms, where we observe the highest occupied molecular orbital (HOMO) peak of the p_z states lowered by 0.3 eV in the $B_{fcc}N_{top}$ configuration (see Figure 4.9).

As shown in various reports a trapping and ordering of atomic or molecular adsorbates can be induced by potential variations across the strongly corrugated BN nanomesh, [27, 28, 30, 110] in structurally related graphene overlayers, [26, 111–114] oxide films, [23, 115] or other nanostructured surfaces. [116] Compared to these systems, BN/Cu(111) yields the advantage of being a topographically planar insulating spacer-layer. Accordingly, the electronically templated BN monolayer on Cu(111) bears great promise as a platform for nanoscale assemblies in functional molecular architectures.

(B , N)	(fcc , top)	(hcp , fcc)
E_{bind} incl. van der Waals	270 meV / unit cell	234 meV / unit cell
E_{bind} without van der Waals	-171 meV / unit cell	-292 meV / unit cell
Work function; 1 x 1	3.62 eV	3.71 eV
Work function; Moiré	3.64 eV	3.77 eV
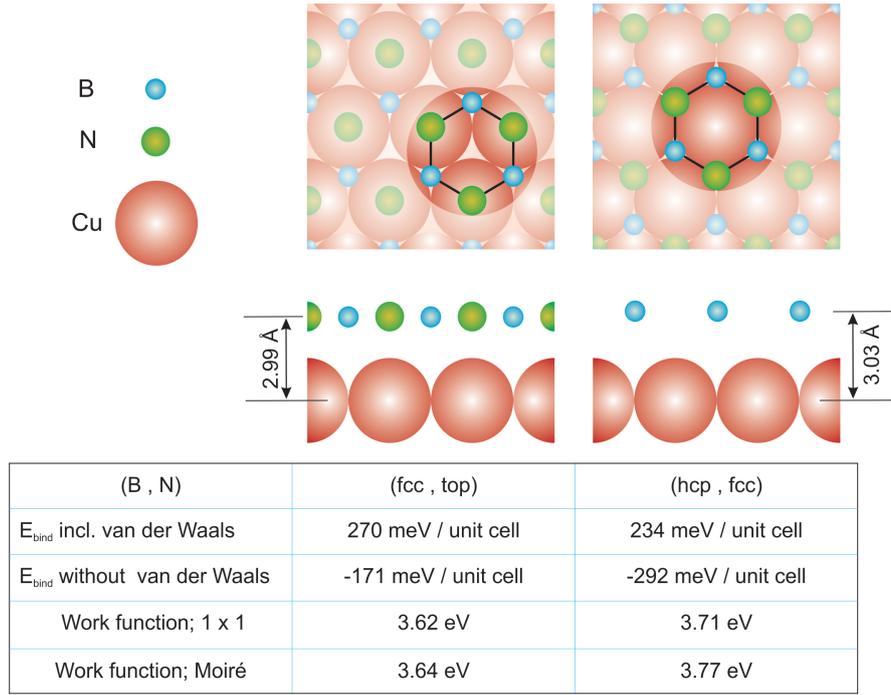
Figure 4.8: Density functional theory calculations of BN/Cu(111). The strongest interaction of the BN with the Cu(111) is observed for a $B_{fcc}N_{top}$ registry, the weakest for $B_{fcc}N_{hcp}$. These two extreme configurations show only minute differences in the adsorption height of the BN, but nevertheless exhibit a markedly different local workfunction (see text for further discussion). [37]
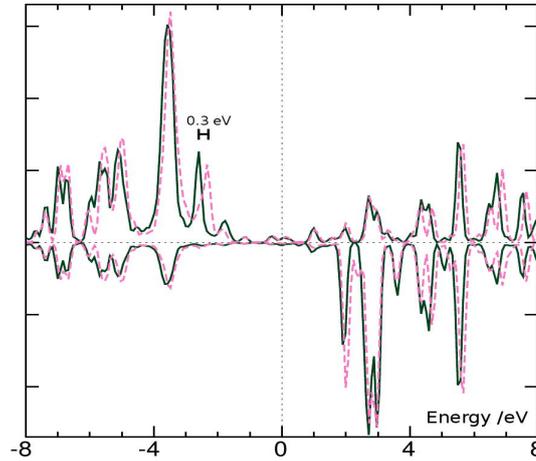
Figure 4.9: Projected Density of States (PDOS) of p_z orbitals on nitrogen (positive y axis) and boron (negative y axis) for BN in $B_{fcc}N_{top}$ (continuous line) and $B_{fcc}N_{hcp}$ (dashed line) registries. The 0.3 eV shift of the highest occupied molecular orbital (HOMO) peak is highlighted. [37]

4.8 Experimental procedures and theoretical methods

All experiments were performed in a custom-designed ultra-high vacuum (UHV) apparatus comprising a commercial low-temperature CreaTec STM [117] based on a design described in ref. [118]. The system base pressure is below 2x10-10 mbar. The Cu(111) single crystal surface was cleaned by repeated cycles of Ar+ sputtering (800 eV) followed by annealing to 1000 K. Subsequently, BN (sub)monolayers were prepared by decomposition of borazine $(HBNH)_3$ on the hot Cu(111) surface, following a recipe described in detail in previous publications. [54, 55, 119] Importantly, the BN growth is self-saturating when a complete monolayer coverage is reached. During borazine dosage, the Cu(111) crystal was kept at temperatures between 983 K and 1120 K. Generally, the higher temperatures favor larger BN domain sizes and thus reduce the defect density, but go in hand with desorption of Cu from the crystal surface. For full BN layers, the sample was typically exposed to ~800 L of borazine. For sub-monolayer coverages, exposures down to 40 L were applied. After the borazine dosage, the sample was cooled down and transferred into the STM, where constant current images were recorded at T ~ 6 K using electrochemically etched tungsten tips. In the figure captions V_b refers to the bias voltage applied to the sample and I to the tunneling current. Differential conductance data (dI/dV spectra and maps) were obtained by lock-in technique with a bias modulation amplitude of 18 mV rms and a frequency of 969 Hz (spectra) and 2.97 kHz (maps). To cover the large voltage range mandatory to measure high-order field emission resonances, the feedback loop was kept closed for the dI/dV point spectroscopy. The fast fourier transformation (FFT) uses the WSxM software. [120] See Section 3.6, chapter 3 for more details.

Density functional theory calculations were carried out in collaboration with a theoretical team at the university in Zurich. The calculations were within the Gaussian-Plane Waves (GPW) formalism [121] as implemented in the CP2K package. [122] The revised PBE functional [123] was used to treat the exchange-correlation energy in combination with the Grimme D3 correction [124] to account for dispersive interactions. Double-Zeta valence polarized basis sets of the MOLOPT [125] type were used for all elements, together with Goedecker Teter Hutter pseudo-potentials. [126] 11, 3, and 5 electrons were considered explicitly in the valence for Cu, B, and N, respectively. The energy cut-off of the plane wave expansion of the density was

set to 500 Ry, and a 20 Å vacuum region was used for surface models in a slab geometry. Commensurate adsorption on Cu was studied using 7-layer Cu(111) slabs with a monolayer of BN on both sides; because the Brillouin zone is only sampled at the Γ-point, the simulations contain laterally a 6x6 supercell.

4.9 Conclusion

In summary, we presented a comprehensive STM/STS study covering the growth and characterization of single BN layers on Cu(111). The insulating properties and the weak interaction of BN with the underlying metallic support are evidenced by the transparent appearance in STM images covering a wide bias range around the Fermi level. The coexistence of various moiré patterns exhibiting giant periodicities resulting from a minute rotation of BN domains together with the emergence of an electronic interface state band prove a weak binding of the BN monolayer to Cu(111). Different adsorption sites of the slightly stretched BN sheets induce spatial variations in the local workfunction and thus the surface potential. The resulting electronic superstructure was characterized by exploring lateral modifications of the apparent barrier height and field emission resonances, respectively. Complementary DFT+vdW calculations reveal a planar geometry of the BN sheet on Cu(111) and identify the $B_{fcc}N_{top}$ registry to result in the strongest adsorption energy and lowest local workfunction. Here, the vdW corrections proved to be decisive for a proper description of the BN adsorption on Cu(111). In conclusion, the electronically templated atomically thin BN layer bears great promise as a platform to support functional nanostructures of reduced dimensions. Following chapters will be about detailed studies of such adsorbates on the BN.

5 Control of Molecular Organization and Energy Level Alignment by an Electronically Nanopatterned Boron Nitride Template

Suitable templates to steer the formation of nanostructure arrays on surfaces are indispensable in nanoscience. Recently, atomically thin sp^2-bonded layers such as graphene or boron nitride grown on metal supports have attracted considerable interest due to their potential geometric corrugation guiding the positioning of atoms, metallic clusters or molecules. Here, we demonstrate three specific functions of a geometrically smooth, but electronically corrugated sp^2/metal interface, namely BN/Cu(111), qualifying it as a unique nanoscale template. As functional adsorbates we employed free-base porphine (2H-P), a prototype tetrapyrrole compound, and tetracyanoquinodimethane (TCNQ), a well known electron acceptor. (i) The electronic moirons of the BN/Cu(111) interface trap both 2H-P and TCNQ, steering self-organized growth of arrays with extended molecular assemblies. (ii) We report an effective decoupling of the trapped molecules from the underlying metal support by the BN, which allows for a direct visualization of frontier orbitals by scanning tunneling microscopy. (iii) The lateral molecular positioning in the superstructured surface determines the energetic level alignment, i.e., the energy of the frontier orbitals, and the electronic gap are tunable.

5.1 Introduction

The functionalization of surfaces by molecular architectures is a promising route towards advanced materials with tailored topological, electronic, optical, magnetic or catalytic properties. Inspired by nature and supramolecular science, self-assembly protocols relying on specific interactions between programmed molecular units were successfully implemented on surfaces to achieve well-defined nanostructures. [7, 8] Scanning tunneling microscopy is the method of choice to image and characterize such low-dimensional architectures with sub-molecular resolution in real space. As STM relies on a finite conductivity of the sample, the vast majority of studies use single crystal metal substrates. This however is associated with severe limitations: Electronic interactions with the metallic support can significantly affect the electronic, magnetic and conformational structure of adsorbates, thereby modifying or hampering their functionality. Furthermore, homogeneous metallic substrates usually prevent the formation of regular arrays of nanostructures. Molecules when adsorbed on a surface interact with both the substrate and co-adsorbates. Depending on the resulting balance of forces, they may experience attractive or repulsive interactions between each other. At submonolayer coverage, the former case yields self-assembled islands or networks [7, 8] while the latter situation leads to a homogeneous distribution of individual molecules scattered across the entire surface area. [127–129] The organized growth of arrays of assemblies, highly desirable to complement structure formation on the nanoscale, thus calls for templated surfaces exhibiting periodicities in the nanometer regime. As reconstructions on metallic substrates only provide limited possibilities regarding periodicity and symmetry of the superstructure, [116, 130] ultrathin adlayers offer new perspectives. [131] Here, special interest focuse on non-metallic or insulating spacer-layers, which reduce the electronic coupling between adsorbate and metallic substrate but are suitable for a characterization with STM, thus yielding information on nearly unperturbed properties of functional adsorbates. The application of various ultrathin oxide, [132] Nitride [133] and halide [21, 134] films grown on metal substrates as supports for atoms or molecules has been reported, but their considerable polarity, corrugation and structural inhomogeneity might be a drawback regarding large-scale self-assembly. As an alternative, epitaxial graphene, [23, 25, 26, 30, 111–113, 135–138] or boron nitride [27, 29, 30, 68, 111, 139, 140] layers recently emerged as promising nanoscale templates. Nevertheless, on insulating spacer-layers, including boron nitride sheets,

self-assembly protocols for the construction of advanced molecular architectures remain to date largely unexplored.

5.2 The substrate and the adsorbate

Atomically thin BN films can be grown by chemical vapor deposition on various transition metals with exquisite control of the interface structure. [55, 66, 70, 73, 75, 80, 93] As for isostructural graphene, the sp^2 sheet can exhibit a considerable geometric corrugation, resulting in nanomesh structures [66] or moiré patterns, or be planar in case of a commensurate, epitaxial fit with the substrate lattice. [55] BN's diverse topographical features on transition metals, together with its exceptional physical and chemical properties (large band gap, inertness, temperature stability), make it lucrative as substrate or template to support molecules [27, 65] *(vide supra)* or graphene. [32, 34, 35] Recently, we have shown that BN on Cu(111) exhibits a rather unique, topographically planar, but electronically corrugated structure. [37] Apart from being an interesting spacer-layer to electronically decouple functional molecules from metal supports, BN/Cu(111) features a periodically modulated surface potential, which is observed as contrast- invertible electronic moiré pattern in STM images. These moiré-like superstructures coexist with variable periodicities, depending on the rotation of the BN domains relative to the Cu(111) lattice. This provides a fascinating potential landscape to study and control the adsorption and electronic properties of complex molecules.

As exemplary functional adsorbate, we use free-base porphine (2H-P, see model in Figure 5.2b), a highly relevant prototype macrocycle representing the parent compound of all porphyrins. Porphyrins are extremely versatile macrocyclic species with an intriguing variety of functional properties. They are ubiquitous in biological systems: incorporated as prosthetic groups in proteins they carry respiratory gases, provide multiple sensing functions in metabolic processes, catalyze chemical transformations, and operate in photosynthetic reaction pathways. [141] Porphyrins are similarly important in synthetic materials and supramolecular chemistry. They have been tailored for sensing purposes, medical applications, catalysis, dye-sensitized solar cells and reticular design of metal-organic frameworks. [142] From a surface science perspective, the versatile chemical termination of functionalized porphyrins allows for the self-assembly of well-defined architectures on metal sup-

ports. For example, two-dimensional (2D) porphyrin arrays and porous networks, 1D-coordination polymers and 0D supramolecules were reported. [12, 13, 143–149] To date, the free-base porphine has received little attention. This is surprising, as systematic studies on 2H-P could provide a reference for the entire class of porphyrins. Multi-method studies of 2H-P on Cu(110) [146] and Cu(111) [128] reveal an electron exchange between the substrate and the porphine. Our recent study of 2H-P on Ag(111) revealed a rather complex behavior considering the inert, noble metal character of the substrate. Charge transfer, preferred adsorption sites and dominating repulsive inter-molecular interactions prevent island formation at submonolayer coverages and induce phase transformations. [129] In striking contrast, functionalized free-base species such as 2H-TPP arrange in well-defined assemblies even at very low coverage. [150] In brief, as the porphine is drastically modified at the molecule/metal interface, no experimental reports on intrinsic characteristics and self-assembly properties of 2H-P on surfaces are available to date. To complement the porphine data, we also applied tetracyanoquinodimethane (TCNQ), a prototype acceptor molecule, as adsorbate on the BN template.

In this chapter, we present a detailed study of 2-HP on BN/Cu(111). Specifically, we report three characteristics of the porphine/BN/Cu interface, which are clearly different from adsorption on metal substrates, thus highlighting the impact of the ultrathin BN spacer-layer. (i) The reduced electronic coupling to the metal support results in a distinct gap of about 3.85 eV and allows us to directly visualize the frontier orbitals of 2-HP in STM images. A comparison to density functional theory and Extended Hückel Theory (EHT) calculations of the charge density of HOMO and LUMO of an isolated 2-HP reveals a good agreement, confirming the assignment of the molecular resonances and the electronic decoupling. (ii) porphines self-assemble into well-defined agglomerates with a nearest neighbor distance of 11.3 Å. At intermediate coverage, highly regular arrays of 2-HP islands are formed, demonstrating the role of the BN/Cu(111) surface as a template for the confined growth of nanostructures. This trapping and templating mechanism yielding ordered assemblies of unprecedented extension is related to the spatial modulation in the surface potential of BN/Cu(111) and is equally operational for TCNQ. (iii) The energy alignment of the molecular electronic resonances is tuned by the lateral positioning of the 2H-P on BN/Cu(111), which also affects the electronic gap. For high coverage, where extended chiral porous Kagomé network structures evolve, an electronic superstructure is thus imprinted in the 2H-P film.

5.3 Trapping of molecules on BN moiré

To characterize individual porphine molecules on BN/Cu(111) and to study the initial phase of self-assembly, 2H-P was prepared with low coverage at room temperature. Figure 5.1c shows the site specific trapping and formation of small porphine aggregates on the H regions or moirons of the electronic BN/Cu(111) superstructure at low coverage. In contrast to porphine adsorption on Ag(111) (Figure 5.1a) and Cu(111) (Figure 5.1b), where repulsive inter-molecular forces prevent the assembly of aggregates below 0.88 ML, [128, 129] small islands are observed on BN. The nearest neighbor distance in these aggregates amounts to 11.3 ± 0.5 Å. This value is very close to the preferred lateral in-plane separation of two 2H-P molecules calculated by simple molecular mechanics simulations (MM+) that do not include interactions with the substrate. Thus inter-molecular repulsion does not play a decisive role for 2H-P/BN/Cu(111), in contrast to 2H-P in direct contact with a Cu(111) or Ag(111) substrate, where charge transfer has been reported. [128, 129] This is a first indication of an effective electronic decoupling of the porphine from the metallic substrate by the BN spacer-layer. Nevertheless, a considerable amount of isolated molecules is observed, seemingly trapped on the moirons or H areas of the BN/Cu(111) superstructure. Clearly, the 2H-P molecules avoid the V and B regions. A statistical analysis of the 2H-P locations on the moirons reveals a preference for off-center positions (Figure 5.1d, top panel). However, after normalizing the counts with the area available for adsorption, which increases linearly with increasing distance r from the moiron center, a monotonous distribution is observed (Figure 5.1d, bottom panel). Thus the porphine experiences a trapping on the moirons without favored ring-like adsorption sites. This observation is corroborated by molecular manipulation experiments. Electron injection from the stationary STM tip into the lowest unoccupied molecular orbital (LUMO) induces a lateral translation of the 2H-P on the BN moiron. Tracking a molecule through a sequence of jumps visualizes the confinement on the moiron (see Figure 5.1e). Color-coded dots and lines, ranging from black to yellow, represent the trajectory of the molecule.
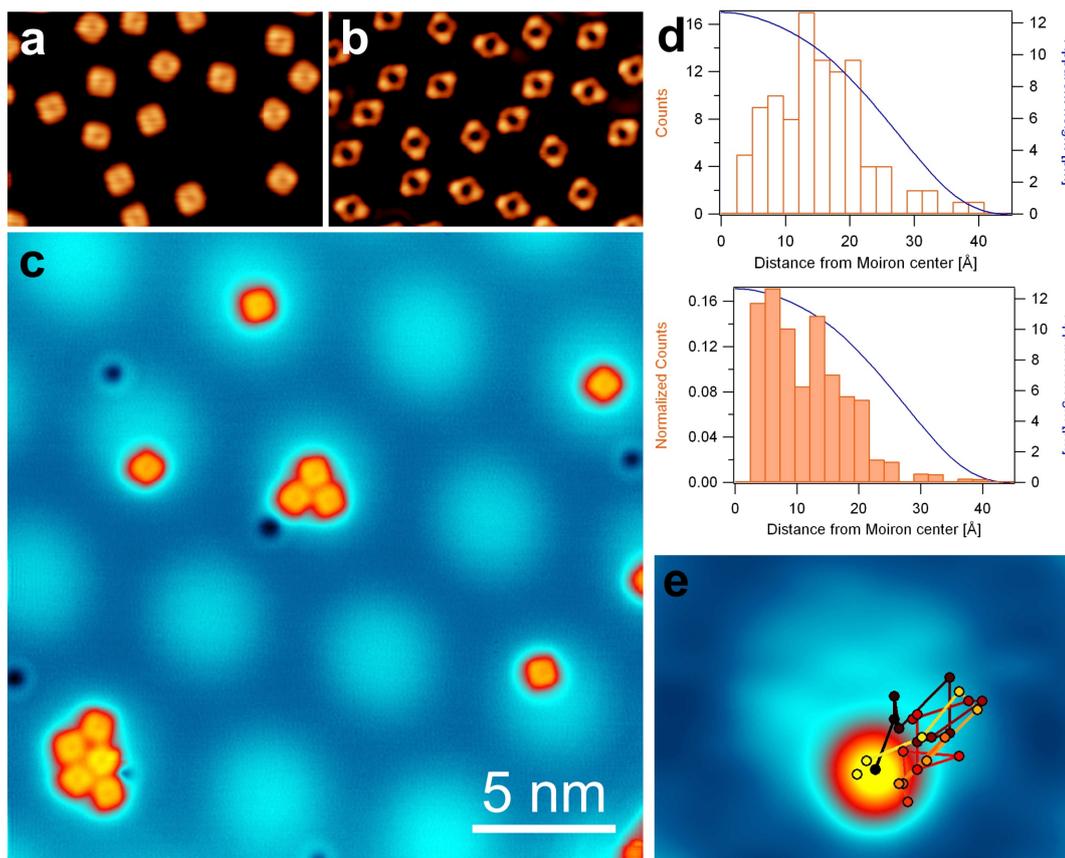
Figure 5.1: Trapping of 2H-Ps on the electronic BN/Cu(111) superstructure. On the metallic Ag(111) (a, V_b = -0.8 V, I = 200 pA) and Cu(111) (b, V_b = -0.1 V, I = 200 pA) surfaces serving as reference systems, repulsive interactions prevent the assembly of porphine aggregates at low coverage. (c) STM image showing the trapping of individual 2H-P molecules (orange squares) and small porphine aggregates on the H areas (or moirons, light blue) of the BN/Cu substrate. The formation of 2H-P islands on the BN is attributed to a reduced electronic coupling of the molecules to the Cu (V_b = 1 V, I = 30 pA). (d) A statistical analysis of the radial positions of 2H-Ps on the moirons reveals a preference for off-center adsorption in the raw data (top panel). Normalizing the counts with the available area however yields a decreasing probability of residence with increasing distance from the moiron center (bottom panel). The blue curve represents an apparent height profile from the center of a moiron to the B region. (e) Jumps of a 2H-P upon injection of electrons. The color-coded dots mark the positions of the molecule, which is trapped on the moiron.

The selective confinement of molecules, clusters or atoms on specific areas of nanostructured surfaces can be triggered by the absolute value of the local workfunction, [116, 130] the strength of van der Waals interactions with the support, [114] the magnitude of vertical dipole moments on polar substrates [23, 107] or lateral electric fields on surfaces exhibiting a corrugated electronic potential. [26, 28] In the present case, the experimentally observed distribution of individual 2H-P molecules on the moiron is consistent with an important role of the absolute value of the local workfunction (compare Figures 4.6b and 5.1d). However, our DFT calculations including vdW corrections show essentially no difference in the binding energy of 2H-P on the local low- and high-workfunction areas corresponding to the $B_{fcc}N_{top}$ ($E_{ads}=$ 1.93 eV) and $B_{hcp}N_{fcc}$ ($E_{ads} = 1.94$ eV) registries, respectively. The interaction energy of 2H-P on the large moiré cell are also rather uniform, ranging between 2.01 and 2.04 eV (See Table in Figure 5.9d). It should be noted that the latter quantity is larger because possible relaxation of the substrate and adsorbate are not accounted for. [151] Irrespective of the precise mechanism, the trapping or confinement, going hand in hand with a spatial ordering of the molecules, is tentatively rationalized with the periodic modulation of the surface potential of the BN/(Cu(111) interface.

5.4 Decoupled molecules on BN

Figure 5.2 shows *dI/dV* spectra along with STM images of a single molecule. A direct comparison of spectra of 2H-P on BN (blue) with reference data of bare BN (red), 2H-P on Ag(111) (green) and Cu(111) (black) is shown in Figure 5.2a. The 2H-P/BN spectrum evidences pronounced resonances at -2.4 V and +1.45 V, in striking contrast to the featureless spectrum of 2H-P in direct contact with a Ag(111) or Cu(111) surface. The unoccupied spectral feature cannot be described by a single peak, but exhibits some fine structure. [The apparent fine structure of the LUMO resonance is influenced by the termination of the STM tip, as seen when comparing Figures 5.2a, 5.3 and 5.8a. The latter evidences a series of side peaks, reminiscent of vibrational excitations detected for molecules adsorbed on insulating layers (see Figure 5.3)] Consequently, we use the slope to define the apparent gap between the resonances, which amounts to about 3.5 V (dotted line in Figure 5,2a). Clearly, the electronic contributions in the 2H-P gap are dominated by the BN/Cu(111) substrate, which accounts for an electronic interface state (red spectrum). [37] The effective decoupling of the 2H-P from the electron-rich metal by the BN is supported

by a negative differential resistance (NDR) regime trailing the unoccupied 2H-P resonance. [152]

As expected from these scanning tunneling spectroscopy data, STM images of 2H-P/BN/Cu(111) show a pronounced bias dependent intramolecular contrast (Figure 5.2b). In the gap, the molecule appears as featureless square representing the geometric outline of 2H-P. At the energies of the resonances, the appearance of the molecule is considerably modified. The STM image representing the occupied state is dominated by four bright protrusions, for the unoccupied resonance a two-fold symmetry prevails. This contrast is in excellent agreement with calculated charge density plots of the highest occupied (HOMO) and lowest unoccupied (LUMO) molecular orbital of an isolated 2H-P molecule. Figure 5.2b compares the STM images (top panel) with the HOMO and LUMO obtained from DFT calculations of an isolated 2H-P molecule (middle panel) and the corresponding constant charge density contours based on EHT simulations (bottom panel). [153] Based on the close resemblance, the resonances identified in the 2H-P spectrum on BN can be assigned to the HOMO and LUMO orbital, respectively.

Our DFT calculations yield a value of 1.93 eV for the electronic gap of isolated porphine, a quantity typically underestimated by GGA methods. Indeed, recent theoretical studies focusing on a precise determination of electronic and optical gaps in organic materials report a HOMO-LUMO gap in isolated porphine of 5.0 eV or 5.2 eV and emphasize the strong excitonic effects in optical spectra. [154, 155] Our experimentally determined electronic gap (3.85 eV peak to peak, 3.5 eV apparent gap) is still considerably smaller than these values, evidencing some interaction of the porphine with its support. Indeed, the binding energy of the HOMO relative to the vacuum level (~6.4 eV) is smaller than the ionization potential of 6.9 eV determined for gas phase 2H-P. [156] [The binding energy of the HOMO relative to the vacuum level is estimated by adding the binding energy of the HOMO relative to the Fermi level (2.4 eV) to the average workfunction of BN/Cu(111) (~4 eV)].
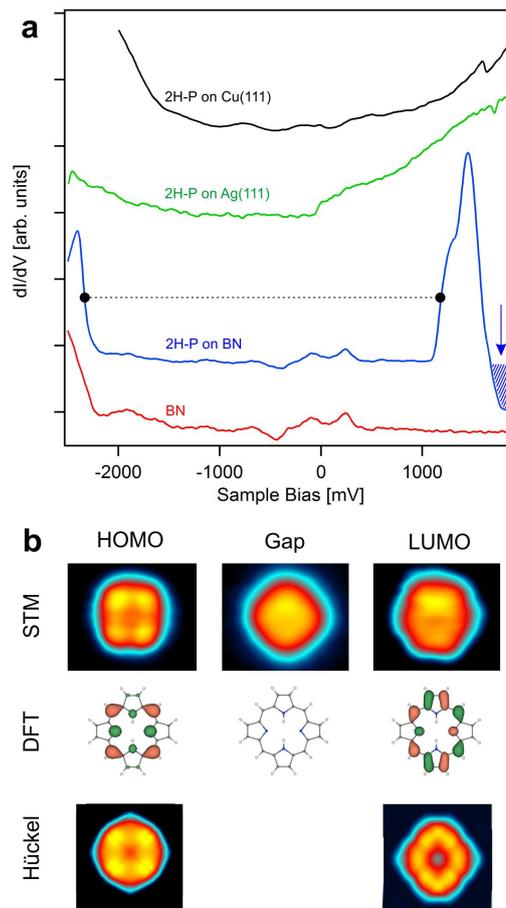
Figure 5.2: Electronic characterization of 2H-Ps on BN/Cu(111). (a) Comparative dI/dV spectra recorded on BN/Cu(111) (red), on the center of 2H-P on Ag(111) (green), Cu(111) (black) and BN/Cu(111) (blue), respectively. While contributions from the surface- and interface states are observed near the Fermi energy (Sample Bias = 0) in all spectra, only the spectrum representing 2H-P/BN/Cu(111) shows pronounced resonances at -2.4 and 1.45 V separated by a gap. The dashed line marks the apparent electronic gap of ≈ 3.5 V. The NDR region highlighted in blue (see arrow) confirms a reduced electronic coupling of 2H-P to Cu. (b) The top panel represents the bias dependent appearance of 2H-P/BN in experimental constant current STM images, recorded in the gap or at the positions of the (un)occupied resonances (HOMO: V_b = -2.45 V, I = 100 pA, gap: V_b = 1 V, I = 30 pA, LUMO: V_b = 1.25 V, I = 30 pA). The STM images are well reproduced by constant charge density contours based on extended Hückel simulations (bottom panel), reflecting the HOMO and LUMO orbitals as calculated by density functional theory (DFT, middle panel). A gaussian blurring was applied to mimic the finite resolution in the STM experiment. See text for discussion.
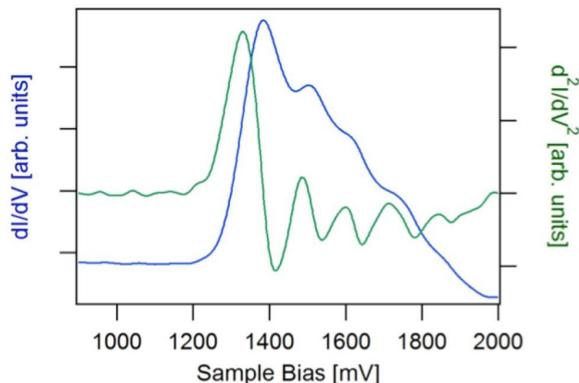
Figure 5.3: *dI/dV* spectrum (blue) recorded on 2H-P/BN/Cu(111). Comparing several data sets (see Figures 5.2a and 5.8a) reveals a variety of fine structures for the LUMO resonance, which we tentatively assign to different configurations of the STM tip. It is important to note that this does not affect the conclusions about the spatial dependence of the level alignment and the electronic gap. We attribute the side peaks and shoulders to vibrational features, [157] well established for molecular adsorbates on insulating layers, rather than to an energetic splitting of the LUMO and LUMO+1 orbitals. The second derivative of the I/V signal (green curve) reveals separations of the side peaks from 100 to 130 mV, well within the range of vibrational modes documented for porphines. [158]
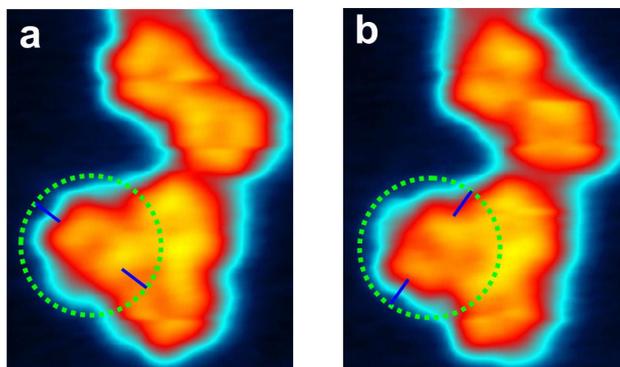
Figure 5.4: Tautomerization in 2H-P/BN/Cu(111). The inner protons can be transferred between two pairs of opposing nitrogens. The position of the central hydrogen pair is reflected in the orientation of the LUMO orbital, i.e. a switching of the protons induces a rotation of the LUMO symmetry by 90°. Indeed, our STM data of 2H-P/BN/Cu(111) recorded at an energy corresponding to the LUMO resonance evidence such switching events (compare (a) and (b). It should be pointed out that a 90° rotation of the 2H-P molecule as origin of the changed LUMO symmetry can be excluded due to symmetry reasons and the observation of the switching in agglomerates (V_b = 1.25 V, I = 30 pA).

All free-base porphyrin systems 2H-P contain two hydrogens in the interior of the tetrapyrrole macrocycle, which can undergo a tautomerization process. [159] Our STM data of 2H-P/BN/Cu(111) indeed show the tautomerization switching, reflected in a 90° rotation of the LUMO symmetry, [133] thus corroborating the resolution of the LUMO (see Figure 5.4).

5.5 Morphology of island growth on BN

With increasing molecular coverage, the average size of the 2H-P aggregates confined to the moirons increases. Figure 5.5a shows a highly ordered array of 2H-P islands at a coverage of about 0.4 monolayers (ML) on a BN/Cu(111) domain characterized by a superstructure periodicity of 7 nm. [The monolayer is defined as the entire surface coverage by the Kagomé network (see Figure 5.7g)] The templating effect of the BN/Cu(111) substrate is clearly discernible and is also reflected in the fast Fourier transform (FFT) of the image (Figure 5.5b). The sharp hexagonal pattern at the center represents the inter-island distances. Remarkably, each moiron hosts an extended, self-assembled 2H-P island. An inspection of the islands' shapes and sizes reveals repeating morphologies including a prominent hexagonal assembly formed by eighteen molecules exposing a central vacancy (examples are marked by colored hexagons in Figure 5.5a). Indeed, the island-size distribution plot based on the analysis of 160 moirons (>2200 molecules), normalized according to scaling theory, shows a clear preference for eighteen-molecule clusters (see Figure 5.5d). Here, N_S describes the island density, θ the coverage, $S\,(<S>)$ is the (average) number of molecules per island. [130, 160] The strong contribution for a normalized island size $S/<S>= 1.3$ represents the eighteen-molecule clusters, corresponding nearly exclusively to the porous hexagonal assemblies. The red solid line shows the calculated size distribution from scaling theory for random nucleation (i = 1) on an isotropic substrate. [130, 160] Clearly, the experimental distribution is narrower, i.e., has a higher size uniformity thus confirming the templating effect of the electronic BN/Cu(111) superstructure. Assuming a perfect confinement of deposited 2H-P molecules on the moiron cells, a binomial distribution of the island sizes is expected. [130] The cyan curve in Figure 5.5d bases on the binomial distribution $P_k = \binom{n}{k} p^k q^{n-k}$ relying on the experimental parameters ($p = \theta = 0.4$ is the coverage, $q = 1 - \theta, k$, is the island size and $n = 33$ is the number of molecules in a super-cell (white rhombus in Figure 5.5a)). The agreement with the experimen-

tal size distribution is reasonable, notably concerning the width. The calculated standard deviation $\sigma = (q/np)^{1/2}$ of 0.21 compares well with values reported for templated, self-organized growth. [130] However, the binomial distribution naturally fails completely in describing the preference for the eighteen-molecule cluster. To rationalize the abundance of these porous hexagon-shaped assemblies, all the observed island sizes and shapes where analyzed regarding two features: First, the average number of nearest neighbors per molecule in an island and second the number of peripheral molecules interacting with only two neighbors, thus representing an "open shell" structure. In comparison to the porous assemblies formed by 15, 16 and 19 molecules, the porous hexagon includes no *peripheral* molecules and features the highest average number of nearest neighbors, making it the favored configuration. As discernible in Figure 5.5, the eighteen-molecule clusters are chiral, i.e., two mirror symmetric assemblies are observed on the surface (examples are marked by the green and red hexagon, respectively). Figure 5.5b (right side) shows a structural model of one of the two chiral assemblies (green hexagon). Indeed, their existence is also revealed in the FFT. Twelve diffuse spots are detected at larger k values reflecting the inter-molecular distance (highlighted by circles in Figure 5.5b, FFT image). From the hexagonal packing within one island, only six spots are expected. The twelve spots emerge from the coexistence of the two chiralities, which are due to the two equivalent possibilities to arrange two aligned 2H-P molecules relative to each other. Figure 5.5c shows a zoom in on a mirror symmetric chiral pair of hexagonal assemblies, marked by red and green borders.

It should be pointed out that the above analysis represents one specific BN/Cu(111) domain. Nevertheless, the conclusions about the templating function are generally valid for all superstructure periodicities and moiron sizes observed (see for example Figure 5.1 and Figure 5.7). Interestingly, the central vacancy, having a footprint of one 2H-P molecule, is not a common feature of all moirons: Some assemblies are dense-packed and larger moirons can host aggregates with several individual off-center vacancies (see Figure 5.6a). Although we cannot clarify in detail the driving force for the vacancy formation, the porous hexagonal units are the building blocks for extended 2H-P islands prevailing at higher coverage *(vide infra)*.
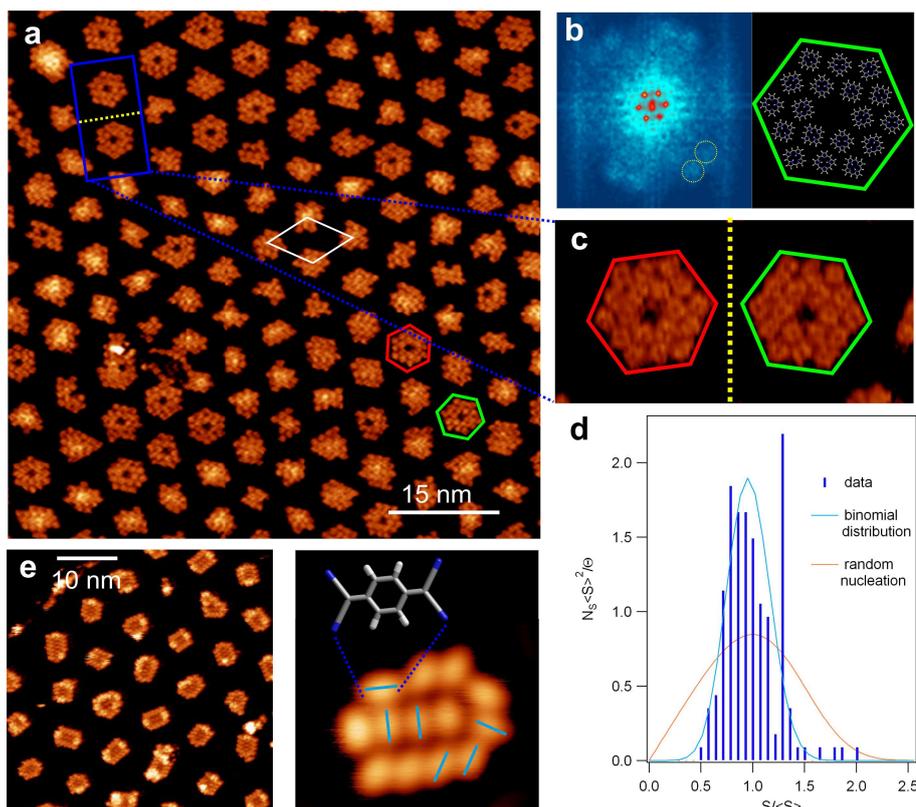
Figure 5.5: Templating functionality of BN/Cu(111) and island morphology. (a) STM image revealing the formation of extended self-assembled 2H-P islands at intermediate coverage confined on the moirons (V_b = 1.0 V, I = 48 pA). The most abundant assemblies, hexagonal eighteen-molecule islands featuring a central cavity, are marked by the green and red hexagons. (b) FFT image to highlight the structural order in (a). The six inner spots (red) reflect the order of the array, i.e. the arrangement of the assemblies. The twelve outer spots (highlighted by yellow circles) represent the order within the assemblies, i.e. the arrangement of the molecules and the chirality (see text for details). A model of one of the chiral hexagons (green) is shown in the right panel. (c) A zoomed and rotated segment from (a, blue rectangle) exhibits the mirror symmetric pair of chiral hexagonal assemblies (red and green). (d) Normalized island-size distribution plot for a coverage corresponding to a), clearly showing the dominance of the eighteen-molecule assemblies (corresponding to S/<S> = 1.3, see text for discussion). The experimental distribution is clearly narrower than the red random nucleation curve, confirming the templating functionality of the electronic superstructure of the BN/Cu(111) interface. The cyan curve shows a binomial distribution representing perfect confinement. (e) Formation of arrays of TCNQ aggregates on BN/Cu(111) after room temperature deposition (V_b = 1.6 V, I = 21 pA). The right panel shows the molecular arrangement within one specific island and a structural model of TCNQ (V_b = 0.3 V, I = 33 pA). The solid lines (cyan) highlight the different coexisting TCNQ orientations and the relative molecular positions.

The potential of BN/Cu(111) as a template is also evident for a structurally and electronically distinctly different adsorbate, namely TCNQ. Figure 5.5e evidences the formation of arrays of TCNQ assemblies after room temperature deposition, analogous to the 2H-P situation. STM images of individual islands (e.g. Figure 5.5e, right panel) reveal the packing scheme of these aggregates, reminiscent of nitronaphthalene supermolecules reported on a reconstructed Au surface. [161] Judging from the molecular dimensions, the average planes of the TCNQ units adsorb parallel to the surface. Distinct molecular orientations differing by 30°, 60° or 90° coexist, representing specific inter-molecular coupling motifs exhibiting a nearest neighbor separation of ≈ 8 Å, with a minimal N...H distance of 3 Å. A simultaneous expression of orthogonal (90°) and side-by-side (0°) arrangements was observed for TCNQ/Cu(111), [162] while parallel (0°), but offset TCNQ alignments are reported on other coinage metal surfaces. [163–165] These homogeneous metal substrates however never supported the organized growth of TCNQ arrays, but yield extended islands at submonolayer coverage. A templated TCNQ growth was achieved on graphene/Ru(0001), where the close match between moiron extension and molecular size results in individual TCNQ units at low coverage. [25]
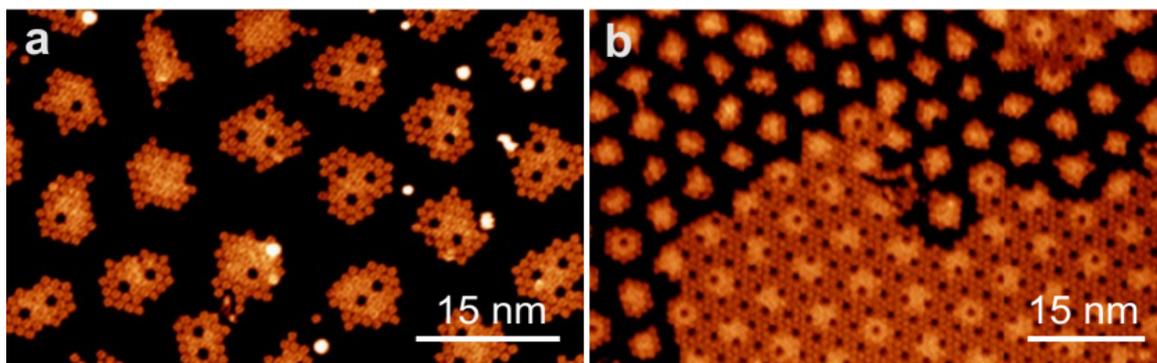
Figure 5.6: Growth of 2H-P islands on BN/Cu(111). (a) BN domain exhibiting a large moiré periodicity of ≈ 12 nm hosts extended 2H-P islands incorporating multiple vacancies in off-center positions, but also dense-packed assemblies ($V_b = 1$ V, I = 48 pA). (b) Overriding of the templating effect at high coverage. The phase transition from ordered array growth to extended island assemblies occurs around 0.4 ML for the presented superstructure. At the selected voltage ($V_b = 1.033$ V), the Moirons are clearly visualized also within the extended 2H-P island.

At coverages exceeding ≈ 0.4ML, the 2H-Ps start to form extended highly regular porous networks with a rhombic unit cell (side length of 3.2 nm) including six molecules (Figure 5.7g, yellow rhombus). The hexagonal eighteen-molecule cluster

abundant at intermediate coverage is observed as repetitive motif in the porous network (green hexagon) thus demonstrating some hierarchy in the assembly. A close inspection of the extended assemblies reveals their chiral Kagomé-type structure (highlighted in cyan in Figure 5.7g). [166] A similar structure was reported for phthalocyanines on a graphene-based moiré pattern. [137] Obviously, the templating effect of the BN superstructure can be overridden provided the number of molecules is large enough. This is neatly apparent in Figures 5.6b and 5.7a showing phase boundaries between the confined assemblies and the extended network.
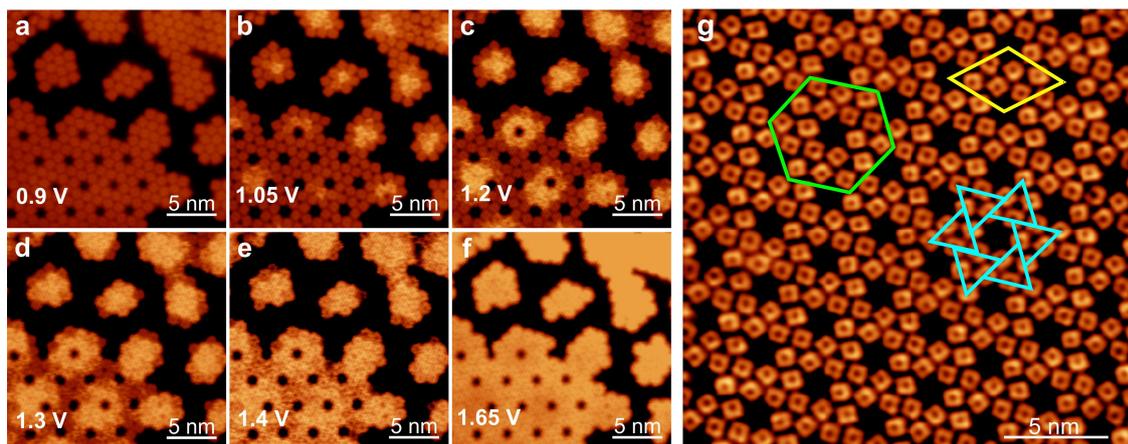
Figure 5.7: Bias and position dependent appearance of 2H-P on BN/Cu(111). (a-f) STM image sequence recorded with increasing bias voltage. The area represented shows the coexistence of an extended network with the ordered island phase (I = 30 pA, identical color scale). The modified appearance with increasing bias is assigned to electron transport via the LUMO. The lateral contrast variation is induced by the corrugated surface potential of the BN/Cu(111) interface (see text for discussion). (g) Extended porous 2H-P Kagomé network on BN/Cu(111) at high coverage (V_b = 1.0 V, I = 50 pA). Here, the templating effect is overridden. The assembly includes the hexagonal eighteen-molecule motif (green hexagon, compare Figure 5.5) and is characterized by a rhombic unit cell (highlighted in yellow).

5.6 Spatial modulation of molecular orbitals

In Figure 5.7a-f, an image sequence recorded with increasing positive sample bias voltage (representing unoccupied electronic states) is shown. Clearly, the appearance of the 2H-P depends both on the applied voltage and the lateral position. At 0.9 V, all molecules appear with an identical contrast. At 1.05 V, the 2H-Ps near

the center of the moirons exhibit an increased apparent height. Here, the position of the moirons or H areas in the extended network is deduced from the positions of the individual islands. While increasing the bias between 0.9 to 1.65 V, this brighter appearance of the molecules gradually spreads outwards, i.e. radially away from the moiron centers (Figures 5.7a-f). At 1.65 V all 2H-Ps appear with an identical contrast again, which however is different from the situation at 0.9 V. To clarify this position- and bias-dependent contrast, *dI/dV* spectra were recorded above the center of porphines located at characteristic spots of the BN/Cu(111) superstructure. Figure 5.8a compares spectra on the center of the "hill" (blue), "in-between" (green) and the "bridge" (red), which show significant shifts of the HOMO and LUMO resonances. Importantly, the LUMO related peak of the molecules on the "hills" is shifted by about 300 mV to lower energy as compared to the "bridge", while the spectral shape is conserved. This explains the spatial-energy variation in appearance of the 2H-P molecules: First, the increased apparent height is assigned to tunneling into the LUMO of the 2H-Ps. Second, the radial increase in brightness with increasing bias voltage is explained by the upshift of the LUMO resonance with increasing distance from the center of the moiron.

We attribute these LUMO shifts to the smooth spatial modulation of the local surface potential of the electronic BN/Cu(111) superstructure (compare Figure 4.6b), where we observed an energy variation in the field emission resonances of about 300 meV between the H and V or B areas, with the lowest local workfunction on the moirons. The mechanism behind the energy shifts is consistent with a vacuum level alignment of the LUMO, as sketched in the diagrams reproduced in Figure 5.8c representing the energy level alignment for the B (red) and H (blue) positions. The LUMO energy is given by the electron affinity (E_A) relative to the vacuum level of the sample, which is defined by the local workfunction. Assuming E_A to be constant, the reduced local workfunction on the moirons (Φ_H, blue) shifts the LUMO closer to the Fermi level, i.e., electrons can tunnel into the LUMO at lower bias voltages as compared to the V situation (Φ_B, red). This vacuum level alignment of molecular orbitals is consistent with an efficient electronic decoupling of the 2H-P from the metal support. Nevertheless, the voltage drop across the BN spacer-layer does not drastically affect the level alignment. A variation of the tip-sample distance by 2 Å shifts the LUMO resonance by less than 50 mV, which is much smaller than the value of 300 mV reported above. A very recent study addressing phthalocyanines on a graphene/BN support also reports varying energies of molecular orbitals and

assigns this effect to an spatially dependent electronic doping of the molecules. [167] For 2H-P/BN, we do not consider relevant charge transfer to/from the molecules as the 2H-P frontier orbitals do not contribute significantly to the density of states at the Fermi level (see Figure 5.2).
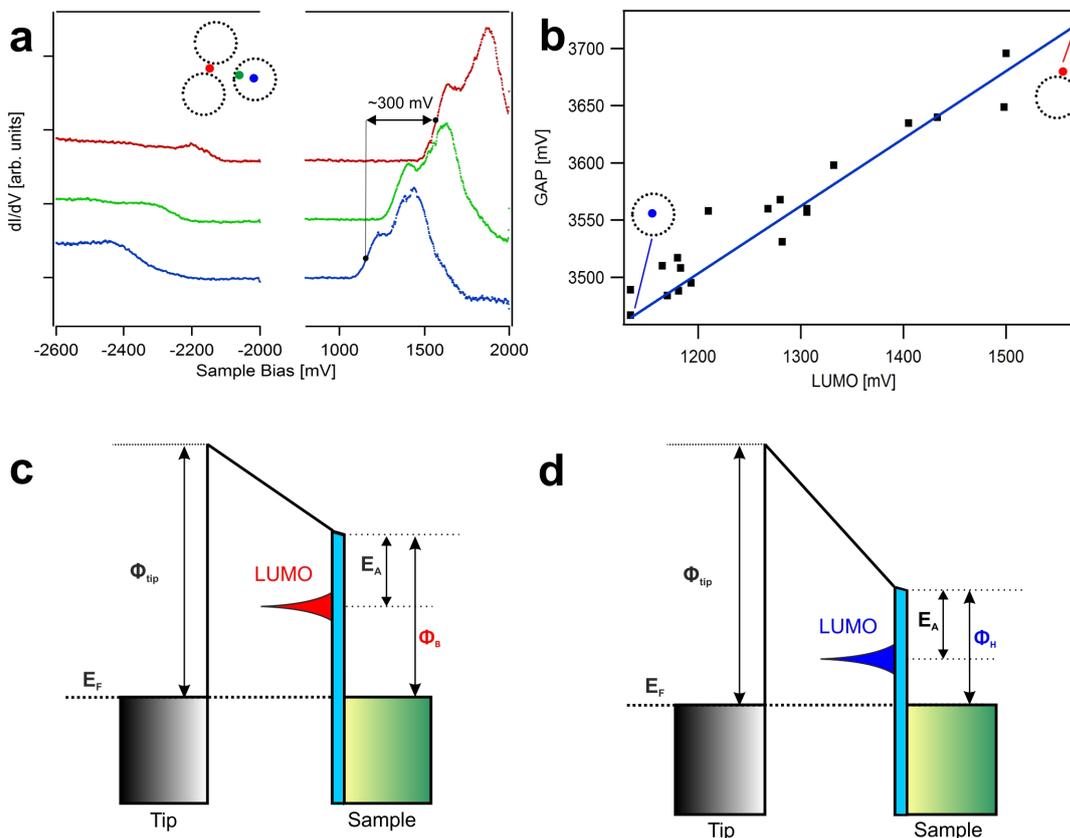
Figure 5.8: Position-dependent energy level alignment of 2H-P on BN/Cu(111). (a) *dI/dV* spectra recorded above the center of porphines positioned on characteristics sites of the superstructure: Center of the moiron (blue marker and spectrum), rim of the moiron (green marker and spectrum), and B area (red marker and spectrum). The energy of the LUMO varies by about 300 mV between the H and V positions. (b) Change of the HOMO-LUMO gap of 2H-P for different positions on the superstructure (see text for discussion). (c-d) Models sketching the tip-sample interface for the high (c, H) and the low local workfunction areas (d, V, B). A vacuum level alignment of the LUMO combined with a constant electron affinity EA brings the LUMO energy on the moiron closer to the Fermi level and thus explains the observed shifts in the *dI/dV* spectra as well as the spatially inhomogeneous contrast in STM images recorded between 1 and 1.4 V (compare Figure 5.7). (See text for further discussion).

The spatially dependent energy shift is also reflected in the HOMO resonance, which appears as a distinct step-like feature in the negative sample bias regime (Figure 5.8a). It shows the same trend as the LUMO. However, the HOMO-LUMO gap varies depending on the 2H-P position on the superstructure. The molecules have the smallest gap on the "hills" and the largest on the "valleys". Figure 5.8b evidences a linear dependence of the HOMO-LUMO gap on the LUMO position and the lateral position, respectively. Thus, a rigid band shift due to a vacuum level alignment does not precisely describe the real situation, despite being a reasonable approximation. We tentatively assign the variation of the gap to subtle modulations of the molecule-substrate interactions, i.e., to screening effects. [168, 169] Compared to the high local workfunction areas, the low local workfunction regions (H) facilitate an electronic interaction with the underlying metal and thus enhance the screening, which is reflected in a reduced HOMO-LUMO gap. Indeed, the confinement of 2H-P on the moirons at low and intermediate coverage, evidencing an increased interaction with the support, is consistent with this interpretation.

5.7 Theoretical calculations of 2H-P on BN

The electronic structure of 2H-P on various positions across the moiré cell as obtained from DFT calculations shows a similar behavior. We have previously demonstrated that the spatial variation of the local workfunction can be rationalized with the modulation of the adsorption registry of BN on Cu(111). [170] Here we placed the molecule on 6 positions along the diagonal of the moiré cell where the electronic corrugation is strongest (Figure 5.9a). We plot the p_z density of states, projected on the C and N atoms at each of these positions (Figure 5.9b) to elucidate the local variation of the electronic structure. The positions of the HOMO and LUMO are modulated depending on the placement of the adsorbate. In particular, at point I ("hill" H) the orbitals are shifted to the lowest and at point IV ("valley" V) to the highest energies. The overall spread of the orbital energies amounts to 100 meV, noticeably smaller than what is observed in the STS. Looking at the LUMO positions (projected onto C atoms) more closely (Figure 5.9c), it becomes evident that the orbital energies are strongly linked to the surface electrostatic potential (ESP), and thus to the local workfunction at the height of the porphine molecule. The LUMO position closely follows the variation in the ESP, where 2H-P in positions with a low ESP shows a LUMO peak at lower energies, while high ESP causes an upshift of the

LUMO. Qualitatively, the DFT results reproduce the LUMO shifts measured with STS (see Figure 5.9a), while the overall variation is smaller by a factor ~3. This is consistent with the underestimated magnitude of the electronic corrugation. Also spatially the calculations agree well with the points sampled by STS, finding the lowest LUMO for the H area and an increase as one moves away from the hill.
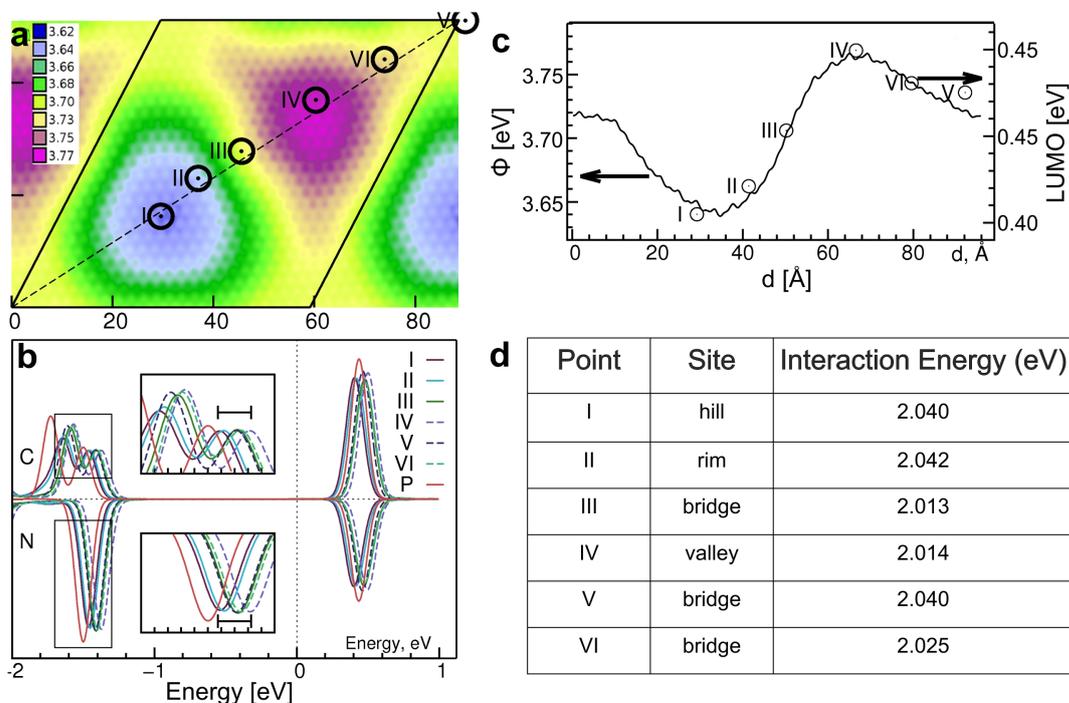
Figure 5.9: DFT investigation of porphine at several adsorption sites on the BN/Cu(111) moiré.DFT investigation of porphine at several adsorption sites on the BN/Cu(111) moiré. (a) Location of six adsorption positions where the 2H-P molecule was placed, superimposed on a map of the local workfunction (in eV) at the approximate height of the 2H-P molecule (3.3 Å above BN surface). (b) Projected density of states (p_z) of porphine-C (top) and porphine-N (bottom) atoms with 2H-P placed at various positions as indicated in (a). The PDOS of 2H-P in vacuum is plotted for comparison (curve "P"). Insets show zooms of the framed HOMO regions, scale bar indicates 100 meV. (c) Local workfunction (eV, line) across the diagonal of the moiré cell and positions of the LUMO maximum (eV, points) for six positions along this diagonal. (d) Interaction energy between molecule and substrate at the various locations of the BN/Cu(111) superstructure. [171]

5.8 Experimental procedures and theoretical methods

The BN spacer-layer was prepared by chemical vapor deposition (CVD) of borazine $(HBNH)_3$ following a protocol described in detail in previous chapters and reports. [37, 54, 55] The 2H-P (Frontier Scientific, purity > 95%) and TCNQ (Aldrich, purified by the Ruben group at Karlsruhe Institute of Technology) molecules were deposited using organic molecular beam epitaxy (OMBE) from a quartz container held at 470 K or 390 K, respectively. During deposition the BN/Cu/(111) substrate was usually kept at room temperature. All STM images were recorded in constant current mode and the differential conductance (dI/dV) spectra or scanning tunneling spectra were taken using a lock-in amplifier (f = 969 Hz, ΔVrms = 18 mV). The feedback loop was closed for the field emission resonance measurements. [37] The FFT and the STM images were processed using the WSxM software. [120]

Complementary DFT calculations were carried out in order to increase our understanding of the system. Our approach uses the Gaussian plane wave formalism as available in the QuickStep module in the CP2K package [122] and a computational set-up that we have described in previous work. [37, 151, 170] Double-Zeta MOLOPT basis sets [125] were used for all elements, with a plane-wave cutoff of 500 Ry for the electron density. The revPBE [123] exchange-correlation functional was used together with the DFT-D3 dispersion correction. [124] Projected Density of States (PDOS) curves are smoothed with a Gaussian convolution with a width of 0.05 eV for better readability and comparability. Using this set-up the HOMO and LUMO of an isolated 2H-P molecule were calculated and are presented in Figure 5.9b. The appearance and qualitative features of the orbitals are robust to changes of the exchange-correlation functional and variations of the geometry. The plots were generated using the VisIt suite, version 2.6.2. [172] Two complementary approaches were used to model the adsorption system. Firstly, porphine was placed atop commensurate BN/Cu(111), with the monolayer in different registries [151] ($N_{top}B_{fcc}$, $N_{fcc}B_{hcp}$) in order to model the different environments of the moiré layer [170] Subsequently full geometry optimizations of these systems were carried out. Secondly, to probe the properties of porphine on a large moiré cell we used a 24x24 rotated BN layer on a 23x23x4 Cu(111) slab, as presented previously. [82] The porphine was placed at the "optimal" height determined from the geometry relaxation on various lateral positions on above the monolayer (Figure 5.9) and energy calcu-

lations were carried out. In all but two instances, the residual average force on the porphine molecule was smaller than 10-4 Ha/Bohr. Where this was not the case, the vertical distance of the porphine was rigidly adjusted by at most 0.1 Å until the forces were below that threshold. Due to the prohibitive computational cost of full geometry optimizations of such a large system this manual approach serves as an acceptable substitute.

5.9 Conclusion

In conclusion, we presented a comprehensive STM/STS characterization of an archetypal porphyrin compound on an electronically nanostructured BN/Cu(111) support. As corroborated by complementary DFT modeling, the ultrathin BN spacer-layer introduces manifold new prospects as compared to conventional adsorption on metal supports. A reduced electronic coupling of 2H-P to metallic states is evidenced by the opening of an electronic gap, the resolution of frontier orbitals in STS and STM, enabling the visualization of the tautomerization-induced LUMO-switching, and the electronic level alignment. Coverage dependent studies show a trapping and ordering of 2H-P on the low local workfunction regions of BN/Cu(111). At intermediate coverage, this templating effect induces the unprecedented organized growth of ordered arrays of molecular assemblies, both for 2H-P and distinctly different TCNQ adsorbates. At elevated porphine coverage, extended porous chiral Kagomé networks are formed. Importantly, the lateral modulation of the surface potential at the BN/Cu(111) interface induces a periodic, spatial modulation of the energy of 2H-P frontier orbitals. This opens up the opportunity to steer the level alignment and to tune the electronic gap of surface anchored functional molecules. Thus, as exemplified by the 2H-P/BN/Cu(111) model system, the electronically corrugated BN/Cu(111) substrate introduces a fascinating potential landscape, making it a unique template to position adsorbates or fabricate functional nanostructures.

6 Two-Level Spatial Modulation of Vibronic Conductance in Conjugated Oligophenylenes on Boron Nitride

Intramolecular current-induced vibronic excitations are reported here in highly ordered monolayers of quaterphenylene dicarbonitriles on an electronically patterned Boron nitride BN/Cu(111) platform. A first level of spatially modulated conductance at the nm-scale is induced by the substrate. Moreover, a second level of conductance variations at the molecular level is found. Low temperature scanning tunneling microscopy studies in conjunction with molecular dynamics calculations reveal collective amplification of the molecule's inter-phenylene torsion angles in the monolayer. Librational modes influencing these torsion angles are identified as initial excitations during vibronic conductance. Density functional theory is used to map phenylene breathing modes and other vibrational excitations which are suggested to be at the origin of the sub-molecular topographical features during vibronic conductance.

6.1 Introduction

Nanoscience endeavors to unravel emerging properties and to control matter at the atomic scale. In the context of (supra)molecular engineering on surfaces, [7, 173] the focus has been to study and use atoms and functional molecules to design nanostructures suitable for technological applications. [174] Thus, a crucial step towards molecular-level device elements is the control over the molecular assembly's photonic, phononic, electronic, magnetic properties and combinations thereof. With

the advent of surface-confined molecular wires such as graphene nanoribbons, [175] polyphenylenes [176] and polyfluorenes, [177] the challenge is to establish functional properties in well-defined nanoscale environments. By employing spacer-layers like alkali halides, [21, 178, 179] oxides, [132, 180] or boron nitride, [37, 56, 66, 171] adsorbate−substrate electronic coupling can be controlled. For instance, we have previously described BN grown epitaxially on Cu(111) where the sp^2sheet is topographically planar but simultaneously presents a continuous spatial local workfunction modulation, [37] featuring distinct moiré patterns (with electronic "hills" and "valleys").

By-design interfaces make it possible to investigate isolated electromagnetic molecular perturbations, such as electron− phonon coupling [181–185] and polarons. [186–188] Thus, tunneling spectroscopy of single molecules on insulating layers has emerged as a powerful method for investigating current-induced vibronic, [157, 189, 190] and even rotational [191, 192] excitations down to the sub-molecular level. However, systematic studies in molecular films of organic semiconductors have not been reported though being critical for the optimization of transport [193] and energy harvesting. [194, 195] The study of organic semiconductors on electronically corrugated substrates might grant access to new strategies in lithography-free nanopatterning of (spin-)electronic properties as means to in situ fabrication of complex organic machinery and devices.

Here we explore the subtle interplay of 2D self-assembly, vibrational and electronic properties, notably including nanoscopic evidence for current-induced librational excitations, with exemplary quaterphenylene dicarbonitrile (QD) layers on an electronically corrugated BN/Cu(111) platform. Librations, or swaying motions, originate mainly from hindered rotational modes. These modes contribute to [196] and often stand synonymously [197, 198] for interphenylene torsion modes when polyphenylene species are considered (see the schematics in Figure 6.1). Control over intermolecular torsions in conjugated polymers is crucial for current organic technology. [199, 200] Regarding interfacial systems, librational motions have been invoked for hydrogen-bonded water layers [201] that were assessed by molecular dynamics simulations of two-dimensional networks on mica. [202] They are also important in Raman-spectroscopy investigations of adsorbed organic layers [203] and more recently were probed in the methyl-Si(111) adlayer system by helium atom scattering. [204] Moreover, frustrated molecular rotations induced by inelastic tunneling have been associated with librations and analyzed at the single-molecule level. [205]

Following the deposition of QD on BN/Cu(111), our STM studies reveal a densely packed chevron assembly featuring a zigzag motif due to alternating torsions of the phenylene rings, as confirmed by molecular dynamics (MD) simulations. The low-temperature tunneling conductance is found to vary at two different spatial length scales. First, due to the electronic corrugation of the BN/Cu(111) support, [37] the signature associated with the lowest unoccupied molecular orbital (LUMO) in the molecular layer, is modulated at the nm-scale. Second, we find molecular scale variations of the conductance, which can be rationalized with the calculated DFT dipoleweighted normal-mode vibrational spectrum. Our studies notably signal that current-induced vibronic excitations [157, 189, 190] can be strongly localized at the intramolecular level. Therefore, our platform featuring two-level spatial modulation of conductance represents a unique scaffold offering modulation of both nanoscopic and sub-molecular charge transport.

6.2 Assembly of QDs on BN spacer-layer

The employed molecular species QD (NC-Ph4-CN; Figure 6.1a) belongs to the class of para-substituted oligophenylenes. Originally intended for exploring interfacial metal-directed assembly, [16] their suitability for purely organic organized thin films became manifest. Systematic investigations revealed that QD supramolecular layers are well ordered, featuring large, regular domains on, for example, Ag(111) [166, 206] in contrast to their non-substituted phenylene counterparts. [207] Figure 6.1b,c show high-resolution low-temperature STM images of the self-assembled pattern found upon evaporating a (sub)monolayer of QDs on BN/Cu(111). Structurally different from the rhombic packing on Ag(111), [166, 206] the present assembly features highly regular ordering, with a coverage-independent chevron structure. A close inspection of the high-resolution STM image reveals that every other row along unit cell's vector b in the assembly is not equivalent and two distinctive molecular units exist. Whereas the first species appears straight (black line in Figure 6.1b,c), the second molecule exhibits a zigzag shape (blue arrows, Figure 6.1b,c), with each (blue) central arrow segment corresponding to a biphenylene's diagonal. This observation in conjunction with comparative studies (see Figure 6.2) suggest that the zigzag shape arises from larger interphenylene torsion (IPT) angles between phenylene rings in every second QD molecular row.
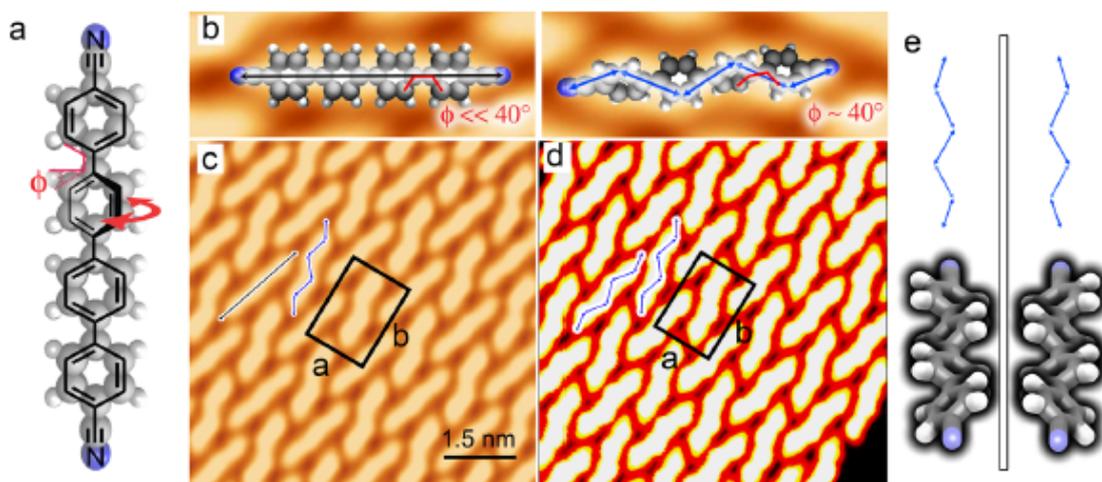
Figure 6.1: Molecular self-assembly of QD on BN/Cu(111) investigated by STM and MD.Molecular self-assembly of QD on BN/Cu(111) investigated by STM and MD. (a) Structural formula of QD showing phenylene libration (arrow) and interphenylene torsion angle (Φ). (b) DFT optimized molecular models showing two stationary states with different interphenylene torsion angles (Φ). (c) STM image of QDs at the BN/Cu(111) interface at 8 K. Unit cell a = 14.2 ± 0.2 Å, b = 19.9 ± 0.5 Å, (a, b) = 88°. (V_b = 1.0 V, I = 40 pA). (d) Isosurface rendering of the molecular orbitals from AM1 calculations of a QD monolayer obtained after 20 ns MD simulations (MMFF force field) at 300 K followed by a fast 5 ns quenching to 10 K. Unit cell parameters a = 14.110 Å, b = 20.500 Å, (a, b) = 90°. (e) Interphenylene axial chirality: Two zigzag enantiomers are not superposable with 3D symmetry operations when keeping the torsion angles fixed.

The observed QD's zigzag shape can be reproduced by preparing 200×100 nm^2 QD monolayer at 300 K through nanosecond-long MD simulations followed by fast quenching to 10 K at rates of 5 K ps^{-1}. The simulations make use of the MMFF46 force field and an underlying substrate consisting of a BN layer mimic (see section 6.5, Experimental Procedures). Quantitatively reproducing the zigzag shape follows by rendering the isosurfaces of the AM1 molecular orbitals coefficients at z = 4 Å from the BN layer. Figure 6.1d depicts the rendering of a monolayer section from the MD simulation. In contrast to the experiment, every other molecular row in the simulation has the same IPT angle amounting to 39 ± 2°. As such, only zigzag molecular shapes are observed in the MD simulation. Similar IPT angles were already reported for molecules with six— phenylene backbone (NC-Ph6-CN) in multilayer films. [206]The present joint MD and STM insights point toward IPT angles alternating between lower (straight species) and close to 40° (zigzag

species) within every other row. We tentatively assign the homogeneous phase in the MD simulations to small-ensemble energy differences whereby epitaxy or entropical contributions breaking the IPT inter-row symmetry are not reproduced by the model. It is important to note that alignment of only one zigzag enantiomer (see Figure 6.1e) along the unit cell vectors is found within a few nanoseconds of MD simulations (from an initially prepared fully planar QDs highly ordered layer see Figure 6.2). In other words, in the MD simulations, every QD and, thus, the assembly acquires axial chirality since IPT angles are frozen and not free to vary (librate) at low temperatures without external excitations. Because the MD reveals that each close-packed zigzag structure transfers and amplifies its IPT angles to every neighbor across the monolayer, this constitutes the first experimental and MD example of amplification of axial chirality, adding a novel feature to interfacial chiral organizations.

Additionally, the BN/Cu(111) substrate with its surface potential modulation was shown to have templating effect on free-base porphine molecules. [171] However, the QDs are found not to be confined on the moiré hills of the BN substrate, regardless of the coverage applied. This can be empirically associated to the fact that the inter-molecular interaction between QDs [208] is greater than the molecular interaction with the BN substrate modulation. [37, 171] For molecules like QDs, the binding energy between a terminal carbonitrile and the phenylene rings of adjacent molecules are shown to be around 220 meV. [208, 209] In an assembly, the QDs interact at both ends to adjacent molecules, thereby doubling the binding energy. Thus the inter-molecular attractive interaction is dominant in comparison to trapping effects of the electronically modulated BN substrate: the molecules favor long-range untemplated assembly. On a metal substrate, due to significant adsorption energy increase the molecules adhere to a planar adsorption registry. This is manifested for linear polyphenylene dicarbonitriles (NC-Phn-CN; n = 3,4,5…..) on Ag(111) through planar interaction of the phenylene rings with the substrate plane. This was confirmed by previous experimental studies for sub-monolayer coverages where it was shown that on Ag(111), NC-Ph3-CNs lie flat on the surface, and for the QD a IPT angle of less than 10° between the phenylene rings and the substrate plane has been suggested. [166, 206]
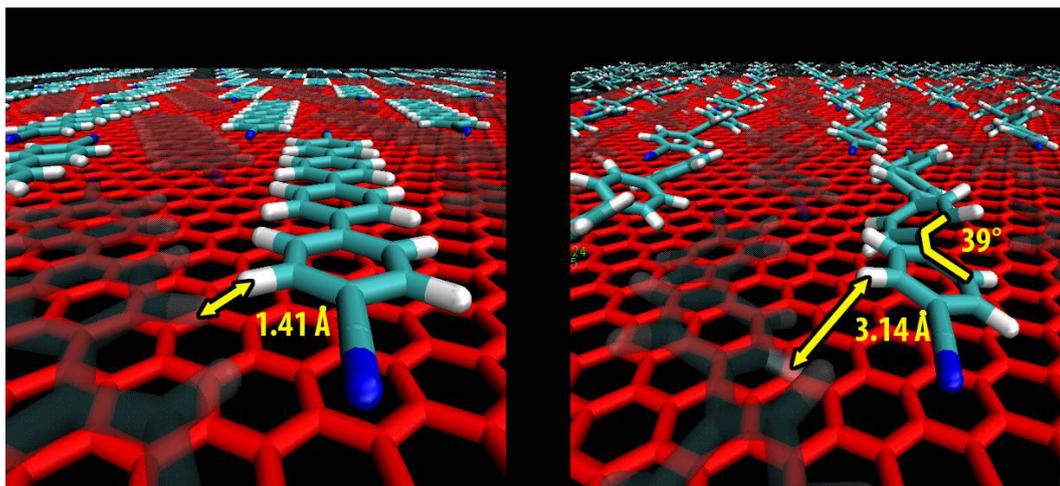
Figure 6.2: Comparison of initial crystalline monolayer preparation before and after MD simulations.Comparison of initial crystalline monolayer preparation before and after MD simulations. Constructed 270-QDs molecular crystal using unit cell parameters a = 14.11 Å b = 20.5 Å (a,b) = 90°. The unit cell of the underlying BN monolayer amounts to a = 2.54 Å, (a,b) = 120°. Image of the QD crystal obtained after 20 ns molecular dynamics simulations at 300 K followed by fast 5 ns quenching to 10 K. Every second molecule is shaded for clarity. [210]

Furthermore, the flat adsorption preference on a metal substrate is also supported by previous theoretical studies where a benzene ring (consider it a single phenylene ring) is shown to have nearly twice the adsorption energy on noble metals (Au and Ag) substrates [211, 212] as compared to graphene. [213] This is relevant to our BN substrate, as graphene is reported to have similar adsorption energies to BN. [214] Besides these pertaining experimental and energetic considerations, the unit cell in Figure 6.1 in the main text cannot accommodate flat-on molecules, as modeled in Figure 6.2. The flat-on monolayer in Figure 6.2 shows that planar QDs are highly sterically hindered with H-H distances between neighbor molecules of 1.4 Å. In order to lie flat with a flat conformation featuring neighbor H-H distances of at least 3 Å, the unit cell should increase by more than 20%. This has been previously suggested for longer oligophenylenes, which would lie with a planar conformation on top of a metal. [166] This is quite plausible because with increment in length, phenylene-adsorption energies overrule adjacent phenylene-phenylene intermolecular interactions and are expected to prefer a less dense rhombic assembly instead.

6.3 Electronic structure and spatial modulation of QDs on BN

Thanks to their conjugated backbone, QDs can be considered prototype oligo p-phenylene molecular wires. [206, 215, 216] Consequently, many-body electronic effects such as electron−phonon coupling [217, 218] are expected to arise when QDs carry electronic currents. Figure 6.3 depicts a comprehensive portrait of the contrast and tunneling conductance (dI/dV) of the molecular film in response to the bias voltage. Clearly, a spatial modulation of the conductance occurs, closely following changes in the BN platform's "hills" and "valleys", due to local workfunction changes which we have reported recently. [37, 171] In Figure 6.3a, comparative differential conductance spectra of the molecules residing on a Ag(111) metal surface (yellow spectrum) and BN/Cu(111) moiré superstructure (green and blue spectra) are reproduced. All three spectra show prominent features above the substrate's Fermi energy that are assigned to resonances of the molecule's LUMO. Especially, the dI/dV data shows that conductance through molecules on "hills" (representing lower local workfunction areas in green Figure 6.3a,b) and molecules on "valleys" (with higher local workfunction in blue Figure 6.3a,b) differ by almost 0.4 V. It is important to mention that changing the tip−sample distance by ∼1 Å does not significantly affect this on−off voltage difference; hence, modulation of the conductance is not an effect of varying tunneling barrier heights. [219] For the QDs on Ag(111) the LUMO+1 peak (1−0) is clearly visible, exhibiting a maximum with a 0.75 eV separation from the LUMO (0−0) peak (Figure 6.3a).

In the case of the QD monolayer on BN/Cu(111), a typical polyphenylene vibronic signature is recognized, [197, 220] where two peaks (0−0), (0−1), and one shoulder (0−2) are found for the molecules (Figure 6.3a, green spectrum). Such current-induced vibronic progressions [221] are associated with transient molecular charging during sequential electron tunneling. [183, 189, 219] The vibronic intensities can be reproduced to a first approximation with help of the adiabatic overlap of the phonon wave functions in the neutral and charged states (i.e., Franck−Condon factors), in analogy to optical spectroscopy, where the overlap between neutral and excited states is considered. [222] However, unlike optical spectroscopy, the spatially resolved vibronic intensities in tunneling spectroscopy can be further modulated by the tipstate, [189] the tip-molecule distance [219] and potentially by polaronic coupling [186, 187] (see Figure 6.4). Thus, optical spectroscopy can help understanding

the vibronic peak spacing, whereas a simplified model in conjunction with topological considerations will be employed to understand the origin of the (0−0) peak.
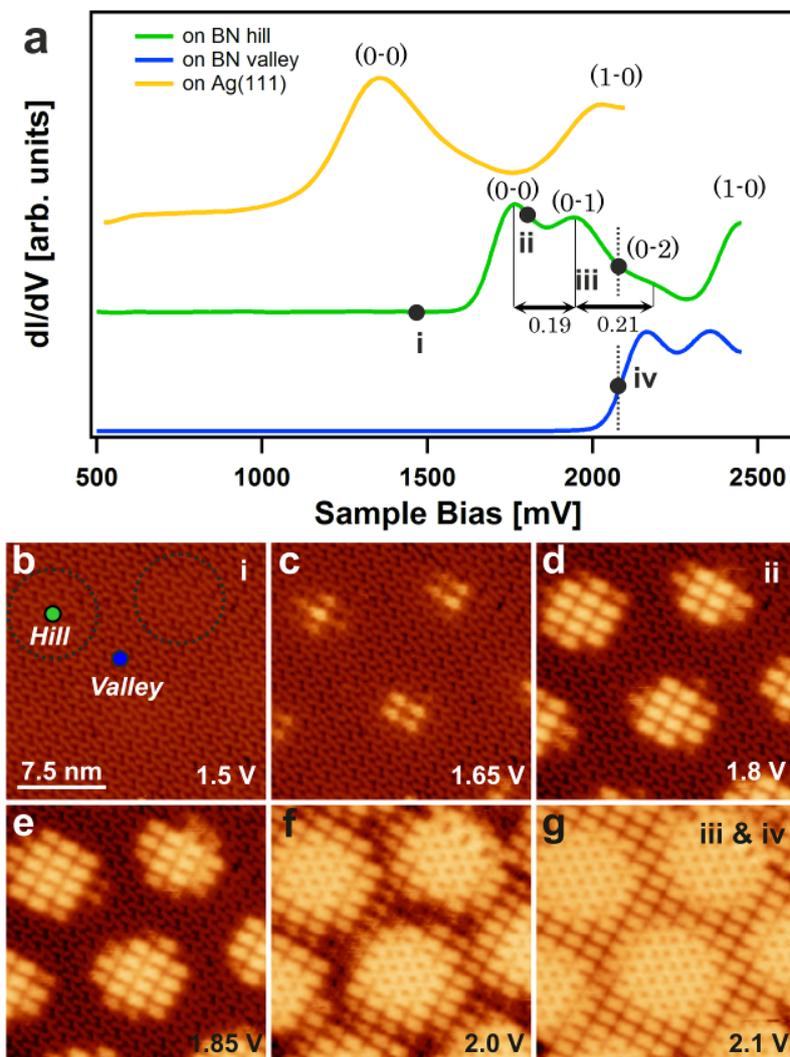
Figure 6.3: Spatial modulation of conductance in a 2D molecular assembly. (a) Comparison of differential conductance spectra of the molecules on Ag(111) (yellow), on the BN "hill" (green) and BN "valley" (blue), in (b). The LUMO of the QDs on BN shows three vibronic peaks (0−0), (0−1), and (0−2). (b)−(e) Image sequence of the molecular film evidencing a gradual outward spreading of bright, brick-like features (V_b = 1.5 to 1.85 V, I = 300 pA). (f)−(g) Net-like features appear for the QDs on BN "hills" while the molecules on the "valleys" appear brick-like (V_b = 1.5 to 1.85 V, I = 300 pA). The STM images for energy values denoted by roman numerals i−iv (black dots) in (a) are represented in (b), (d), and (g).

For flexible and librating oligophenylenes, which provoke non-adiabatic effects of special importance in the progressions, [223] vibronic peak spacing in room-temperature optical spectroscopy allows a qualitative interpretation of the observed low-temperature vibronic tunneling spectroscopic features. For instance, solution optical spectra of QD negatively charged radicals, reveal separations between the $(0-0)$, $(0-1)$, peaks of ~ 0.22 eV (shoulder at 19 800 and peak at 18 000 cm^{-1}, respectively, in ref. [216]). This value is in agreement with the conductance spectra in Figure 6.3a, showing differences of 0.19 ± 0.02 between $(0-0)$, $(0-1)$, and 0.21 ± 0.02 V between $(0-1)$, $(0-2)$. For the higher electronic levels, the $(1-0)$ LUMO+1 and $(0-0)$ LUMO energy difference maintain a close relation (~ 0.7 V) to the difference on Ag(111) (Figure 6.3a, green spectrum). This difference is also in agreement with the TD-DFT (LUMO)$-$(LUMO+1) gap of 0.6 eV (flat conformer, Figure 6.5). The $(0-0)$ LUMO molecular resonances on the metal (peak at 1.4 V) are substantially shifted to lower energies (0.3 V difference) as compared to the resonances on the BN-spacer-layer (1.7 V, green).

This can be explained by a reduction of the on-site Hubbard energy due to screening and charge redistribution upon contact of the molecules with the metal surface. [168] Metal screening causes the electronic gap between the two frontier orbitals (HOMO$-$LUMO) to reduce. Note that the HOMO level in our experiment could not be observed at negative biases, up to a minimum of -2.0 V. Considering the LUMO onset energy of 1.6 V, this might indicate that the electronic gap of the molecules exceeds 3.6 eV, a value close to the gap of 3.2 eV calculated using the Firefly [224] package TD-DFT PBE0 [225] (for an IPT of 35° see Figure 6.5) with a mean absolute error of 0.3 eV. [226] In BN/Cu(111), the "hill" spectrum (green, $(0-0)$ at 1.7 V) is shifted considerably to lower energies as compared to "valley" spectrum (blue, $(0-0)$ at 2.2 V).
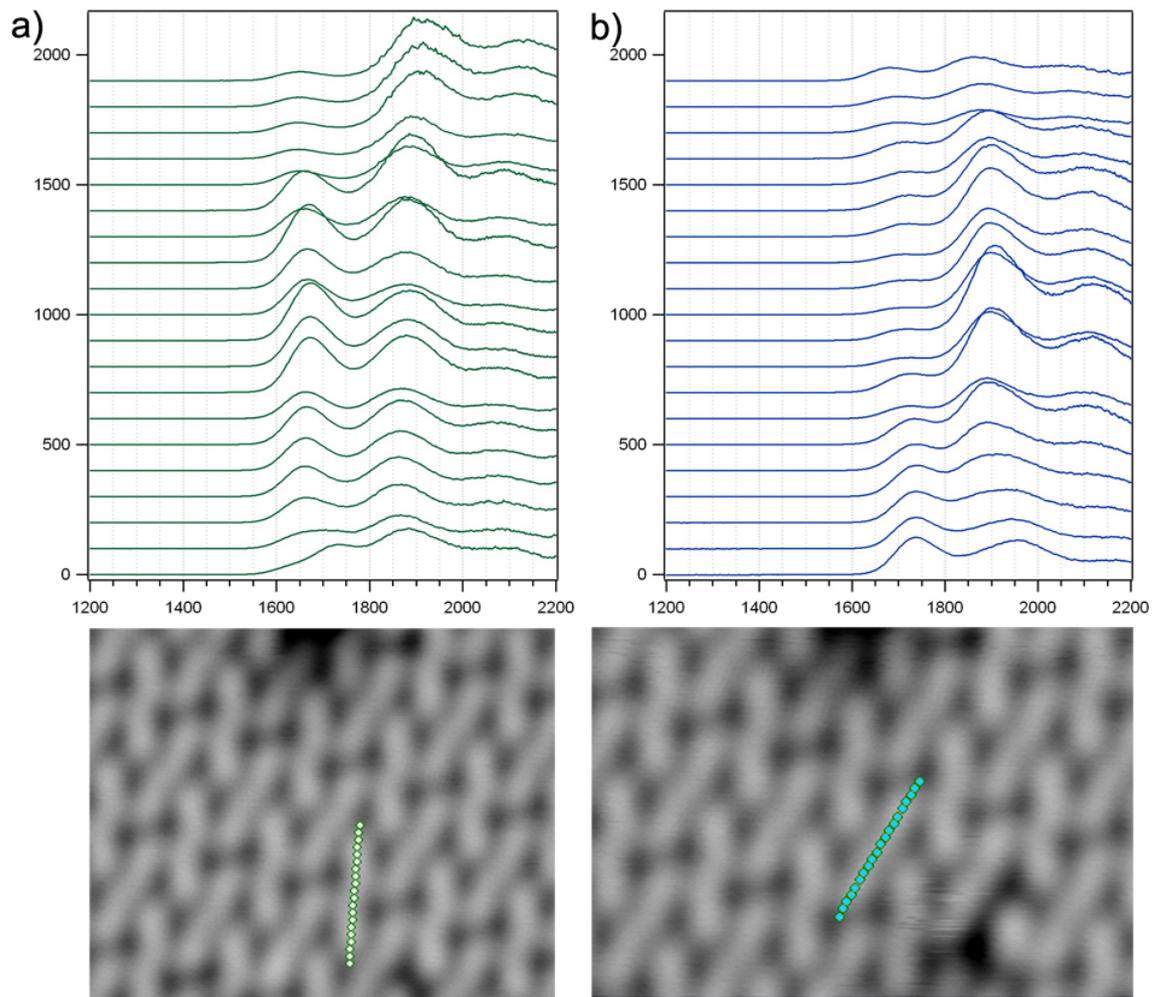
Figure 6.4: *dI/dV* spectra showing the modulation of the vibronic spectra in a single molecule. a) Along the zigzag molecule b) along the straight molecule.
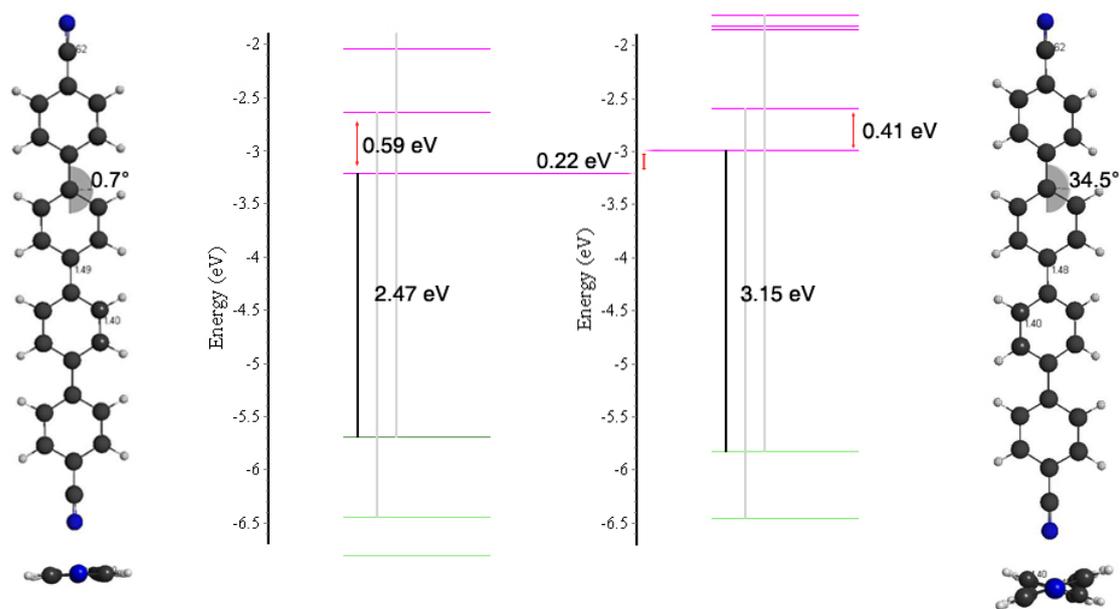
Figure 6.5: TD-DFT gas phase energy level alignment. A straight (left) and a zigzag (right) molecule is show. [210]
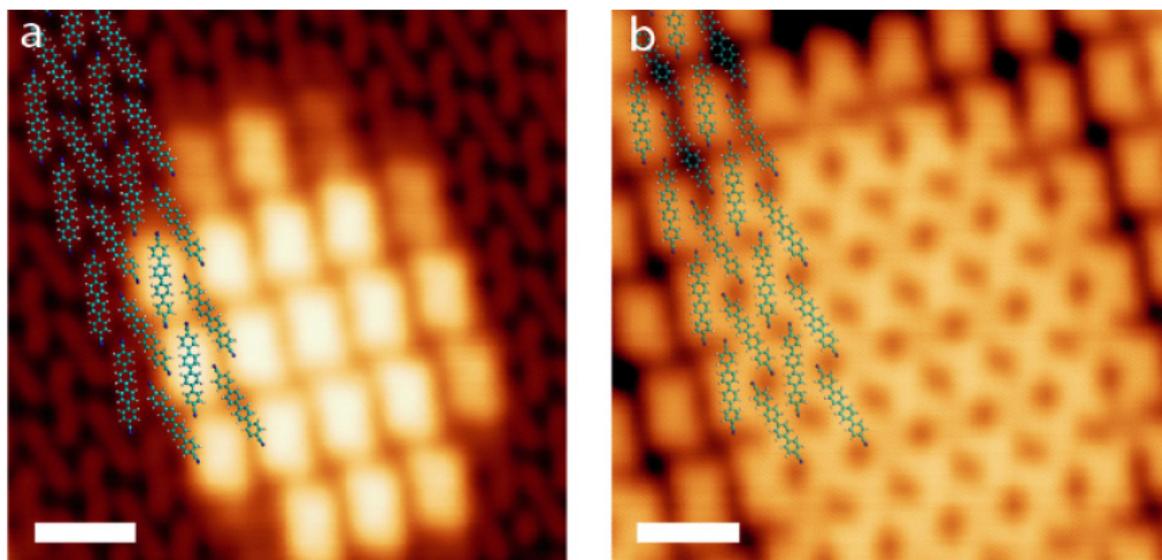
Figure 6.6: Higher resolution images with molecular models. a) Brick-like structure. $V_b = 1.86$ V, I = 100 pA. b) Net-like structure. $V_b = 2.06$ V, I = 100 pA. Scale bar is 2 nm.

We have previously reported [37] that the local workfunction is modulated in BN on Cu(111). As a result, the region of lower local workfunction represented by an electronic moiré "hill" is the first to reveal the architecture's $(0-0)$ LUMO feature. Figure 6.3b−g depict the STM topography at selected points in the dI/dV spectra. It shows the emergence and gradual expansion of bright features in the range of 1.65 to 2.1 V. The black dots (c.f. labels "i", "ii", "iii", and "iv") mark the bias used for STM data in Figure 6.3b, d, and g. The point "i" at 1.5 V lies in the gap for molecules on both "hills" and "valleys"; therefore, the corresponding image (Figure 6.3b) shows the homogeneous topography of the QD film. Similarly, point "ii" represents 1.8 V at which we observe the $(0-0)$ peak for the "hill" spectrum only; and still the energy gap molecular contrast for the "valley" spectrum. This corresponds to the situation shown in Figure 6.3d which exhibits the $(0-0)$ peak for the molecules residing over moiré "hills". Until this point the $(0-0)$ peak evolves into an array of brick-like structures and the molecules at the "valleys" are unperturbed. With increasing bias until 2.1 V, we observe the spreading of the brick-like structure also for the molecules on the "valleys". At the same time, for an applied bias above 2.0 V, a second net-like porous structure (Figure 6.6) appears in the STM topography on the projected moiré"hills" region, at the energy of the $(0-1)$ peak, together with the $(0-0)$ brick-like features for molecules at the "valleys". This is represented together as points "iii" and "iv" on "hill" and "valley" spectra, respectively.

6.4 Second intramolecular modulation

A striking outcome of the electronic decoupling of QDs from the substrate is the observation of a second level with spatial conductance modulation related to the vibronic excitations. High spatial and energy resolution is used to unravel the origin of the observed brick-like topography features. Figure 6.7 depicts close-ups of the STM topography at voltages in the $(0-0)$ vibronic peak range, of 1.70 (A), 1.73 (B), 1.75 (C), and 1.80 V (D), respectively. Each brick-like feature is clearly shown to fit to the assembly's unit cell (red rectangles), which encompasses the area of two molecules. The center-most position of the brick-like feature is due entirely to one single molecule whereas the lower part appears to be composed of two excited zigzag molecular ends strongly interacting together. It is worth mentioning that equal vibronic signatures for every molecule in the assembly are recovered in the net-like structure at energies in the $(0-1)$ vibronic peak range (Figure 6.6).
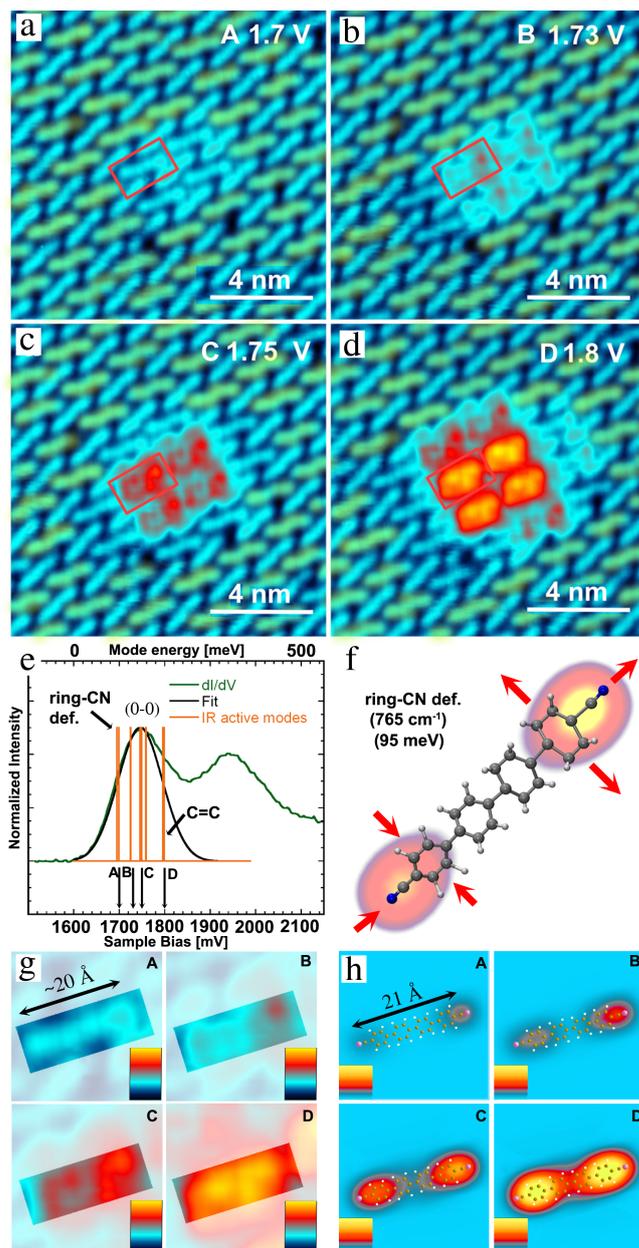
Figure 6.7: Modulation of vibronic conductance at the single-molecule level. (a)−(d) STM images showing straightening of the molecules belonging to the zigzag molecular rows (in yellow) a top of the moiré "hill" as a function of bias (V_b = A, 1.7 V; B, 1.73 V; C, 1.75 V; D, 1.8 V; I = 100 pA). (e) Differential conductance spectrum. Vertical lines represent normalized, nonzero normal-mode gas phase vibrational (i.e., IR) modes from 1400 to 200 cm^{-1} (orange). These modes are weighted with Gaussians to fit the experimental spectrum envelope. (f) Normal mode approximation benzonitrile deformation at 765 cm^{-1} (95 eV) and its underlying real-space vibronic mapping. (g) Detail of a single-molecule vibronic excitations during increasing energy in (a−d). (h) Modeled energy-accumulated vibronic maps up to energies of A, 806 cm^{-1}; B, 1008 cm^{-1}; C, 1209 cm^{-1}; and D, 1612 cm^{-1}. [210]

Interestingly, the center-most molecule appears straight at 1.70 V bias. A detailed inspection reveals (Figure 6.7a–d and Figure 6.8) that the row that includes the center-most molecule consists exclusively of zigzag molecules (zigzag rows colored in yellow). The fact that at 1.70 V the molecule near the "hill" appears straight is assigned to a current-induced librational excitation, [197] causing molecules to oscillate between high and low IPT angles. This points that the electrons injected by the STM-tip effectively couple to molecular vibrations [157, 189, 190, 227] and rotations. [191, 192, 228] Accordingly, the STM topography reflects current-induced vibronic excitations. Thus, localized excitations can be tentatively assigned to discrete, sub-molecular vibrational/librational modes when examining the topography of a single center-most molecule belonging to the brick-like topography feature.

At 1.70 V, corresponding to energy A in the *dI/dV* spectrum in Figure 6.7e, one end of the molecule appears brighter than the rest of the molecule. The center of mass of this excitation is shifted upward and a higher conductance and brighter topography contrast is detected upon increasing to energy B. At the same time, the opposite end of the molecule becomes wider. At energies exceeding 1.75 V (C and D in Figure 6.7c, d) the vibronic excitations appear to couple to the lattice and a single-molecule signature is hard to recognize as independent from the adjacent molecules. On the one hand, vibrationally coupled vibronic excitations are known to occur in the form of Frenkel polarons. [188] On the other, vibronically coupled excited molecules can stem from formation of excimers [229] and other inter-molecular charge and energy transfer effects.
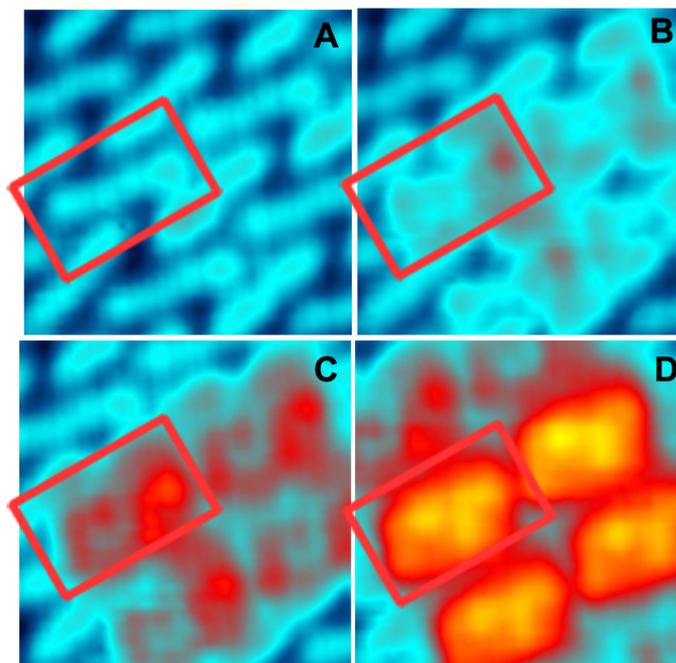
Figure 6.8: High resolution STM topography in Figure 6.7. At the "hill" of the
BN molecular film, a transition from zigzag to straight molecules (and vice versa)
is observed with increasing tunneling bias (V_b = A.1.7 V, B.1.73 V, C.1.75 V and
D.1.8 V_b, I = 100 pA), attributed to excitation of librational modes.

Despite evidence for vibronic excitations being strongly anharmonic, the normal-
mode approximation (NMA) can be used to compute the gas phase vibrational
spectrum in order to shed light into the possible origin of localized current-induced
vibronic excitations observed between 1.70 and 1.75 V (A and B in Figure 6.7c,d).
To this end, the dipole-weighted infrared (IR) gas phase vibrational spectrum of the
QD radical anion zigzag state was computed at the DFT PBE0 [225] level of the-
ory. Such dipole selected (IR) intensities have been found to describe well vibronic
assisted tunneling spectra in highly flexible molecules. [230] It is worth mentioning
that such an approximation to electron−phonon coupling is reasonable since rela-
tive electron−phonon modes and weights must also be assumed for complex spectra
[231, 232] and because of computational challenges, as elaborated below. The first
intense peak from the IR gas phase spectrum (95 meV or 765 cm^{-1} vibrational en-
ergy) corresponds to an asymmetric benzonitrile (ring-CN) deformation or breathing
(Figure 6.9). Considering the energy, intensity, and geometry of such modes, the
aforementioned increase in the STM contrast at the end of the molecule (A and B
in Figure 6.7g) can be tentatively assigned to this asymmetric benzonitrile deforma-

tion. To get further insight, we fit the IR spectrum to the experimental conductance (dI/dV) spectrum and use it to weight the infrared intensity in real-space per atom (a vibronic map). For the fitting, every IR mode with nonzero intensity is normalized to one, as an approximation of (closely spaced) Franck−Condon active modes. Subsequently, each IR mode is weighted with Gaussians ($\sigma = 300$ cm^{-1}) to reproduce the envelope of the dI/dV (0−0) peak. Effectively, this oversimplified adiabatic picture assumes a sum of progressions, with $\sigma = 300$ cm^{-1} the librational broadening accompanying each active mode. Such a simple model is employed since computing the electron−phonon interactions [182] underlying the full vibronic conductance [233] is a serious theoretical challenge, particularly for cases with multi-mode strong coupling. [233, 234]
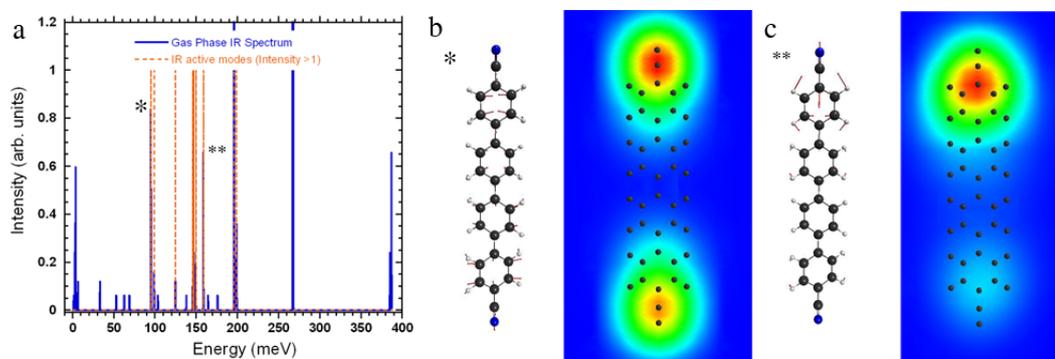
Figure 6.9: DFT as-computed and scaled Infrared gas phase spectrum. a) Comparison between the computed DFT Infrared gas spectrum (blue lines) and the nonzero >50 meV IR active modes (in orange, convoluted to the dI/dV (0-0) peak in the main text). b) The benzonitrile breathing mode at 95 meV (765 cm^{-1}) and individual IR intensity mapping. c) The benzonitrile rocking at 145 meV (1177 cm^{-1}) and its individual IR intensity mapping. [210]

Figure 6.7e shows the position of the nonzero IR modes with orange lines. For the vibronic mapping, the sum of squares of the dot product between the dipole tensor and the respective NMA vector is mapped at the atom's coordinates and color coded. Figure 6.7f shows the ring-CN deformation NMA of the QD with its respective vibronic mapping. The rendered map displays intensity asymmetries proper of a nonzero transition dipole matrix (see also the mapping for individual benzene modes in Figure 6.10). Therefore, it is clear that the dipole-selected vibrational contributions explain the real-space molecular vibronic symmetry during current-induced excitations, showing maximum amplitudes at the benzonitrile moieties.
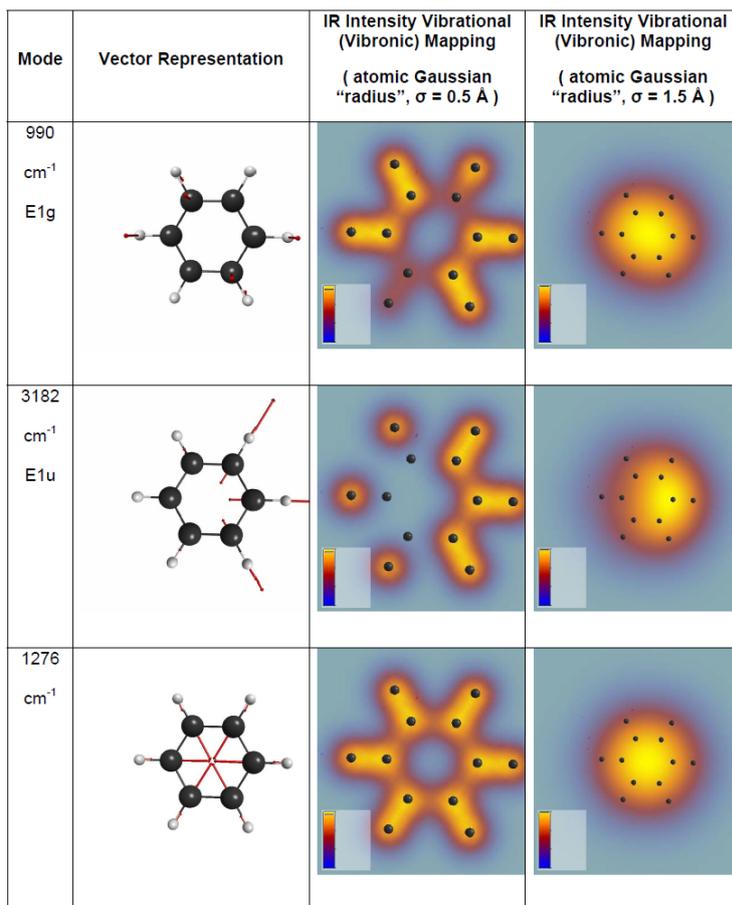
Figure 6.10: Benchmark for IR intensity mapping of individual modes. With our mapping method of the IR intensity per atom, strongly asymmetric modes like the benzene ~990 cm^{-1} E1g and ~ 3182 cm^{-1} E1u are recognized with ease. All other symmetric modes, where movement of all atoms are involved, like for the ~1276 cm^{-1} mode A1g, are featureless with our mapping method. The lower resolution (σ = 1.5 Å) used for the rendering of the maps in the main text Figure 6.7 is also shown. The IR intensities shown here were calculated at the AM1 level of theory. Complete scripts for quantum chemical calculations, individual script mapping and cumulative summing are provided in the online supplemental material. [210]

In order to compare the experimental STM images to the vibronic maps, the modeling results for each mode are Gaussian weighted and cumulatively summed to the corresponding energies in Figure 6.7e. We find that the computed energy accumulated vibronic maps in Figure 6.7h parts A and B, correlate with the corresponding experiment in Figure 6.7g parts A and B. Energy A in both Figure 6.7g,h shows a fair increase in the intensity of the vibrational excitation at the molecules' benzonitriles. At energy B in Figure 6.7h, this vibration is stronger at one side of the

benzonitrile, in agreement with Figure 6.7g. At the same time, the opposite end also shows a broad signal. At even higher energies (C in Figure 6.7g), strongly convoluted excitations are observed throughout the molecule. The higher amplitude of the topographical excitations on one benzonitrile's end at these higher energies can be assigned to the contribution of a non-degenerate asymmetric vibrational mode, the benzonitrile rocking at 145 meV or 1177 cm $^{-1}$ (see Figure 6.9). Finally, at energy D in Figure 6.7g these excitations move in amplitude toward the molecule's center. This is marginally reproduced by the vibronic maps, but in agreement with the benzene double bond stretching modes being excited at this higher energy ($\sim$200 meV or 1600 cm^{-1}). Thus, our simplified model attributes the conductance shape of the (0$-$0) peak to a pronounced mixing of fine-spaced ring torsions and stretches, as reported in optical spectroscopy experiments. [197, 198, 220, 222]

One notable observation is the conservation of crystalline order during current-induced asymmetric excitations. In other words, excitations where one end of the molecule appears brighter are found on the entire monolayer, and the pattern acquires an additional level of chirality in the excited state. Related phenomena have been previously observed in electronic states [235] and may be an intrinsic effect of the monolayer lattice phonons; influenced by the underlying substrate and dynamic electrostatic (dipole) forces. These observations in a model conjugated oligomer give remarkable insights on how charge transport occurs in polyphenylenes along the vertical direction, en route toward a quantitative understanding of polarons in bulk molecular wire solids.
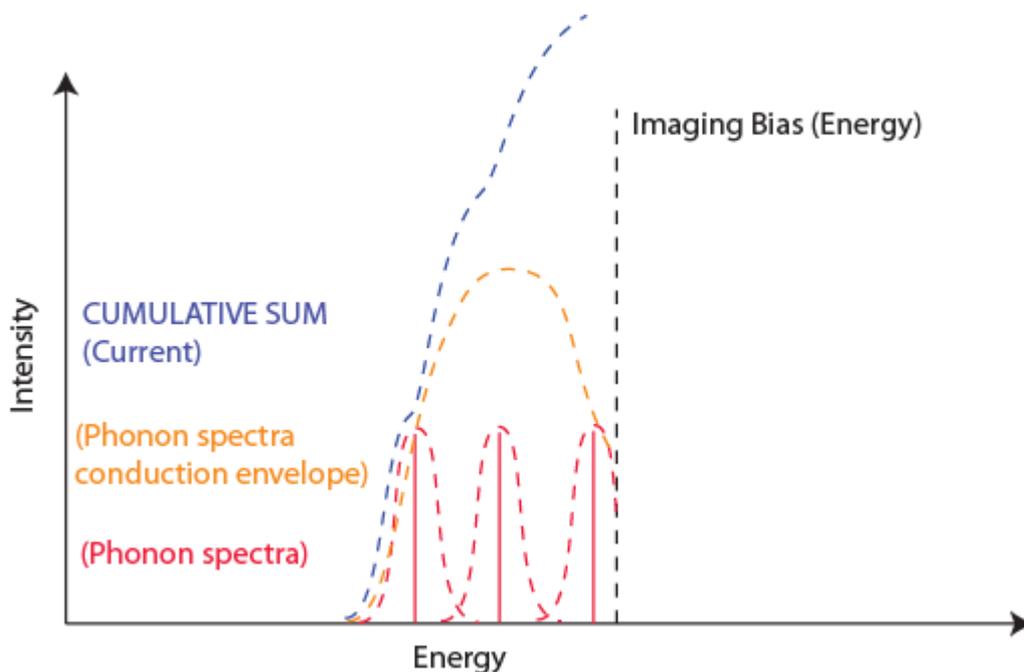
Figure 6.11: Schematics for the calculation of "vibronic" maps in the vibronic assisted conductance (tunneling) picture.Schematics for the calculation of "vibronic" maps in the vibronic assisted conductance (tunneling) picture. Every IR mode with non-zero intensity is normalized to one, as an approximation of (closely spaced) Franck-Condon active modes (red solid line) between the neutral and charge species which are at the origin of electron-vibron coupling in the sequential tunneling regime. [219] Subsequently, each IR mode is weighted with Gaussians ($\sigma = 300$ cm^{-1}, red dotted line) to reproduce the envelope of the dI/dV (0-0) peak (yellow line) which is then cumulatively summed (blue) to the imaging energy in order to reproduce the "vibronic" map at the respective biases. [210]

6.5 Experimental procedures and theoretical methods

The BN surface was prepared by chemical vapor deposition (CVD) of borazine; following a protocol described in previous chapters and ref. [37]. The QD molecules were deposited using organic molecular beam epitaxy (OMBE) with the quartz container held at 503 K while the BN/Cu(111) substrate was kept at 293 K. All STM data were recorded in constant current mode and the dI/dV spectra were taken using a lock-in amplifier (f = 969 Hz, ΔVrms = 18 mV). The STM images shown in this work are processed using the WSxM software. [120]

For molecular dynamics a full 200 nm x 100 nm monolayer molecular crystal containing 270 QD using periodic boundary conditions was prepared. The experimental unit-cell in the monolayers was rounded to the theoretically allowed super cell for BN, a = 14.11 Å, b = 20.50 Å (a,b) = 90°, considering a fixed BN unit cell of a,b = 2.54 Å, (a,b) = 120°. The QD monolayer with underlying BN substrate was investigated by molecular dynamics (MD) using the MMFF parameter [236] implementation in the program CHARMM c36. [237] The vdW parameters were approximated by graphene Lennard-Jones parameters [213] which closely follow BN adsorption energies. [214] The Langevin Thermostat was used to perform constant temperature MD and to quench the monolayers from 300 K to 10 K, close to the experimental imaging temperature. SHAKE [238] algorithm was used to constrain the hydrogen atoms and 2 fs integration time steps were used.

The structures were minimized at the density functional theory level using a 6-311G basis set with the PBE0 [225] functional to a RMS Energy gradient below 0.00001 Hartree. The Hessian and dipole derivative tensor were obtained from DFT and used to calculate the IR intensities. DFT and TD-DFT calculations were performed with the quantum chemistry package Firefly [224] based on the GAMESS (US) [239] source code. For the TD-DFT the transitions between the first 10 excited states were computed. All the DFT calculations shown here are based in a stationary state of a negatively charged QD saddle point with IPT angles of 36°, 38° and 36° and imaginary frequencies of 67 cm^{-1} , 58 cm^{-1} and 51 cm^{-1}. For the fitting of the IR phonon intensities to the dI/dV signal, the sum of squares of the dot products between the dipole derivative tensors and the normal-modes was computed, the intensities higher than 1 were normalized and fitted to the experimental (0-0) peak by convoluting each peak with Gaussian envelopes of $\sigma = 300$ cm^{-1}. To render the vibronic maps in Figure 6.7, the IR intensity per atom was calculated by means of the sum of the squares of the dot products between the dipole derivative tensors and its Cartesian component at each atom. Then, these normalized "IR" intensities per atom are fitted to Gaussian envelopes of $\sigma = 3\,300$ cm^{-1} and cumulatively added (see Figure 6.11) to the respective energies (A. 806 cm^{-1} B. 1008 cm^{-1} C. 1209 cm^{-1} and D. 1612 cm^{-1} in Figure 6.7) and the isosurface was mapped. Figure 6.10 illustrates how individual IR modes are represented by such mapping in a benchmark model. For benzene the root square, rather than the square of the dot products was used for clarity in the mapping. All scripts used are provided in the supporting online information as an additional zip file, in accordance with rcecer.org.

6.6 Conclusion

In conclusion, intramolecular current-induced vibronic excitations can be spatially modulated in a substituted oligophenylene monolayer atop a BN/Cu(111) template. We showed that intrinsically electronic corrugated platforms can shift molecular energy levels by up to 0.4 V. STM studies in conjunction with MD calculations revealed how quaterphenylene dicarbonitriles transfer and amplify their axial chirality coherently across a crystalline monolayer. Librational (inter-phenylene torsion) modes are strongly excited during vibronic conduction. Higher energy vibronic excitations are assigned to calculated dipole-selected vibrational excitations thanks to spatially resolved vibronic maps. In conjunction with preferential conductance at specific sites, these results might inspire a new generation of self-assembled, spontaneous electronically patterned, molecular electronics device elements.

7 Formation, Characterization and Functionalization of Cobalt Coordinated Structure of Oligophenylenes on Boron Nitride

Compared to weak hydrogen / van der Waals or sophisticated covalent bonded nanostructures, metal directed systems offer stability, order and better control to steer desired architectures and properties of matter at the nanoscale. Also important is the establishment of fundamental properties and exploration potential functionality of such systems. Presented here is a detailed report of a low temperature scanning tunneling microscopy/spectroscopy (STM/S) and complementary density functional theory study of cobalt-coordinated structure of conjugated oligophenylene linker molecule on an inert boron nitride spacer-layer. The metal-coordination confirms a previously predicted four fold square motif with two distinct inter-switchable conformations of the molecule on BN; making it a model system for such current induced functionalization. Furthermore, a comparative STS/DFT study of potential barrier variation across the metal-ligand profile on two different substrates (BN and Ag(111)) reveals a reverse charge distribution as compared to each other, revealing the intrinsic chemistry of such systems and the role of substrates thereof.

7.1 Introduction

With innumerous studies of self-assembled organic molecular systems, the understanding of surface supported supramolecular chemistry has grown tremendously. With every step forward in the comprehension of the self-assembly protocols, we come closer to create novel nanostructures for future artificial devices. So far, both non-covalent (van der Waals forces, hydrogen bonding and metal-coordination) [7, 8, 240] as well as covalent [19, 241, 242] inter-molecular interactions have been employed for self-assembly of molecules on surfaces. In particular, metal directed nanostructures have gained great attention due to their optimum properties like stability and long-range order over large domains. The weaker (van der Waals, hydrogen bonds) or stronger (covalent) assemblies often lack one or more of the above mentioned features. One-dimensional (1D) chains [13, 243] and numerous impressive arrays of two-dimensional (2D) nanostructures, [7, 8, 12, 14, 240, 244–246] based on various metal-organic assemblies have been reported; yielding diverse architectures. However, to reach the goals of truly applicable devices, organometallic networks with controlled structure, properties and above all functionality are needed. Therefore, a systematic study to understand and exquisitely control the metal-coordinated networks' fabrication and functionality is highly desirable.

As a model systematic study, a series of scanning tunneling microscopy studies of networks based on n-phenylene dicarbonitrile and their metal-coordination with various metal atom centers have been reported. These are simple linear ditopic linker molecules (see inset, Figure 7.1b) with extendable phenylene backbone terminated by carbonitrile moieties (NC-Phn-CN; n = 3,4,5,6) The experiments were designed to control aspects such as size, assembly, structure of the networks. First on a Ag(111) surface, upon coordination with cobalt (Co) metal atoms, linear molecules with CN moieties at terminal para-positions yielded a highly ordered porous honeycomb nanomesh based on three-fold coordination at the metal center (see Figure 7.1a for nanomesh, NC-Ph4-CN). Notably, the cavity sizes of the structures were tunable by changing the number of phenylenes (3 to 6). [15–17] Next, by simply changing the position of the carbonitrile groups in the molecules to meta-positions, a new assembly of random 2D string network was recorded. [247] This was a consequence of change in the position of the terminal groups and prochirality (due to rotatability of phenylene rings) of the molecules. To control the network structure of the metal organic framework, an alternative solution is to switch the coordinating metal center

in the assembly. Lately, instead of cobalt atom centers we applied cerium and gadolinium metal atoms of lanthanide elements. Due to larger sizes of the atoms and higher number unsaturated electrons, cerium and gadolinium enable higher number of coordination possibilities to the molecules. As a result, we were able to demonstrate a special five-vertex Archimedean surface tessellation. [18, 248] Finally as a leap further, in this work we substitute the underlying metal substrate to study cobalt-coordination of the linear four phenylene linker on monolayers of insulating boron nitride on Cu(111). This gives the possibility to study metal-coordination on a decoupled environment where the probed system is unperturbed from the strongly interacting metal support.

7.2 The substrate and the molecule

A range of spacer-layers that reduce adsorbate-metal substrate interaction like alkaline halides [21, 178, 179], oxides [132, 180], graphene [24, 30, 111, 112, 135, 138] and recently boron nitride [171, 210, 232, 249, 250] have been reported. However, most of these epitaxially grown ultrathin layers have inherent drawbacks like strong polarity, non-planarity (corrugation) and inhomogeneity, thereby making it unsuitable for nanostructures based on metal-coordination. Moreover, 2D metal-coordination studies on decoupling insulating layers are simply rare. [171, 251] Recently, we reported a rather interesting insulating monolayer of BN grown epitaxially on Cu(111). It was demonstrated that on Cu(111) the special breed of sp^2 hybridized hexagonal ultrathin layer is topographically planar but has a continuous spatial workfunction modulation. [37] Nonetheless, as an insulating flat layer, it is an ideal platform for studying metal directed nanostructures on it.

Quaterphenylene dicarbonitrile (QD) is a ditopic linear molecule with four conjugated phenylene rings terminated by carbonitrile moieties at the para positions (NC-Ph4-CN; see inset, Figure 7.1b). Linear polyphenylene molecules have interesting optical and electronic properties with potential applications in organic thin film transistors, light emitting diodes etc. [206] The CN groups of QD makes it possible to use the molecule as organic ligand, which can be coordinated to metal atoms to create nanoporous networks. [16, 17] The QDs were previously studied on Ag(111) surface under monolayer coverages where the underlying metal substrate played a significant role in the reported planar conformation, [166, 206] along with

an extended honeycomb lattice through cobalt -coordination. Upon deposition of QD on the decoupling BN/Cu(111) surface the molecule exhibits a zigzag feature due to alternating rotation of the phenylenes. [210] Therefore, it is a promising endeavor to form, characterize and explore functionality of the metal-coordination of QDs on the insulating BN/Cu(111) support.

In this chapter, we present a low-temperature scanning tunneling microscopy, spectroscopy, and additional density functional theory study of cobalt-coordination of QD linker molecules on BN/Cu(111) which exhibits a four-fold binding motif at the metal center; supporting earlier predictions from DFT calculations. Additionally, we observe bi-stable switchable states of the Co bonded molecules due to non planar conformations from phenylene rotations on the insulating layer. Importantly, supported by a basic DFT study we report a distinct (opposite) potential barrier variation across the metal-ligand profile on the spacer-layer as compared to on traditional metal substrate hinting; to an opposite charge distribution of such system on an insulator. This opens up a completely new avenue for research and characterization of metal organic networks and their unexplored functionalization on novel surfaces like BN.

7.3 Metal-coordination of QD

To form metal-coordinated frameworks, cobalt was deposited on submonolayer coverages of QDs on BN/Cu(111). The process yields a structure consisting of four-fold coordination motif with a tendency for a square lattice as seen in Figure 7.1b. This is interesting as the same molecule forms a well characterized three-fold motif honeycomb lattice on traditional metal surfaces like Ag(111) and Cu(111) *(vide supra)*. Such a case is illustrated by the overlapped model in the inset of Figure 7.1a, where a Co atom coordinates three QD molecules, with two molecules spanning an angle of 120°. On the insulting spacer-layer however, a four-fold bonding motif is observed. This corroborates earlier DFT calculations [16] that predicted four-fold coordination to be energetically favored over three-folded one, in the absence of a metal support. This is a clear indication that BN indeed acts as an insulating support for the metal-organic network.
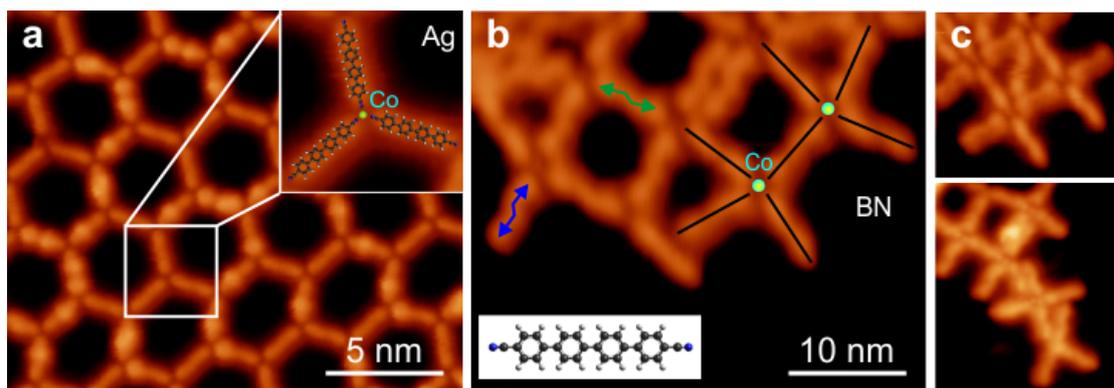
Figure 7.1: Co-coordination of QDs on surfaces. (a) Three-fold coordination motif of QDs on Ag(111) (V_b = 0.5 V, I = 100 pA). Detailed zoom of a bonding motif in the inset with superimposed model. (b) Four-fold coordination motif of QD-Co on BN/Cu(111) (V_b = 0.3 V, I = 80 pA). Two distinct zigzag features of the QDs observed shown with blue "s" and green "z" like lines. Model of QD with four phenylene rings terminated by carbonitrile moieties in the inset. (c) Smaller patches of four-fold QD-Co frameworks on BN (V_b = 0.3 V, I = 0.27 pA) with an individual QD trapped in the square cavity of the top figure.

The sample was found to be replete with small patches of the four-fold QD-Co metal organic framework as seen above in Figure 7.1b and c. However, extended networks could not be found as the cobalt atoms clearly prefer cluster formation on BN instead. Also the electronic modulation [37] of the BN surface had no significant templating effect [171] on QD molecules; metal-coordinated or not. [210]

Further in Figure 1b, the metal-coordinated QDs appear zigzag on BN/Cu(111) as compared to flat on metal surfaces. [16, 17] Such feature of the QDs on BN was also reported in our previous work where uncoordinated non-planar molecules form dense packed chevron assembly. [210] Due to absence of the meddling metal surface, QD is stabilized on the insulating BN platform with alternating torsional angles of the phenylene rings in the molecular backbone. It is however interesting to note that the molecules exhibit non planarity after Co-coordination as well. It can be easily explained as an effect of decoupling of the QDs from metal surface with which the phenylenes normally have a laterally attractive π conjugation. On an insulating BN support phenylene rings undergo the alternating rotation due to steric hindrance to each other. Such phenomenon was also reported in previous works comprising of similar molecules atop a decoupling monolayer. [206] Regardless of metal-coordination whether on one end (see Figure 7.1b, blue "s" lines) or both ends (green "z" lines) the molecules exhibit the zigzag conformation.

7.4 Model functionalization of a robust metal-organic structure on an insulator

The robustness of the metal-ligand framework was tested by performing vertical manipulation on a QD-Co arm with one end of the molecule free as shown in Figure 7.2a. In this process the STM tip was placed on top of Co atom junction (green sphere) for 10 seconds under a bias voltage of 1.2 V. As seen in the top and down sequence images of Figure 7.2a, the metal organic bond was found to be stable with the molecular arm strongly attached to the metal center. However, as seen in the figure the QD appears to alter its conformations during the process from previously described non planar green "z" to blue "s" state. These are the same two distinct conformations discussed in Figure 7.1b (vide supra) with alternating phenylene rings on its molecular backbone. Upon repetition of the process the arm traverses up and down forming almost 30° angle between the two states. Obviously, the alternating non planar phenylene rings flip between the two states due to possible charging and vibrations/librations as reported in our recent publication. [210] Moreover, the inert BN surface facilitates such flipping of the phenylene rings as there is significantly weaker π interaction on the spacer-layer.

Furthermore, the metal-organic framework was explored for potential functionalization as model conductance switch system. On a similar insulating surface pioneering work demonstrating conductance switch using naphthalocyanine [21] and later free-base porphyrins on Ag(111) [150] using tautomerization has been performed. On the insulating BN surface, we utilized a QD bonded to Co atoms with both nitrile groups to demonstrate a bistable conduction switch (see Figures 7.2 b&c). Unlike the molecule with one end free, the double bonded QD provides stable measurement conditions. Applying tunneling current on top of the molecular backbone above a threshold voltage 1.2 V, the QD undergoes reversible switching between green "s" and blue "z" conformational states.

In order to visualize the switching process better we recorded the tunneling current I versus time t by placing the STM tip above and slightly off the molecular center (black dot, Figure 7.2b) while keeping the feedback loop open. As a result we get a typical telegraphic curve $I(t)$ depicting switching between the two distinct "z" and "s" states shown by two defined current levels Q_1 and Q_2 (Figure 7.2d). After careful examination of the switching curve and the images preceding/succeeding the

measurement, we assign the higher conductance level Q_1 and lower Q_2 to "z" and "s" conformations respectively. The reason behind higher conductance level Q_1 is the proximity of phenylene ring at the off center position of the STM tip for "z" and vice versa. Importantly, we did not find any clear preference for the QD to stabilize at either of the two conductance states or conformational states.
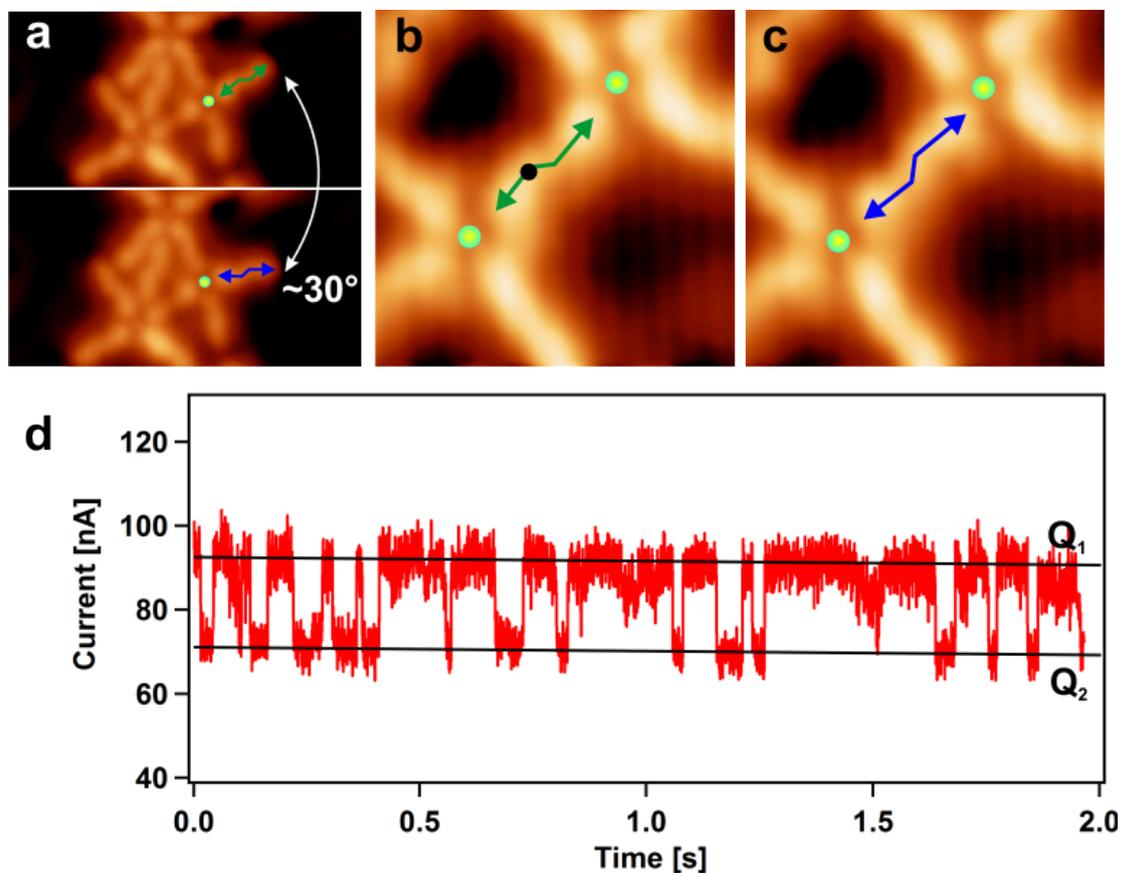
Figure 7.2: Functionalization of the QD-Co framework. (a) Flipping of QD arm free at one end upon tunneling of electrons on the metal center (V_b = 0.5 V, I = 27 pA). The molecule flips up and down forming a 30° angle and switching between the two "s" and "z" states. (b &c) High resolution STM images (V_b = 0.3 V, I = 50 pA) of a QD bonded at both ends. Bistable switching observed between the two states as the electron injection was performed at an off-centered position (black dot) on the QD. (d) Telegraphic $I(t)$ curves exhibits the switching process between the two blue "s" and green "z" states with distinct Q_1 & Q_2 levels of conductance.
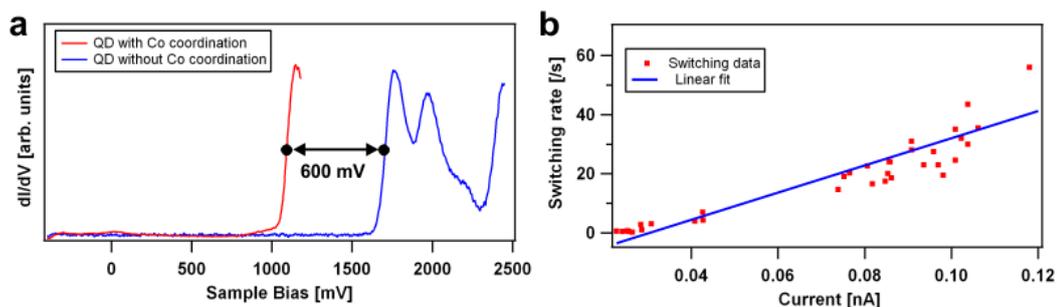
Figure 7.3: STS and switching rates of QDs. (a) Comparison of spectra of Co-coordinated QD and free QD on BN. LUMO of Co-coordinated QD (red) around 1.2 V and free QD (blue) around 1.8 V. The complete feature of the red spectrum beyond LUMO unattainable due to rupture of metal-coordination at higher energies. (b) Current dependence plot of the switching process. Linear fit of the switching rate increment with current signifies a one electron process behind the conductance switching.

As reported for the QDs on BN without metal-coordination, the molecules undergo current induced vibronic progression as the molecules are charged during sequential electron tunneling. [210] Additionally, we used STS to record differential conductance spectra on both Co-coordinated as well as free QDs in assembly wherein we note that the lowest unoccupied molecular orbital (LUMO) energy for a metal-coordinated QD is observed around 1.2 V above Fermi level E_F (see Figure 7.3a). As this is the threshold voltage above which the switching occurs, we can tentatively assign it to transport through the LUMO. In principle the tunneling electrons are likely to shortly fill up the LUMO thereby altering the molecule-sample interaction inducing flipping or rotations of the phenylene rings.

To evaluate the current dependence of the switching process we performed series of measurements at 1.2 V at varying tunneling currents. In all cases the STM tip is placed on a slightly off-centered position on QD as described above. As the molecule flips between the two states and conductance levels Q_1 & Q_2, a switching rate was evaluated from the count of switching event per time for various tunneling currents. As seen in plot of Figure 7.3b, the switching rate agreeably increases linearly with current. This suggests that the flipping of the phenylene rings between the two states is driven by a one electron process. Thus it is clear that our prototypical system functions as a model bistable molecular switch on BN.

7.5 Electronic structure of decoupled model system

As further characterization of the QD-Co metal-ligand system and to probe its potential functionality as molecular wire network, charge transfer as well as injection/extraction needs to be understood. For this, detailed profile of local workfunction across the molecule-metal center was measured, which is determined by apparent barrier height ϕ . The apparent barrier height of the metal-ligand profile was extracted by measuring slope of fitted logarithmic tunneling current I as a function of tip sample distance z . Following the protocol described by Vitali *et al.* [104] a tip independent relative variation of the workfunction $\Delta\phi = 2\left(\phi_{QD} - \phi_{BN}\right)$was calculated and plotted along the measured profile of QD-Co metal organic system on BN as seen in Figure 7.4a,b. Interestingly, the local relative workfunction variation $(\Delta\phi)$ is seen to decrease on the molecular backbone while sharply increasing for the Co metal centers. In contrary, $\Delta\phi$ has the opposite behavior (see Figure 7.4d,e) for the metal-ligand profile on Ag(111) compared to on the spacer-layer.

Generally, the workfunction is a good measure of chemical and physical processes in a metal organic complex like QD-Co and depends on various factors like molecule-substrate interaction, charge transfer & rearrangement, molecular bonding and adsorption geometry etc. In stark contrast, all these parameters are totally different for our two QD-Co frameworks primarily due to the underlying substrates. The framework on BN is decoupled from the underlying electron rich metal surface, which rules out many ordinary processes like charge transfer, formation of induced dipoles etc. Moreover as discussed before, the non planar geometry of the molecular backbone means the weakening of interactions via π conjugation as well. Therefore, the chemical activity occurring in QD-Co on BN system is almost of intrinsic nature and the measured workfunction variation can be arguably assigned to pure charge rearrangement between the only two actors; metal Co and organic QD molecule. By definition the increment of $\Delta\phi$ of up to 0.50 eV on the metal centers indicates electron accumulation and a *symmetric* 0.46 eV decrease of $\Delta\phi$ indicates charge depletion on the molecule. [104]This suggests the balance of charge in such a unperturbed system is accounted for.
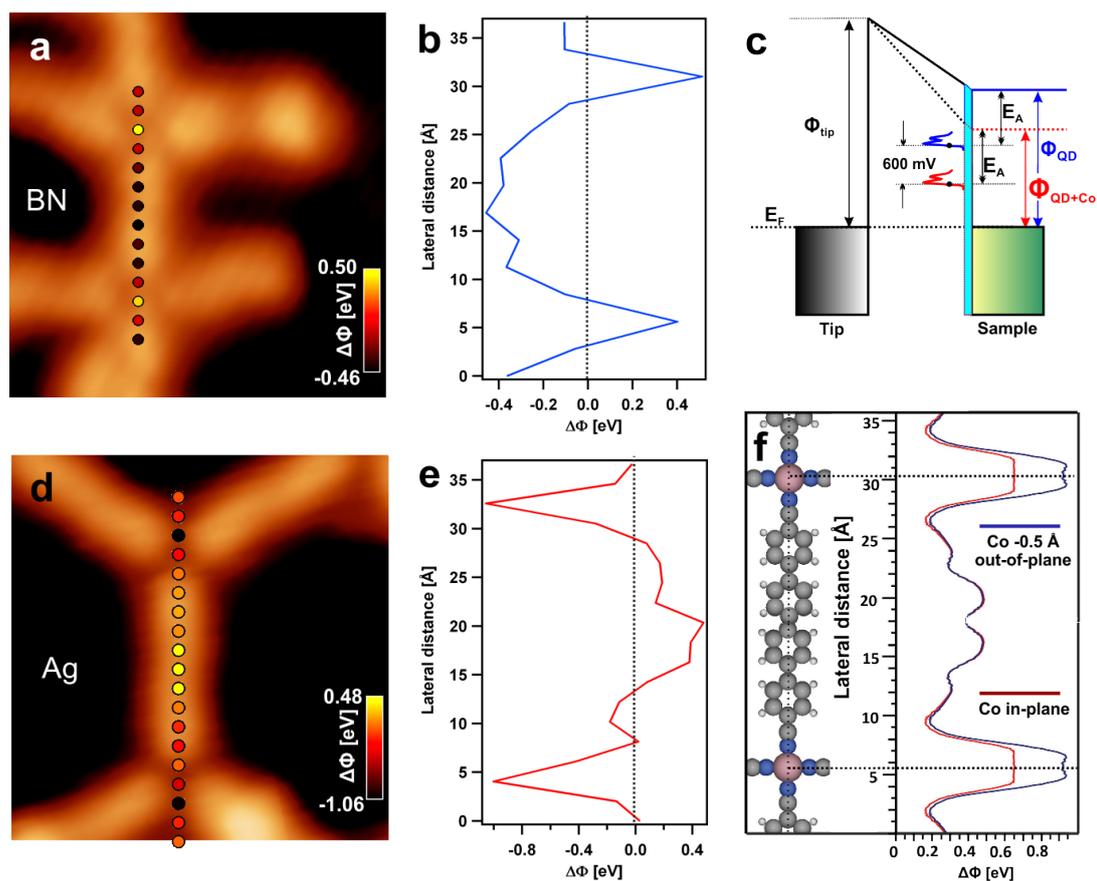
Figure 7.4: Electronic structure of QD-Co frameworks on BN and Ag(111). (a) STM image (V_b = 0.3 V, I = 27 pA) of the QD-Co system on BN with colored points along a line across metal-molecule-metal to characterize $\Delta\phi$. Colored scale bar of $\Delta\phi$ ranging from 0.5 eV to -0.46 eV in the inset. (b) workfunction variation $\Delta\phi$ plot along the line passing through molecular axis between metal centers representing Figure 7.4a. (c) Model sketching the tip-sample interface for free QD (blue vacuum level) with high workfunction and Co-coordinated QD (red vacuum level, dotted) with low workfunction. Accordingly, LUMOs of the Co-coordinated LUMO (red curves) are nearer to the Fermi level as compared to the free QDs on BN. (d) STM image (V_b = 0.2 V, I = 50 pA) of the QD-Co system on Ag(111) with colored points along a line across metal-molecule-metal to characterize . Colored scale bar of ranging from 0.48 eV to -1.06 eV in the inset. (e) Giant modulation of the plotted along the line passing through molecular axis between metal centers representing Figure 7.4d. Sharp reduction of the $\Delta\phi$ observed in the vicinity of the Co center on Ag(111). (f) Theoretical calculation of the workfunction plotted along a free standing metal organic bond simulating the STM measured system on BN which closely matches the trend of $\Delta\phi$ variation. [252]

In Figure 7.3a, STS measured around the center of the QDs with Co-coordination (red) and without Co-coordination (blue) are shown with LUMO resonances around 1.2 V and 1.8 V respectively. Complete profile of the LUMO from Co-coordinated QD was not possible due to tendency of the metal organic bond to break above the 1.2 V. Importantly, for the Co-coordinated QDs the LUMO (red) shifts towards E_F by around 0.6 V on BN. This reduction in LUMO further corroborates the above exhibited $\Delta\phi$ reduction on the molecular backbone. To make it comprehensible see the energy level alignment diagram of Figure 7.4c where both Co-coordinated and free QDs are featured. For both free (blue) and Co-coordinated (red) QDs, we assume constant electron affinity (E_A) from the respective vacuum levels shown here are solid blue line and dotted red line. As the red LUMO level is shifted towards the Fermi level in comparison to blue by 0.6 V, this signifies that the electrons can tunnel into the LUMO at lower bias voltages as compared to free QDs. This corroborates the conjecture above that the Co-coordinated QD is charge depleted and attracts electrons more readily. Moreover, in Figure 7.4c we can see that to keep E_A constant the vacuum level has to decrease as well, thereby reducing the local workfunction of the molecule ϕ_{QD} as compared to a free QD molecule on BN. In turn this reduction of local workfunction ϕ_{QD} is understandably responsible for the reduction (-0.46 eV) of the $\Delta\phi$ as well. [consider the relation $\Delta\phi = 2\,(\phi_{QD} - \phi_{BN})$].

Periodic DFT calculations were used to study the freestanding QD-Co metal organic network with four-fold coordination. The network was first geometrically optimized. workfunction shifts were then extracted from the electrostatic potential, as explained in the methods section (*vide infra*), both for the completely flat network and for a network where the Co has been displaced 0.5 Å below the molecular layer. In principle, the workfunction shift was defined as the shift of the electrostatic barrier height, with respect to the vacuum level. In this definition the local workfunction is basically the local electrostatic potential an electron has to climb to escape the sample. As seen in the figure, the shift for both metal center and the molecular backbone are positive, which is always the case for calculations using a freestanding network with this definition. Only with inclusion of substrate explicitly, herewith the correct reference, the *symmetric* positive and negative shifts we measured can be achievable; which is in itself is another topic of detailed research. Nevertheless, we see that the resulting workfunction shift calculated along a line running along the center of one of the molecules and crossing the Co atoms in Figure 7.4f. Firstly, considering the red curve where the Co is in the molecular plane. The workfunction

shift is largest on the Co atom but not as significant as in the measurements. From our experience in modeling metal organic networks on metal surfaces, the metal center is closer to the surface than the molecules, and me may assume this to be true on BN as well. When displacing the Co atom 0.5 Å below the molecular layer, the workfunction shift increases quite significantly (over 0.9 eV) for the Co (purple curve), and remains constant over the molecule. Now empirically adjusting for the negative shift of the molecules, we can make an estimate that the adjusted increment of the workfunction on Co metal centers would be around 0.4 eV, agreeing reasonably to our measured value. It is nonetheless important to note that the basic model is able to corroborate the main trends observed in experiments.

To further compare the workfunction shift of the metal-ligand system on a traditional Ag(111) system, measurements and extraction of $\Delta\phi$ was performed across a molecule bonded by Co atoms at both ends as seen in Figure 7.4d,e. As mentioned above the trend is exactly opposite to that on the BN and rather *asymmetric* as well with giant decrease of workfunction variation *near* metal atoms (-1.06 eV) and relatively small increment of the $\Delta\phi$ on the molecular backbone (0.48 eV). Upon close inspection, it can be seen that the sharp reduction in $\Delta\phi$ occurs just in the immediate vicinity outside the Co centers. The asymmetry here in the charge rearrangement can be assigned to the presence of metal substrate underneath as an additional actor in the charge redistribution dynamics. Following explanations provided in work from Vitali *et al.* [104] and their study of similar system we can safely assign high charge accumulation atop the Co metal centers and the existence of positive induced dipoles formed due to transfer of electron density from the bonded QDs to the substrate using the metal center as junction or anchoring point. In turn this strong interaction of the QD-Co system and the substrate at the point (Co metal center) is likely to cause sharp electron density displacement in the vicinity. This explains the giant modulation of $\Delta\phi$ just outside the metal junctions. On the other hand, $\Delta\phi$ increases when measured on top on the QD molecule. Unlike on the inert BN, the phenylenes of the QD here on Ag(111) are known to be planar with π interaction. Again similar to the observation in Figure 2b in ref. [253], the slight increment of $\Delta\phi$ above the molecule can be assigned to electron accumulation directly above the aromatic groups.

Lastly, we can safely state that the comparison clarifies the role and type of the substrate for understanding charge distribution dynamics in such a potential molecular wire system. On the decoupling BN in particular, the observation of *sym-*

metric charge variation between Co centers and molecular background gives insight to intrinsic nature of charge accumulation/depletion is a complex network. This could open new avenues to studies and development of molecular wire network array for hosting suitable molecular donor-acceptor complexes. Thus this makes BN on Cu(111) and ever intriguing surface to explore a myriad different phenomenons in nanoscience and functionality thereof.

7.6 Experimental procedures and theoretical methods

The BN surface was prepared by chemical vapor deposition (CVD) of borazine following protocol described in previous chapters and reports. [37, 54, 55] Sub-monolayer coverage of QD molecules were deposited using organic molecular beam epitaxy (OMBE) with the quartz container held at 503 K while the BN/Cu/(111) substrate kept at 293 K. The cobalt metal atoms were sublimated on the sample by resistively heating a cobalt filament placed in the OMBE. The sample temperature was varied between room temperature and 218 K in an attempt to control the growth of the nanostructure. For comparative purpose, the cobalt-coordinated network was also reproduced on Ag(111) following protocol described in previous publications. [16, 17] All STM data were recorded in constant current mode and the dI/dV spectra were taken using a lock-in technique with a bias modulation amplitude of 18 mV rms and a frequency of 969 Hz. The STM images shown in this work are processed using the WSxM software. [120]

Theoretical calculations were done within the framework of periodic density functional theory using the VASP code, [254] using the projector-augmented wave method to describe ion-core interactions. [253] Exchange-correlation effects were described with the generalized gradient approximation using the PBE functional. [255] Plane waves were expanded up to a kinetic energy of 500 eV and the Γ–point only was used to sample the 1st Brillouin zone. QD-Co network was modeled in its freestanding form using the optimized square unit cell of the network of 24.71$\times$24.71 Å^2. To model local workfunction shift we calculated the difference between the largest value of the electrostatic potential along a vertical line through the point of interest and the vacuum level of the overall system.

7.7 Conclusion

In summary, we have presented a detailed STM/STS study covering the formation, characterization and functionalization of Co bonded QD framework on insulating BN/Cu(111). The QD-Co system was shown to form characteristic four-fold coordination motif upon decoupling from metal substrate, supporting a previous DFT prediction. The molecules appear with zigzag features on BN pointing to a non planar conformation due to alternating rotation of phenylene rings. Upon excitation of the LUMO by electron tunneling, the phenylene rings were found to flip between two distinct conformational states; thereby depicting a model functionality of a bistable switch driven by one electron process. As further characterization, the metal-ligand profile on BN was probed with STS showing LUMO shifted towards the Fermi level, together with $\Delta\phi$ extracted from $I(z)$ curves exhibiting a reduced workfunction atop the molecular backbone. Both strongly point to a charge depleted molecule upon bond formation while the Co metal junctions are negatively charged as shown by elevated level. Complementary DFT calculations also show sharp rise in the $\Delta\phi$ on top of the Co junction corroborating the trend. As reference, $\Delta\phi$ profile was also measured for the metal directed QD-Co network on Ag(111) wherein the trends contrasted that on the BN and the local workfunction variation decreased sharply in the vicinity of the Co centers. Following previous similar study on metal substrate [104] the decrease of $\Delta\phi$ was assigned to strong screening and electron depletion in the periphery due to presence of charge accumulating Co centers which act as contact point of strong interaction between the network and the substrate. In conclusion, novel insulting surfaces such as BN are promising substrates for studying metal organic networks and their intrinsic chemistry as well as potential functionalization.

8 Conclusion and Perspectives

This thesis is the final result of a research endeavor in nanoscience with departure from studying molecules and their architectures on well-understood metal surfaces like Cu(111) and Ag(111). Since the Nobel prize for graphene in the year 2010, BN attracted increasing attention as the strongest potential candidate of the wonder material's substrate. However, we began the BN research as part of the search for a suitable decoupling spacer-layer for our studies of molecules, their explorative properties, self-assembly protocols and potential functionalization.

As all of our previous works were done on the well characterized Cu(111) and Ag(111) surfaces, it was only logical to explore the growth of the ultrathin film on one of these substrates. Moreover, detailed STM/STS studies of BN on these layers were simply lacking. For the first part of the research, important research questions, to begin with were: a) What would be the optimum experimental parameters of growth of a sizeable clean surface? b) Would there be an extended surface or several domains within? c) Would the surface be planar or corrugated? The second question was important as domain boundaries hinder the potential growth of extended molecular nano-architectures studied on it. The latter question is particularly interesting as previous results of BN grown on different metal substrates yielded conformations ranging from planar, concave corrugated to convex corrugated (as in the so called nanomesh) in the "hills" area. The mechanism behind these variations was simply lattice mismatches and the interaction between BN and the substrate underneath. The chosen Cu(111) substrate, to begin with, was reported in theoretical studies to have very low binding energy and a small lattice mismatch with BN. Upon measurement, we observed several domains of BN formed on Cu with sizes up to several hundred nanometers in dimension, enough for systematic studies of adsorbates on it. However, due to low binding energy between the spacer-layer and substrate, domains were prone to rotations on the copper surface. Importantly, rotation and the lattice mismatches thereby contributed to moiré patterns of several different periodicities. The moirés were observed at the scanning bias above 4 V with clear "hills" and "val-

leys"; but the BN ultrathin films appeared featureless and planar around normal scanning voltages. Through detailed STS and complementary DFT inspection (in collaboration with the research group in Zurich) of the surface, we established that the BN has a unique topographically planar but electronically corrugated property. The electronic patterning on the BN was attributed to the periodic spatial variation of workfunction across the surface. This is a significant discovery that opened new avenues to not just a decoupled environment for studying our molecular specimen but also to a potential usage of the BN/Cu(111) as a nano-template for functional molecular units, clusters etc.

As further perspectives for future research, detailed comparative growth and study of BN could be done on similar surfaces like Ag, Bi, 2D or other carbon allotropes like graphene and diamond etc. Furthermore, various crystal lattices of the metal substrates other than (111) could also be interesting and could offer novel properties like in the electronically corrugated BN on Cu(111). An important issue that still requires attention is the quest to grow uniform single moiré periodic BN surface on Cu(111), with careful interplay of CVD deposition rates, the temperature of the sample during deposition, cooling rates etc. It's also worthwhile to explore if the moiré size can be engineered or tuned as per requirement.

For further broader perpspectives, the low binding energy between the BN and Cu(111) could be exploited to try and transfer the BN on to other surfaces. Upon gentle contact with the BN containing Cu(111) with another crystal (Ag(111) for instance), BN could in principle be exfoliated by the contact and transferred to the clean surface. It is difficult to grow a clean extended domain of BN monolayer on several surfaces, primarily due to uncontrolled high mobility of the surface atoms at the elevated preparation temperature. Some desired surfaces might even have a melting point lower than the standard CVD temperature required for a good quality BN sheet. We could also imagine trying the famous scotch tape exfoliation technique famously employed with Graphene for the transfer. Also, the growth of BN could be envisaged on monocrystalline silicon with a melting point (1687 K) well above the BN preparation. This could open more doors for various applications in silicon industry, effectively as an alternative for currently employed oxide insulators which are desirably made to be ever thinner. Moreover, a work proving successful integration of BN on silicon would be favorable from the economic perspectives of an already established industry that predominantly uses silicon wafers.

For the second part of the research, BN was deployed as the originally intended spacer-layer using well-studied porphine molecules on it. The 2H-Ps demonstrate interesting repulsive interaction to each other on both Cu and Ag surfaces, with significant influence from the metal substrates. Therefore, the important research questions were: a) How would the porphines react to each other when decoupled? b)What would the intrinsic electronic structure be like? c) Would the electronic corrugation of BN have a templating effect on 2H-P? The porphines are found to form clusters or islands on the BN. Indeed, the metal substrates on previous studies had contributed to the repulsive interaction. As anticipated, the porphines on BN clearly revealed previously elusive HOMO and LUMO resonances in STS. Subsequent STM images at the two resonances revealed the frontier orbitals of the molecules which were also matched with relevant Hückel rendering. Importantly we could also resolve the tautomerization phenomenon with two hydrogen atoms at the molecular core; seen by 90° flipping of the LUMO features. The templating effect of the of the BN was observed starting from very low coverages already with porphines residing on the moiré "hills" exclusively. Upon excitation with electron injection, the molecule was observed to jump around within one moiré cell. Upon coverage increment, they override the templating effect and form a complex chiral Kagomé assembly with periodic holes in the film. STS data revealed an important aspect that the workfunction variation of the underlying BN substrate (across the moiré) is also translated on the adsorbed 2H-Ps as the HOMO-LUMO gap of the molecules varies distinctly depending on their position on moiré. For instance, the LUMO resonances of the porphines moiré "hills" were shifted towards Fermi as compared to ones near the "valley" boundaries. This tunable electronic gap feature of molecules on the electronic corrugation of BN was further elucidated in STM images scanned around LUMO biases. Molecules with pronounced contrast were seen; first on the "hills" and gradually propagating outward. This proved that the BN possesses templating as well and band gap tunability properties for adsorbates, thereby opening more doors for functional nano-architectures and arrays.

As further perspectives related to this part of the research, two aspects could be targeted: templating and band-gap tunability. Countless different functional molecules and metal clusters could be explored for confining on the moiré template. As the surface potential modulation of BN enables band-gap tunability, heterostructure of graphene and other sp^2 layers could be studied. For better control of the experiment direct deposition of smaller graphene components like triangulene etc. could be

done. A direct proof of band gap opening and even their tuning of small graphene patches on the BN would be worthwhile. As an ultrathin insulator, experiments perceiving intercalation of atoms could be interesting. Moreover, growing BN sheet on an already formed molecular network (possibly covalent networks for robustness) could effectively serve the BN as hermetically sealing of packaging layer, useful in potential future applications. Furthermore, studies of porphines or their derivatives with metal centers could be quite elucidating. Experiments with an attempt to change oxidation states of Ce metal atoms on a porphyrin double-decker compound was planned but never tried. This would be an excellent result if successful.

For the third part of the research, QDs were studied on BN as a continuation of an old research series. Conjugated oligophenylenes were extensively studied in our group before using various molecular backbone lengths, metal centers (for metal directed networks) on the two Cu and Ag metal single crystals. Studying QDs on the novel BN substrate led to following research questions: a) Would they be confined on the moirés too? b)What sort of assembly protocols would they follow? c) What effect would the spatial modulation of the underlying substrate have on them? Regardless of the coverage applied the QDs are unaffected by the templating effect of the BN, primarily due to higher inter-molecular interaction and the presence of highly binding carbonitrile groups at the terminals. Compared to their assembly on metal surfaces, the decoupling enables QDs to form a film with chevron assembly. Importantly, the molecules appear with a zigzag shape due to prominent torsion angles (rotations) of phenylene rings. Furthermore, the decoupling effect of the substrate allowed high-resolution STS of the molecules on BN with distinct resonances assigned to two level spatial modulations of vibronic conductance. This was observed in high-resolution STM images as well. With strong support from molecular dynamics and DFT studies, the phenomenon was well understood where first level modulation of conductance at the nanometer scale is a direct impact of the BN's electronic corrugation. Of more importance is resolution and DFT proof of the second level sub nanometer vibronic signature, including the special librational degree of freedom. Indeed, the BN is a unique substrate enabling such experimental and theoretical collaboration to extract such data, which is at the very edge of what is possible with today's instrumentation.

As further recommendations, similar studies could be done with varying lengths of the oligophenylenes as the assembly protocol is directed by the length of the molecules as well. Likewise, similar theoretical studies of films composed of other

different functional molecules would also be interesting. A detailed DFT study of the 2nd net like porous structure is still lacking and definitely would significantly boost our understanding of the vibronic conductance further.

For the last part, QDs were used along with cobalt metal atoms on BN with an endeavor to form a metal-organic network. This was a step further to the work described in the third research segment and would provide additional perspective for the older work done on metal surfaces. Answers that were sought from this segment of research were: a) What would be the size, crystallinity and robustness of the network formed? b) Would the phenylene backbone still exhibit non-planar torsion angles? c) What would be the electronic properties of the metal-coordination on such a decoupled environment? In absence of the metal influence underneath, QDs formed a square network structure with four-fold binding motif at the Co centers, validating an earlier DFT prediction during metal-coordination of QDs on metal substrates. However, large domains of the network could not be formed due to the tendency for Co to prefer formation of clusters on BN. The phenylene rings of the metal coordinated QDs on displayed rotations on BN too with two distinct conformational states "s" and "z". Importantly, we were able to excite the molecules upon electron injection in order to flip the phenylene rings, switching the QDs between the two "s" and "z" states. Further investigation of this phenomenon confirmed this model switch system to be driven by a one-electron process. The metal-ligand system was probed for relative workfunction variation across the metal center and molecular backbone, both on BN and on Ag(111) substrates. This offered a rare insight into charge redistribution of an unperturbed system on BN. Comparative study on Ag(111) produced a rather complex charge redistribution wherein several additional factors like the presence of metal substrate and subsequent formation of dipoles, interaction with the molecular backbone etc come into play. Overall the metal-ligand system opens up a new window for further exploration and functionality of various molecular complexes in nanoscience.

In future, to grow a large domain of Co-QD network, engineering could be done by playing with factors like stoichiometry, the deposition rate of Co metal atoms, the temperature of the sample etc. Moreover, changing the length of the oligophenylenes could also yield clean extended networks of interesting motifs. The above result exhibited that the network coordination binding motif increased from a three-fold to four-fold one due to the presence of BN. Experiments with other metal centers like Ce, Gd could also yield excellent comparative results on top of the current unique

tessellations and 2D quasi-crystalline networks. The bistable switching mechanism of a similar system on the BN could also be delved deeper into for better understanding and potential application.

As a bottomline, BN on Cu(111) is itself a promising new direction for repeating all the experiments ever done using molecules and other adsorbates on metal and other relevant surfaces. This would not only enable us to understand the intrinsic properties of the adsorbates on BN/Cu(111) but would also perhaps promote fascinating novel self-assembly protocols and functionality. In every step, it is a chance to rewrite what we have known so far in nanoscience, enabling us to gain a deeper understanding and better control of matter at the nanoscale.

*Note: Recent followup X-ray standing wave (XSW) and Atomic-force microscopy (AFM) results show that the weakly bound BN have a measurable corrugation on Cu(111).

Bibliography

[1] Valden, M.; Lai, X.; Goodman, D. W. *Science* **1998**, *281*, 1647–1650.

[2] Oliver-Meseguer, J.; Cabrero-Antonino, J. R.; Domínguez, I.; Leyva-Perez, A.; Corma, A. *Science* **2012**, *338*, 1452–1455.

[3] Binnig, G.; Rohrer, H.; Gerber, C.; Weibel, E. *Physical Review Letters* **1983**, *50*, 120–123.

[4] Crommie, M. F.; Lutz, C. P.; Eigler, D. M. *Science* **1993**, *262*, 218–220.

[5] Hla, S.-W.; Bartels, L.; Meyer, G.; Rieder, K.-H. *Physical Review Letters* **2000**, *85*, 2777–2780.

[6] Whitesides, G. M.; Boncheva, M. *Proceedings of the National Academy of Sciences* **2002**, *99*, 4769–4774.

[7] Barth, J. V.; Costantini, G.; Kern, K. *Nature* **2005**, *437*, 671–679.

[8] Barth, J. V. *Annu. Rev. Phys. Chem.* **2007**, *58*, 375–407.

[9] Dmitriev, A.; Spillmann, H.; Lin, N.; Barth, J. V.; Kern, K. *Angewandte Chemie International Edition* **2003**, *115*, 2774–2777.

[10] Stepanow, S.; Lingenfelder, M.; Dmitriev, A.; Spillmann, H.; Delvigne, E.; Lin, N.; Deng, X.; Cai, C.; Barth, J. V.; Kern, K. *Nature Materials* **2004**, *3*, 229–233.

[11] Stepanow, S.; Lin, N.; Barth, J. V.; Kern, K. *The Journal of Physical Chemistry B* **2006**, *110*, 23472–23477.

[12] Heim, D.; Seufert, K.; Auwärter, W.; Aurisicchio, C.; Fabbro, C.; Bonifazi, D.; Barth, J. V. *Nano Letters* **2009**, *10*, 122–128.

[13] Heim, D.; Ecija, D.; Seufert, K.; Auwärter, W.; Aurisicchio, C.; Fabbro, C.; Bonifazi, D.; Barth, J. V. *Journal of the American Chemical Society* **2010**, *132*, 6783–6790.

[14] Ecija, D.; Vijayaraghavan, S.; Auwärter, W.; Joshi, S.; Seufert, K.; Aurisic-chio, C.; Bonifazi, D.; Barth, J. V. *ACS Nano* **2012**, *6*, 4258–4265.

[15] Stepanow, S.; Lin, N.; Payer, D.; Schlickum, U.; Klappenberger, F.; Zoppel-laro, G.; Ruben, M.; Brune, H.; Barth, J. V.; Kern, K. *Angewandte Chemie International Edition* **2007**, *119*, 724–727.

[16] Schlickum, U.; Decker, R.; Klappenberger, F.; Zoppellaro, G.; Klyatskaya, S.; Ruben, M.; Silanes, I.; Arnau, A.; Kern, K.; Brune, H.; V. Barth, J. *Nano Letters* **2007**, *7*, 3813–3817.

[17] Kühne, D.; Klappenberger, F.; Decker, R.; Schlickum, U.; Brune, H.; Kly-atskaya, S.; Ruben, M.; Barth, J. V. *Journal of the American Chemical Society* **2009**, *131*, 3881–3883.

[18] Ecija, D.; Urgel, J. I.; Papageorgiou, A. C.; Joshi, S.; Auwärter, W.; Seitso-nen, A. P.; Klyatskaya, S.; Ruben, M.; Fischer, S.; Vijayaraghavan, S.; Re-ichert, J.; Barth, J. V. *Proceedings of the National Academy of Sciences* **2013**, *110*, 6678–6681.

[19] Grill, L.; Dyer, M.; Lafferentz, L.; Persson, M.; Peters, M. V.; Hecht, S. *Nature Nanotechnology* **2007**, *2*, 687–691.

[20] Krasnikov, S. A.; Doyle, C. M.; Sergeeva, N. N.; Preobrajenski, A. B.; Vino-gradov, N. A.; Sergeeva, Y. N.; Zakharov, A. A.; Senge, M. O.; Cafolla, A. A. *Nano Research* **2011**, *4*, 376–384.

[21] Liljeroth, P.; Repp, J.; Meyer, G. *Science* **2007**, *317*, 1203–1206.

[22] Gross, L.; Mohn, F.; Moll, N.; Liljeroth, P.; Meyer, G. *Science* **2009**, *325*, 1110–1114.

[23] Lin, X.; Nilius, N. *The Journal of Physical Chemistry C* **2008**, *112*, 15325–15328.

[24] Cho, J.; Smerdon, J.; Gao, L.; Suzer, O.; Guest, J. R.; Guisinger, N. P. *Nano Letters* **2012**, *12*, 3018–3024.

[25] Garnica, M.; Stradi, D.; Barja, S.; Calleja, F.; Diaz, C.; Alcami, M.; Mar-tin, N.; de Parga, A. L. V.; Martin, F.; Miranda, R. *Nature Physics* **2013**, *9*, 368–374.

[26] Zhang, H.; Sun, J.; Low, T.; Zhang, L.; Pan, Y.; Liu, Q.; Mao, J.; Zhou, H.; Guo, H.; Du, S.; Guinea, F.; Gao, H.-J. *Physical Review B* **2011**, *84*, 245436.

[27] Berner, S.; Corso, M.; Widmer, R.; Groening, O.; Laskowski, R.; Blaha, P.; Schwarz, K.; Goriachko, A.; Over, H.; Gsell, S.; Schreck, M.; Sachdev, H.; Greber, T.; Osterwalder, J. *Angewandte Chemie International Edition* **2007**, *46*, 5115–5119.

[28] Dil, H.; Lobo-Checa, J.; Laskowski, R.; Blaha, P.; Berner, S.; Osterwalder, J.; Greber, T. *Science* **2008**, *319*, 1824–1826.

[29] Koch, H. P.; Laskowski, R.; Blaha, P.; Schwarz, K. *Physical Review B* **2011**, *84*, 245410.

[30] Wang, B.; Bocquet, M.-L. *The Journal of Physical Chemistry Letters* **2011**, *2*, 2341–2345.

[31] Roth, S.; Matsui, F.; Greber, T.; Osterwalder, J. *Nano Letters* **2013**,

[32] Xue, J.; Sanchez-Yamagishi, J.; Bulmash, D.; Jacquod, P.; Deshpande, A.; Watanabe, K.; Taniguchi, T.; Jarillo-Herrero, P.; LeRoy, B. J. *Nature Materials* **2011**, *10*, 282–285.

[33] Giovannetti, G.; Khomyakov, P. A.; Brocks, G.; Kelly, P. J.; van den Brink, J. *Physical Review B* **2007**, *76*, 073103.

[34] Decker, R.; Wang, Y.; Brar, V. W.; Regan, W.; Tsai, H.-Z.; Wu, Q.; Gannett, W.; Zettl, A.; Crommie, M. F. *Nano Letters* **2011**, *11*, 2291–2295.

[35] Dean, C.; Young, A.; Meric, I.; Lee, C.; Wang, L.; Sorgenfrei, S.; Watanabe, K.; Taniguchi, T.; Kim, P.; Shepard, K.; Hone, J. *Nature Nanotechnology* **2010**, *5*, 722–726.

[36] Britnell, L.; Gorbachev, R. V.; Jalil, R.; Belle, B. D.; Schedin, F.; Katsnelson, M. I.; Eaves, L.; Morozov, S. V.; Mayorov, A. S.; Peres, N. M.; Neto, A. H. C.; Leist, J.; Geim, A. K.; Ponomarenko, L. A.; Novoselov, K. S. *Nano Letters* **2012**, *12*, 1707–1710.

[37] Joshi, S.; Ecija, D.; Koitz, R.; Iannuzzi, M.; Seitsonen, A. P.; Hutter, J.; Sachdev, H.; Vijayaraghavan, S.; Bischoff, F.; Seufert, K.; Barth, J. V.; Auwärter, W. *Nano Letters* **2012**, *12*, 5821–5828.

[38] Binnig, G.; Rohrer, H.; Gerber, C.; Weibel, E. *Applied Physics Letters* **1982**, *40*, 178–180.

[39] Binnig, G.; Rohrer, H.; Gerber, C.; Weibel, E. *Physical Review Letters* **1982**, *49*, 57–61.

[40] Chen, C. J. *Introduction to scanning tunneling microscopy*; Oxford University Press New York, 1993; Vol. 227.

[41] Bonnell, D. A. *Scanning tunneling microscopy and spectroscopy: theory, techniques, and applications*; VCH New York, 1993.

[42] Drakova, D. *Reports on Progress in Physics* **2001**, *64*, 205.

[43] Bardeen, J. *Physical Review Letters* **1961**, *6*, 57–59.

[44] Tersoff, J.; Hamann, D. *Scanning Tunneling Microscopy*; Springer, 1993; pp 59–67.

[45] Tersoff, J.; Hamann, D. *Physical Review Letters* **1983**, *50*, 1998–2001.

[46] Chen, C. J. *Physical Review Letters* **1990**, *65*, 448–451.

[47] Stroscio, J. A.; Feenstra, R.; Newns, D.; Fein, A. *Scanning Tunneling Microscopy*; Springer, 1993; pp 101–109.

[48] Hamers, R. *Annual Review of Physical Chemistry* **1989**, *40*, 531–559.

[49] Lang, N. *Physical Review B* **1988**, *37*, 10395.

[50] Coombs, J.; Gimzewski, J. *Journal of Microscopy* **1988**, *152*, 841–851.

[51] Seufert, K. Surface anchored porphyrins - investigations of assembly, reactivity, manipulation and in-situ synthesis. Ph.D. thesis, Technische Universität München, 2011.

[52] Oura, K.; Lifshits, V. G.; Saranin, A. A.; Zotov, A. V.; Katayama, M.; Yates, J. T. *Physics Today* **2004**, *57*, 79–80.

[53] Zöphel, S. Der aufbau eines tieftemperatur-rastertunnelmikroskops und strukturuntersuchungen auf vicinalen kupferoberflächen. Ph.D. thesis, Freie Universität Berlin, 2000.

[54] Nagashima, A.; Tejima, N.; Gamou, Y.; Kawai, T.; Oshima, C. *Physical Review B* **1995**, *51*, 4606.

[55] Auwärter, W.; Kreutz, T.; Greber, T.; Osterwalder, J. *Surface Science* **1999**, *429*, 229–236.

[56] Oshima, C.; Nagashima, A. *Journal of Physics: Condensed Matter* **1997**, *9*, 1.

[57] Sachdev, H.; Müller, F.; Hüfner, S. *Diamond and Related Materials* **2010**, *19*, 1027–1033.

[58] Shi, Y.; Hamsen, C.; Jia, X.; Kim, K. K.; Reina, A.; Hofmann, M.; Hsu, A. L.; Zhang, K.; Li, H.; Juang, Z.-Y.; S. Dresselhaus, M.; Li, L.-J.; Kong, J. *Nano Letters* **2010**, *10*, 4134–4139.

[59] Kim, K. K.; Hsu, A.; Jia, X.; Kim, S. M.; Shi, Y.; Hofmann, M.; Nezich, D.; Rodriguez-Nieva, J. F.; Dresselhaus, M.; Palacios, T.; Kong, J. *Nano Letters* **2011**, *12*, 161–166.

[60] Zunger, A.; Katzir, A.; Halperin, A. *Physical Review B* **1976**, *13*, 5560.

[61] Watanabe, K.; Taniguchi, T.; Kanda, H. *Nature Materials* **2004**, *3*, 404–409.

[62] Watanabe, K.; Taniguchi, T.; Niiyama, T.; Miya, K.; Taniguchi, M. *Nature Photonics* **2009**, *3*, 591–594.

[63] Ramasubramaniam, A.; Naveh, D.; Towe, E. *Nano Letters* **2011**, *11*, 1070–1075.

[64] Ci, L.; Song, L.; Jin, C.; Jariwala, D.; Wu, D.; Li, Y.; Srivastava, A.; Wang, Z.; Storr, K.; Balicas, L.; Feng, L.; Ajayan, P. M. *Nature Materials* **2010**, *9*, 430–435.

[65] Muntwiler, M.; Auwärter, W.; Seitsonen, A.; Osterwalder, J.; Greber, T. *Physical Review B* **2005**, *71*, 121402.

[66] Corso, M.; Auwärter, W.; Muntwiler, M.; Tamai, A.; Greber, T.; Osterwalder, J. *Science* **2004**, *303*, 217–220.

[67] Bose, S.; Garcia-Garcia, A. M.; Ugeda, M. M.; Urbina, J. D.; Michaelis, C. H.; Brihuega, I.; Kern, K. *Nature Materials* **2010**, *9*, 550–554.

[68] Kahle, S.; Deng, Z.; Malinowski, N.; Tonnoir, C.; Forment-Aliaga, A.; Thontasen, N.; Rinke, G.; Le, D.; Turkowski, V.; Rahman, T. S.; Rauschenbach, S.; Ternes, M.; Kern, K. *Nano Letters* **2011**, *12*, 518–521.

[69] Auwärter, W.; Suter, H. U.; Sachdev, H.; Greber, T. *Chemistry of Materials* **2004**, *16*, 343–345.

[70] Goriachko, A.; He, Y.; Knapp, M.; Over, H.; Corso, M.; Brugger, T.; Berner, S.; Osterwalder, J.; Greber, T. *Langmuir* **2007**, *23*, 2928–2931.

[71] Sutter, P.; Lahiri, J.; Albrecht, P.; Sutter, E. *ACS Nano* **2011**, *5*, 7303–7309.

[72] Müller, F.; Hüfner, S.; Sachdev, H.; Gsell, S.; Schreck, M. *Physical Review B* **2010**, *82*, 075405.

[73] Müller, F.; Hüfner, S.; Sachdev, H.; Laskowski, R.; Blaha, P.; Schwarz, K. *Physical Review B* **2010**, *82*, 113406.

[74] Auwärter, W.; Muntwiler, M.; Osterwalder, J.; Greber, T. *Surface Science* **2003**, *545*, L735–L740.

[75] Morscher, M.; Corso, M.; Greber, T.; Osterwalder, J. *Surface Science* **2006**, *600*, 3280–3284.

[76] Preobrajenski, A.; Vinogradov, A.; Ng, M. L.; Cavar, E.; Westerström, R.; Mikkelsen, A.; Lundgren, E.; Martensson, N. *Physical Review B* **2007**, *75*, 245412.

[77] Corso, M.; Greber, T.; Osterwalder, J. *Surface Science* **2005**, *577*, L78–L84.

[78] Brugger, T.; Günther, S.; Wang, B.; Dil, J. H.; Bocquet, M.-L.; Osterwalder, J.; Wintterlin, J.; Greber, T. *Physical Review B* **2009**, *79*, 045407.

[79] Müller, F.; Hüfner, S.; Sachdev, H. *Surface Science* **2008**, *602*, 3467–3476.

[80] Vinogradov, N. A.; Zakharov, A.; Ng, M.; Mikkelsen, A.; Lundgren, E.; Mårtensson, N.; Preobrajenski, A. *Langmuir* **2012**, *28*, 1775–1781.

[81] Laskowski, R.; Blaha, P.; Schwarz, K. *Physical Review B* **2008**, *78*, 045409.

[82] Preobrajenski, A.; Vinogradov, A.; Martensson, N. *Surface Science* **2005**, *582*, 21–30.

[83] Rokuta, E.; Hasegawa, Y.; Suzuki, K.; Gamou, Y.; Oshima, C.; Nagashima, A. *Physical Review Letters* **1997**, *79*, 4609.

[84] Song, L.; Ci, L.; Lu, H.; Sorokin, P. B.; Jin, C.; Ni, J.; Kvashnin, A. G.; Kvashnin, D. G.; Lou, J.; Yakobson, B. I.; Ajayan, P. M. *Nano Letters* **2010**, *10*, 3209–3215.

[85] Bokdam, M.; Khomyakov, P. A.; Brocks, G.; Zhong, Z.; Kelly, P. J. *Nano Letters* **2011**, *11*, 4631–4635.

[86] Rasool, H. I.; Song, E. B.; Allen, M. J.; Wassei, J. K.; Kaner, R. B.; Wang, K. L.; Weiller, B. H.; Gimzewski, J. K. *Nano Letters* **2010**, *11*, 251–256.

[87] Gao, L.; Guest, J. R.; Guisinger, N. P. *Nano Letters* **2010**, *10*, 3512–3516.

[88] Ogawa, Y.; Hu, B.; Orofeo, C. M.; Tsuji, M.; Ikeda, K.-i.; Mizuno, S.; Hibino, H.; Ago, H. *The Journal of Physical Chemistry Letters* **2012**, *3*, 219–226.

[89] Binnig, G.; Frank, K.; Fuchs, H.; Garcia, N.; Reihl, B.; Rohrer, H.; Salvan, F.; Williams, A. *Physical Review Letters* **1985**, *55*, 991.

[90] Merino, P.; Svec, M.; Pinardi, A. L.; Otero, G.; Martïn-Gago, J. A. *ACS Nano* **2011**, *5*, 5627–5634.

[91] Xhie, J.; Sattler, K.; Ge, M.; Venkateswaran, N. *Physical Review B* **1993**, *47*, 15835.

[92] Hermann, K. *Journal of Physics: Condensed Matter* **2012**, *24*, 314210.

[93] Ćavar, E.; Westerström, R.; Mikkelsen, A.; Lundgren, E.; Vinogradov, A.; Ng, M. L.; Preobrajenski, A.; Zakharov, A.; Mårtensson, N. *Surface Science* **2008**, *602*, 1722–1726.

[94] Paszkowicz, W.; Pelka, J.; Knapp, M.; Szyszko, T.; Podsiadlo, S. *Applied Physics A* **2002**, *75*, 431–435.

[95] Miller, D. L.; Kubista, K. D.; Rutter, G. M.; Ruan, M.; de Heer, W. A.; First, P. N.; Stroscio, J. A. *Physical Review B* **2010**, *81*, 125427.

[96] Hörmandinger, G. *Physical Review B* **1994**, *49*, 13897.

[97] Repp, J.; Meyer, G.; Rieder, K.-H. *Physical Review Letters* **2004**, *92*, 036803.

[98] Hasegawa, Y.; Avouris, P. *Physical Review Letters* **1993**, *71*, 1071–1074.

[99] Reinert, F.; Nicolay, G.; Schmidt, S.; Ehm, D.; Hüfner, S. *Physical Review B* **2001**, *63*, 115415.

[100] Park, J.-Y.; Ham, U.; Kahng, S.-J.; Kuk, Y.; Miyake, K.; Hata, K.; Shigekawa, H. *Physical Review B* **2000**, *62*, R16341.

[101] Ziroff, J.; Gold, P.; Bendounan, A.; Forster, F.; Reinert, F. *Surface Science* **2009**, *603*, 354–358.

[102] Ternes, M.; González, C.; Lutz, C. P.; Hapala, P.; Giessibl, F. J.; Jelínek, P.; Heinrich, A. J. *Physical Review Letters* **2011**, *106*, 016802.

[103] Repp, J. Scanning Tunneling Microscopy and Spectroscopy of Adsorbates on Metal and Insulator Surfaces. Ph.D. thesis, Freie Universität, Berlin, 2002.

[104] Vitali, L.; Levita, G.; Ohmann, R.; Comisso, A.; De Vita, A.; Kern, K. *Nature Materials* **2010**, *9*, 320–323.

[105] Ruggiero, C. D.; Choi, T.; Gupta, J. A. *Applied Physics Letters* **2007**, *91*, 253106–253106.

[106] Ploigt, H.-C.; Brun, C.; Pivetta, M.; Patthey, F.; Schneider, W.-D. *Physical Review B* **2007**, *76*, 195404.

[107] Rienks, E. D.; Nilius, N.; Rust, H.-P.; Freund, H.-J. *Physical Review B* **2005**, *71*, 241404.

[108] Pivetta, M.; Patthey, F.; Stengel, M.; Baldereschi, A.; Schneider, W.-D. *Physical Review B* **2005**, *72*, 115404.

[109] Geim, A. K.; Novoselov, K. S. *Nature Materials* **2007**, *6*, 183–191.

[110] Ma, H.; Brugger, T.; Berner, S.; Ding, Y.; Iannuzzi, M.; Hutter, J.; Osterwalder, J.; Greber, T. *ChemPhysChem* **2010**, *11*, 399–403.

[111] Pollard, A. J.; Perkins, E. W.; Smith, N. A.; Saywell, A.; Goretzki, G.; Phillips, A. G.; Argent, S. P. e. a. *Angewandte Chemie International Edition* **2010**, *49*, 1794–1799.

[112] Barja, S.; Garnica, M.; Hinarejos, J. J.; de Parga, A. L. V.; Martín, N.; Miranda, R. *Chemical Communications* **2010**, *46*, 8198–8200.

[113] N 'Diaye, A. T.; Bleikamp, S.; Feibelman, P. J.; Michely, T. *Physical Review Letters* **2006**, *97*, 215501.

[114] Roos, M.; Künzel, D.; Uhl, B.; Huang, H.-H.; Brandao Alves, O.; Hoster, H. E.; Gross, A.; Behm, R. J. *Journal of the American Chemical Society* **2011**, *133*, 9208–9211.

[115] Nilius, N.; Rienks, E. D.; Rust, H.-P.; Freund, H.-J. *Physical Review Letters* **2005**, *95*, 066101.

[116] Ruffieux, P.; Aït-Mansour, K.; Bendounan, A.; Fasel, R.; Patthey, L.; Gröning, P.; Gröning, O. *Physical Review Letters* **2009**, *102*, 086807.

[117] CreaTec Fischer & Co. GmbH, Germany, http://www.lt-stm.com.

[118] Meyer, G. *Review of scientific instruments* **1996**, *67*, 2960–2965.

[119] Auwärter, W.; Muntwiler, M.; Greber, T.; Osterwalder, J. *Surface Science* **2002**, *511*, 379–386.

[120] Horcas, I.; Fernandez, R.; Gomez-Rodriguez, J.; Colchero, J.; Gómez-Herrero, J.; Baro, A. *Review of Scientific Instruments* **2007**, *78*, 013705.

[121] VandeVondele, J.; Krack, M.; Mohamed, F.; Parrinello, M.; Chassaing, T.; Hutter, J. *Computer Physics Communications* **2005**, *167*, 103–128.

[122] CP2K developers group, CP2K version 2.3 (Development Version), CP2K is freely available from http://www.cp2k.org.

[123] Zhang, Y.; Yang, W. *Physical Review Letters* **1998**, *80*, 890–890.

[124] Grimme, S.; Ehrlich, S.; Goerigk, L. *Journal of Computational Chemistry* **2011**, *32*, 1456–1465.

[125] VandeVondele, J.; Hutter, J. *The Journal of Chemical Physics* **2007**, *127*, 114105.

[126] Goedecker, S.; Teter, M.; Hutter, J. *Physical Review B* **1996**, *54*, 1703.

[127] Stadler, C.; Hansen, S.; Kröger, I.; Kumpf, C.; Umbach, E. *Nature Physics* **2009**, *5*, 153–158.

[128] Diller, K.; Klappenberger, F.; Allegretti, F.; Papageorgiou, A.; Fischer, S.; Wiengarten, A.; Joshi, S.; Seufert, K.; Écija, D.; Auwärter, W.; Barth, J. *The Journal of Chemical Physics* **2013**, *138*, 154710.

[129] Bischoff, F.; Seufert, K.; Auwärter, W.; Joshi, S.; Vijayaraghavan, S.; Ecija, D.; Diller, K.; Papageorgiou, A. C.; Fischer, S.; Allegretti, F.; Duncan, D. A.; Klappenberger, F.; Blobner, F.; Han, R.; Barth, J. V. *ACS Nano* **2013**, *7*, 3139–3149.

[130] Brune, H.; Giovannini, M.; Bromann, K.; Kern, K. *Nature* **1998**, *394*, 451–453.

[131] Gruznev, D.; Matetskiy, A.; Bondarenko, L.; Utas, O.; Zotov, A.; Saranin, A.; Chou, J.; Wei, C.; Lai, M.; Wang, Y. *Nature Communications* **2013**, *4*, 1679.

[132] Qiu, X.; Nazin, G.; Ho, W. *Science* **2003**, *299*, 542–546.

[133] Hirjibehedin, C. F.; Lin, C.-Y.; Otte, A. F.; Ternes, M.; Lutz, C. P.; Jones, B. A.; Heinrich, A. J. *Science* **2007**, *317*, 1199–1203.

[134] Repp, J.; Meyer, G.; Stojković, S. M.; Gourdon, A.; Joachim, C. *Physical Review Letters* **2005**, *94*, 026803–026803.

[135] Wang, Q. H.; Hersam, M. C. *Nature Chemistry* **2009**, *1*, 206–211.

[136] Zhou, H.; Mao, J.; Li, G.; Wang, Y.; Feng, X.; Du, S.; Müllen, K.; Gao, H.-J. *Applied Physics Letters* **2011**, *99*, 153101.

[137] Mao, J.; Zhang, H.; Jiang, Y.; Pan, Y.; Gao, M.; Xiao, W.; Gao, H.-J. *Journal of the American Chemical Society* **2009**, *131*, 14136–14137.

[138] Hämäläinen, S. K.; Stepanova, M.; Drost, R.; Liljeroth, P.; Lahtinen, J.; Sainio, J. *The Journal of Physical Chemistry C* **2012**, *116*, 20433–20437.

[139] Ng, M. L.; Preobrajenski, A.; Zakharov, A.; Vinogradov, A.; Krasnikov, S.; Cafolla, A.; Mårtensson, N. *Physical Review B* **2010**, *81*, 115449.

[140] Natterer, F. D.; Patthey, F.; Brune, H. *Physical Review Letters* **2012**, *109*, 066101.

[141] Milgrom, L. R.; Warren, M. J. *The colours of life: an introduction to the chemistry of porphyrins and related compounds*; Oxford University Press Oxford, 1997.

[142] Kadish, K. M.; Smith, K. M.; Guilard, R. *The Porphyrin Handbook: Inorganic, organometallic and coordination chemistry*; Access Online via Elsevier, 2003; Vol. 3.

[143] Auwärter, W.; Weber-Bargioni, A.; Riemann, A.; Schiffrin, A.; Gröning, O.; Fasel, R.; Barth, J. *The Journal of Chemical Physics* **2006**, *124*, 194708–194708.

[144] Auwärter, W.; Weber-Bargioni, A.; Brink, S.; Riemann, A.; Schiffrin, A.; Ruben, M.; Barth, J. V. *ChemPhysChem* **2007**, *8*, 250–254.

[145] Jung, T.; Schlittler, R.; Gimzewski, J. *Nature* **1997**, *386*, 696–698.

[146] Dyer, M. S.; Robin, A.; Haq, S.; Raval, R.; Persson, M.; Klimes, J. *ACS Nano* **2011**, *5*, 1831–1838.

[147] Stark, M.; Ditze, S.; Drost, M.; Buchner, F.; Steinrück, H.-P.; Marbach, H. *Langmuir* **2013**, *29*, 4104–4110.

[148] Haq, S.; Hanke, F.; Dyer, M. S.; Persson, M.; Iavicoli, P.; Amabilino, D. B.; Raval, R. *Journal of the American Chemical Society* **2011**, *133*, 12031–12039.

[149] Iavicoli, P.; Haq, S.; Amabilino, D. B.; Raval, R. e. a. *Chemical Communications* **2008**, 1536–1538.

[150] Auwärter, W.; Seufert, K.; Bischoff, F.; Ecija, D.; Vijayaraghavan, S.; Joshi, S.; Klappenberger, F.; Samudrala, N.; Barth, J. V. *Nature Nanotechnology* **2011**, *7*, 41–46.

[151] Díaz, J. G.; Ding, Y.; Koitz, R.; Seitsonen, A. P.; Iannuzzi, M.; Hutter, J. *Theoretical Chemistry Accounts* **2013**, *132*, 1–17.

[152] Franke, K.; Schulze, G.; Henningsen, N.; Fernández-Torrente, I.; Pascual, J.; Zarwell, S.; Rück-Braun, K.; Cobian, M.; Lorente, N. *Physical Review Letters* **2008**, *100*, 036807.

[153] Gröning, O.; Fasel, R. *STM generator software, EMPA Materials Science and Technology, Switzerland* **2004**,

[154] Palummo, M.; Hogan, C.; Sottile, F.; Bagalá, P.; Rubio, A. *The Journal of Chemical Physics* **2009**, *131*, 084102.

[155] Dabo, I.; Ferretti, A.; Park, C.-H.; Poilvert, N.; Li, Y.; Cococcioni, M.; Marzari, N. *Physical Chemistry Chemical Physics* **2013**, *15*, 685–695.

[156] Dupuis, P.; Roberge, R.; Sandorfy, C. *Chemical Physics Letters* **1980**, *75*, 434–437.

[157] Qiu, X.; Nazin, G.; Ho, W. *Physical Review Letters* **2004**, *92*, 206102.

[158] Tsai, H.-H.; Simpson, M. C. *The Journal of Physical Chemistry A* **2003**, *107*, 526–541.

[159] Hennig, J.; Limbach, H.-H. *J. Chem. Soc., Faraday Trans. 2* **1979**, *75*, 752–766.

[160] Amar, J. G.; Family, F. *Physical Review Letters* **1995**, *74*, 2066.

[161] Böhringer, M.; Morgenstern, K.; Schneider, W.-D.; Wühn, M.; Wöll, C.; Berndt, R. *Surface Science* **2000**, *444*, 199–210.

[162] Kamna, M.; Graham, T.; Love, J.; Weiss, P. *Surface Science* **1998**, *419*, 12–23.

[163] Torrente, I. F.; Franke, K. J.; Pascual, J. I. *International Journal of Mass Spectrometry* **2008**, *277*, 269–273.

[164] Tseng, T.-C.; Urban, C.; Wang, Y.; Otero, R.; Tait, S. L.; Alcamí, M.; Écija, D. e. a. *Nature Chemistry* **2010**, *2*, 374–379.

[165] Tseng, T.-C.; Abdurakhmanova, N.; Stepanow, S.; Kern, K. *The Journal of Physical Chemistry C* **2011**, *115*, 10211–10217.

[166] Schlickum, U.; Decker, R.; Klappenberger, F.; Zoppellaro, G.; Klyatskaya, S.; Auwärter, W.; Neppl, S.; Kern, K. e. a. *Journal of the American Chemical Society* **2008**, *130*, 11778–11782.

[167] Järvinen, P.; Hämäläinen, S. K.; Banerjee, K.; Häkkinen, P.; Ijäs, M.; Harju, A.; Liljeroth, P. *Nano Letters* **2013**, *13*, 3199–3204.

[168] Torrente, I. F.; Franke, K. J.; Pascual, J. I. *Journal of Physics: Condensed Matter* **2008**, *20*, 184001.

[169] Schiller, F.; Ruiz-Osés, M.; Ortega, J.; Segovia, P.; Martínez-Blanco, J.; Doyle, B.; Pérez-Dieste, V.; Lobo, J.; Néel, N. e. a. *The Journal of Chemical Physics* **2006**, *125*, 144719.

[170] Koitz, R.; Seitsonen, A. P.; Iannuzzi, M.; Hutter, J. *Nanoscale* **2013**,

[171] Joshi, S.; Bischoff, F.; Koitz, R.; Ecija, D.; Seufert, K.; Seitsonen, A. P.; Hutter, J. e. a. *ACS Nano* **2013**, *8*, 430–442.

[172] Childs, H.; Brugger, E.; Bonnell, K.; Meredith, J.; Miller, M.; Whitlock, B.; Max, N. A contract based system for large data visualization. Visualization, 2005. VIS 05. IEEE. 2005; pp 191–198.

[173] Ciesielski, A.; Palma, C.-A.; Bonini, M.; Samorì, P. *Advanced Materials* **2010**, *22*, 3506–3520.

[174] Palma, C.-A.; Samorì, P. *Nature Chemistry* **2011**, *3*, 431–436.

[175] Cai, J.; Ruffieux, P.; Jaafar, R.; Bieri, M.; Braun, T.; Blankenburg, S.; Muoth, M. e. a. *Nature* **2010**, *466*, 470–473.

[176] Lipton-Duffin, J.; Ivasenko, O.; Perepichka, D.; Rosei, F. *Small* **2009**, *5*, 592–597.

[177] Bombis, C.; Ample, F.; Lafferentz, L.; Yu, H.; Hecht, S.; Joachim, C.; Grill, L. *Angewandte Chemie International Edition* **2009**, *48*, 9966–9970.

[178] Gross, L.; Moll, N.; Mohn, F.; Curioni, A.; Meyer, G.; Hanke, F.; Persson, M. *Physical Review Letters* **2011**, *107*, 086101.

[179] Rossel, F.; Pivetta, M.; Patthey, F.; Ćavar, E.; Seitsonen, A. P.; Schneider, W.-D. *Physical Review B* **2011**, *84*, 075426.

[180] Qin, Z.; Liu, C.; Chen, J.; Guo, Q.; Yu, Y.; Cao, G. *The Journal of Chemical Physics* **2012**, *136*, 024701.

[181] McCarthy, K. D.; Prokofev, N.; Tuominen, M. T. *Physical Review B* **2003**, *67*, 245415.

[182] Sergueev, N.; Roubtsov, D.; Guo, H. *Physical Review Letters* **2005**, *95*, 146803.

[183] Seldenthuis, J. S.; Van Der Zant, H. S.; Ratner, M. A.; Thijssen, J. M. *ACS Nano* **2008**, *2*, 1445–1451.

[184] Song, H.; Kim, Y.; Jang, Y. H.; Jeong, H.; Reed, M. A.; Lee, T. *Nature* **2009**, *462*, 1039–1043.

[185] Chang, C. T.-c.; Sethna, J. P.; Pasupathy, A. N.; Park, J.; Ralph, D.; McEuen, P. *Physical Review B* **2007**, *76*, 045435.

[186] Spano, F. C. *Accounts of chemical research* **2009**, *43*, 429–439.

[187] Spano, F. C.; Yamagata, H. *The Journal of Physical Chemistry B* **2010**, *115*, 5133–5143.

[188] Zhang, W.; Govorov, A. O.; Ulloa, S. E. *Physical Review B* **2002**, *66*, 060303.

[189] Pavliček, N.; Swart, I.; Niedenführ, J.; Meyer, G.; Repp, J. *Physical Review Letters* **2013**, *110*, 136101.

[190] Huan, Q.; Jiang, Y.; Zhang, Y.; Ham, U.; Ho, W. *The Journal of Chemical Physics* **2011**, *135*, 014705.

[191] Natterer, F. D.; Patthey, F.; Brune, H. *Physical Review Letters* **2013**, *111*, 175303.

[192] Li, S.; Yu, A.; Toledo, F.; Han, Z.; Wang, H.; He, H.; Wu, R.; Ho, W. e. a. *Physical Review Letters* **2013**, *111*, 146102.

[193] Kim, S.-o.; An, T. K.; Chen, J.; Kang, I.; Kang, S. H.; Chung, D. S.; Park, C. E.; Kim, Y.-H.; Kwon, S.-K. *Advanced Functional Materials* **2011**, *21*, 1616–1623.

[194] Womick, J. M.; Moran, A. M. *The Journal of Physical Chemistry B* **2011**, *115*, 1347–1356.

[195] Scholes, G. D.; Mirkovic, T.; Turner, D. B.; Fassioli, F.; Buchleitner, A. *Energy & Environmental Science* **2012**, *5*, 9374–9393.

[196] Rietveld, H.; Maslen, E.; Clews, C. *Acta Crystallographica Section B: Structural Crystallography and Crystal Chemistry* **1970**, *26*, 693–706.

[197] Karabunarliev, S.; Bittner, E. R.; Baumgarten, M. *The Journal of Chemical Physics* **2001**, *114*, 5863–5870.

[198] Heimel, G.; Daghofer, M.; Gierschner, J.; List, E. J.; Grimsdale, A. C.; Müllen, K.; Beljonne, D.; Brédas, J.-L.; Zojer, E. *The Journal of Chemical Physics* **2005**, *122*, 054501.

[199] Coropceanu, V.; Cornil, J.; da Silva Filho, D. A.; Olivier, Y.; Silbey, R.; Brédas, J.-L. *Chemical Reviews* **2007**, *107*, 926–952.

[200] Venkateshvaran, D.; Nikolka, M.; Sadhanala, A.; Lemaur, V.; Zelazny, M.; Kepa, M.; Hurhangee, M. e. a. *Nature* **2014**, *515*, 384–388.

[201] Hodgson, A.; Haq, S. *Surface Science Reports* **2009**, *64*, 381–451.

[202] Odelius, M.; Bernasconi, M.; Parrinello, M. *Physical Review Letters* **1997**, *78*, 2855.

[203] Morawitz, H.; Koehler, T. *Chemical Physics Letters* **1980**, *71*, 64–67.

[204] Brown, R. D.; Hund, Z. M.; Campi, D.; OLeary, L. E.; Lewis, N. S.; Bernasconi, M.; Benedek, G.; Sibener, S. *Physical Review Letters* **2013**, *110*, 156102.

[205] Schaffert, J.; Cottin, M. C.; Sonntag, A.; Karacuban, H.; Bobisch, C. A.; Lorente, N.; Gauyacq, J.-P.; Möller, R. *Nature Materials* **2013**, *12*, 223–227.

[206] Klappenberger, F.; Kühne, D.; Marschall, M.; Neppl, S.; Krenner, W.; Nefedov, A.; Strunskus, T. e. a. *Advanced Functional Materials* **2011**, *21*, 1631–1642.

[207] France, C.; Frame, F. A.; Parkinson, B. *Langmuir* **2006**, *22*, 7507–7511.

[208] Krenner, W.; Klappenberger, F.; Kepcija, N.; Arras, E.; Makoudi, Y.; Kühne, D.; Klyatskaya, S.; et al., *The Journal of Physical Chemistry C* **2012**, *116*, 16421–16429.

[209] Arras, E.; Seitsonen, A. P.; Klappenberger, F.; Barth, J. V. *Physical Chemistry Chemical Physics* **2012**, *14*, 15995–16001.

[210] Palma, C.-A.; Joshi, S.; Hoh, T.; Ecija, D.; Barth, J. V.; Auwärter, W. *Nano Letters* **2015**, *15*, 2242–2248.

[211] Ruiz, V. G.; Liu, W.; Zojer, E.; Scheffler, M.; Tkatchenko, A. *Physical Review Letters* **2012**, *108*, 146103.

[212] Björk, J.; Stafström, S.; Hanke, F. *Journal of the American Chemical Society* **2011**, *133*, 14884–14887.

[213] Björk, J.; Hanke, F.; Palma, C.-A.; Samori, P.; Cecchini, M.; Persson, M. *The Journal of Physical Chemistry Letters* **2010**, *1*, 3407–3412.

[214] Hod, O. *Journal of Chemical Theory and Computation* **2012**, *8*, 1360–1369.

[215] Weiss, E. A.; Ahrens, M. J.; Sinks, L. E.; Gusev, A. V.; Ratner, M. A.; Wasielewski, M. R. *Journal of the American Chemical Society* **2004**, *126*, 5577–5584.

[216] Moneo, Á.; Carvalho, M.; Telo, J. P. *Journal of Physical Organic Chemistry* **2012**, *25*, 559–565.

[217] Repp, J.; Liljeroth, P.; Meyer, G. *Nature Physics* **2010**, *6*, 975–979.

[218] van der Lit, J.; Boneschanscher, M. P.; Vanmaekelbergh, D.; Ijäs, M.; Uppstu, A.; Ervasti, M.; Harju, A.; Liljeroth, P.; Swart, I. *Nature Communications* **2013**, *4*.

[219] Nazin, G.; Wu, S.; Ho, W. *Proceedings of the National Academy of Sciences of the United States of America* **2005**, *102*, 8832–8837.

[220] Cornil, J.; Beljonne, D.; Shuia, Z.; Hagler, T.; Campbell, I.; Bradley, D.; Brédas, J.; Spangler, C.; Müllen, K. *Chemical Physics Letters* **1995**, *247*, 425–432.

[221] Pradhan, N. A.; Liu, N.; Ho, W. *The Journal of Physical Chemistry B* **2005**, *109*, 8513–8518.

[222] Karabunarliev, S.; Baumgarten, M.; Bittner, E. R.; Müllen, K. *The Journal of Chemical Physics* **2000**, *113*, 11372–11381.

[223] Plasser, F.; Barbatti, M.; Aquino, A. J.; Lischka, H. *Theoretical Chemistry Accounts* **2012**, *131*, 1–14.

[224] Granovsky, A. A. *URL: http://classic. chem. msu. su/gran/firefly/index. html* **2014**,

[225] Adamo, C.; Barone, V. *The Journal of Chemical Physics* **1999**, *110*, 6158–6170.

[226] Laurent, A. D.; Jacquemin, D. *International Journal of Quantum Chemistry* **2013**, *113*, 2019–2039.

[227] Néel, N.; Kroger, J.; Berndt, R. *Nano Letters* **2011**, *11*, 3593–3596.

[228] Lotze, C.; Corso, M.; Franke, K. J.; von Oppen, F.; Pascual, J. I. *Science* **2012**, *338*, 779–782.

[229] Jenekhe, S. A. e. a. *Excimers and exciplexes of conjugated polymers*; 1994.

[230] Hipps, K.; Mazur, U. *Journal of the American Chemical Society* **1987**, *109*, 3861–3865.

[231] Secker, D.; Wagner, S.; Ballmann, S.; Härtle, R.; Thoss, M.; Weber, H. B. *Physical Review Letters* **2011**, *106*, 136807.

[232] Schulz, F.; Drost, R.; Hämäläinen, S. K.; Liljeroth, P. *ACS Nano* **2013**, *7*, 11121–11128.

[233] Wingreen, N. S.; Jacobsen, K. W.; Wilkins, J. W. *Physical Review B* **1989**, *40*, 11834.

[234] Härtle, R.; Benesch, C.; Thoss, M. *Physical Review B* **2008**, *77*, 205314.

[235] Mugarza, A.; Lorente, N.; Ordejón, P.; Krull, C.; Stepanow, S.; Bocquet, M.-L.; Fraxedas, J.; Ceballos, G.; Gambardella, P. *Physical Review Letters* **2010**, *105*, 115702.

[236] Halgren, T. A. *Journal of Computational Chemistry* **1999**, *20*, 720–729.

[237] Brooks, B. R.; Brooks, C. L.; MacKerell, A. D.; Nilsson, L.; Petrella, R. J.; Roux, B.; Won, Y. e. a. *Journal of Computational Chemistry* **2009**, *30*, 1545–1614.

[238] Ryckaert, J.-P.; Ciccotti, G.; Berendsen, H. J. *Journal of Computational Physics* **1977**, *23*, 327–341.

[239] Schmidt, M. W.; Baldridge, K. K.; Boatz, J. A.; Elbert, S. T.; Gordon, M. S.; Jensen, J. H.; Koseki, S.; Matsunaga, N. e. a. *Journal of Computational Chemistry* **1993**, *14*, 1347–1363.

[240] Barth, J. V. *Surface Science* **2009**, *603*, 1533–1541.

[241] Lafferentz, L.; Ample, F.; Yu, H.; Hecht, S.; Joachim, C.; Grill, L. *Science* **2009**, *323*, 1193–1197.

[242] Zhang, Y.-Q.; Kepčija, N.; Kleinschrodt, M.; Diller, K.; Fischer, S.; Papageorgiou, A. C.; Allegretti, F. e. a. *Nature Communications* **2012**, *3*, 1286.

[243] Tait, S. L.; Langner, A.; Lin, N.; Stepanow, S.; Rajadurai, C.; Ruben, M.; Kern, K. *The Journal of Physical Chemistry C* **2007**, *111*, 10982–10987.

[244] Clair, S.; Pons, S.; Fabris, S.; Baroni, S.; Brune, H.; Kern, K.; Barth, J. V. *The Journal of Physical Chemistry B* **2006**, *110*, 5627–5632.

[245] Matena, M.; Björk, J.; Wahl, M.; Lee, T.-L.; Zegenhagen, J.; Gade, L. H.; Jung, T. A.; Persson, M.; Stöhr, M. *Physical Review B* **2014**, *90*, 125408.

[246] Stepanow, S.; Lin, N.; Barth, J. V. *Journal of Physics: Condensed Matter* **2008**, *20*, 184002.

[247] Marschall, M.; Reichert, J.; Weber-Bargioni, A.; Seufert, K.; Auwärter, W.; Klyatskaya, S.; Zoppellaro, G.; Ruben, M.; Barth, J. V. *Nature Chemistry* **2010**, *2*, 131–137.

[248] Urgel, J. I.; Ecija, D.; Auwärter, W.; Papageorgiou, A. C.; Seitsonen, A. P.; Vijayaraghavan, S.; Joshi, S. e. a. *The Journal of Physical Chemistry C* **2014**, *118*, 12908–12915.

[249] Urgel, J. I.; Schwarz, M.; Garnica, M.; Stassen, D.; Bonifazi, D.; Ecija, D.; Barth, J. V.; Auwärter, W. *Journal of the American Chemical Society* **2015**, *137*, 2420–2423.

[250] Kaposi, T.; Joshi, S.; Hoh, T.; Wiengarten, A.; Seufert, K.; Paszkiewicz, M.; Klappenberger, F.; Ecija, D. e. a. *ACS Nano* **2016**, *10*, 7665–7674.

[251] Abel, M.; Clair, S.; Ourdjini, O.; Mossoyan, M.; Porte, L. *Journal of the American Chemical Society* **2010**, *133*, 1203–1205.

[252] Joshi, S.; Hoh, T.; Ecija, D.; Björk, J.; Barth, J. V.; Auwärter, W. *To be submitted* **2017**,

[253] Blöchl, P. E. *Physical Review B* **1994**, *50*, 17953.

[254] Kresse, G.; Furthmüller, J. *Physical Review B* **1996**, *54*, 11169.

[255] Perdew, J. P.; Burke, K.; Ernzerhof, M. *Physical Review Letters* **1996**, *77*, 3865.

List of Publications

1. Willi Auwärter, Knud Seufert, Felix Bischoff, David Ecija, Saranyan Vijayaraghavan, Sushobhan Joshi, Florian Klappenberger, Niveditha Samudrala & Johannes V. Barth. *"A surface-anchored molecular four-level conductance switch based on single proton transfer."* Nature nanotechnology, 2011, 7, 41–46.

2. Sushobhan Joshi, David Ecija, Ralph Koitz, Marcella Iannuzzi, Ari P Seitsonen, Jürg Hutter, Hermann Sachdev, Saranyan Vijayaraghavan, Felix Bischoff, Knud Seufert, Johannes V. Barth, Willi Auwärter. *"Boron Nitride on Cu(111): An Electronically Corrugated Monolayer."* Nano letters, 2012, 12, 5821–5828.

3. David Ecija, Saranyan Vijayaraghavan, Willi Auwärter, Sushobhan Joshi, Knud Seufert, Claudia Aurisicchio, Davide Bonifazi, Johannes V. Barth. *"Two-dimensional short-range disordered crystalline networks from flexible molecular modules."* ACS Nano 2012, 6, 4258–4265.

4. Saranyan Vijayaraghavan, David Écija, Willi Auwärter, Sushobhan Joshi, Knud Seufert, Ari P Seitsonen, Kentaro Tashiro, Johannes V. Barth. *"Selective Supramolecular Fullerene–Porphyrin Interactions and Switching in Surface-Confined C60–Ce (TPP) 2 Dyads."* Nano letters, 2012, 12, 4077–4083.

5. David Écija, José I Urgel, Anthoula C Papageorgiou, Sushobhan Joshi, Willi Auwärter, Ari P Seitsonen, Svetlana Klyatskaya, Mario Ruben, Sybille Fischer, Saranyan Vijayaraghavan, Joachim Reichert, Johannes V. Barth. *"Five-vertex Archimedean surface tessellation by lanthanide-directed molecular self-assembly."* PNAS, 2013, 110, 6678-6681.

6. Felix Bischoff, Knud Seufert, Willi Auwärter, Sushobhan Joshi, Saranyan Vijayaraghavan, David Ecija, Katharina Diller, Anthoula C Papageorgiou, Sybille Fischer, Francesco Allegretti, David A Duncan, Florian Klappenberger, Florian Blobner, Runyuan Han, Johannes V. Barth. *"How surface bonding and*

repulsive interactions cause phase transformations: Ordering of a prototype macrocyclic compound on Ag (111)." ACS Nano, 2013, 7, 3139–3149.

7. Saranyan Vijayaraghavan, David Ecija, Willi Auwärter, Sushobhan Joshi, Knud Seufert, Mateusz Drach, Damian Nieckarz, Paweł Szabelski, Claudia Aurisicchio, Davide Bonifazi, Johannes V. Barth. *"Supramolecular Assembly of Interfacial Nanoporous Networks with Simultaneous Expression of Metal–Organic and Organic-Bonding Motifs."* Chemistry–A European Journal, 2013, 19, 14143-14150.

8. Knud Seufert, Willi Auwärter, FJ García de Abajo, David Ecija, Saranyan Vijayaraghavan, Sushobhan Joshi, Johannes V. Barth. *"Controlled interaction of surface quantum-well electronic states."* Nano letters, 2013, 13, 6130-6135.

9. Katharina Diller, Florian Klappenberger, Francesco Allegretti, Anthoula C Papageorgiou, Sybille Fischer, Alissa Wiengarten, Sushobhan Joshi, Knud Seufert, David Écija, Willi Auwärter, Johannes V. Barth. *"Investigating the molecule-substrate interaction of prototypic tetrapyrrole compounds: Adsorption and self-metalation of porphine on Cu(111)."* The Journal of chemical physics, 2013, 138, 154710.

10. Sushobhan Joshi, Felix Bischoff, Ralph Koitz, David Ecija, Knud Seufert, Ari Paavo Seitsonen, Jürg Hutter, Katharina Diller, José I Urgel, Hermann Sachdev, Johannes V. Barth, Willi Auwärter. *"Control of molecular organization and energy level alignment by an electronically nanopatterned boron nitride template."* ACS Nano, 2014, 8, 430–442.

11. José I Urgel, David Ecija, Willi Auwärter, Anthoula C Papageorgiou, Ari P Seitsonen, Saranyan Vijayaraghavan, Sushobhan Joshi, Sybille Fischer, Joachim Reichert, Johannes V. Barth. *"Five-vertex lanthanide coordination on surfaces: A route to sophisticated nanoarchitectures and tessellations."* The Journal of Physical Chemistry C, 2014, 118, 12908-12915.

12. Carlos-Andres Palma*, Sushobhan Joshi*, Tobias Hoh, David Ecija, Johannes V. Barth, Willi Auwärter. *"Two-Level Spatial Modulation of Vibronic Conductance in Conjugated Oligophenylenes on Boron Nitride."* Nano letters, 2015, 15, 2242-2248. *Equally contributing authors.

13. Tobias Kaposi, Sushobhan Joshi, Tobias Hoh, Alissa Wiengarten, Knud Seufert, Matheusz Paszkiewicz, Florian Klappenberger, David Ecija, Luka Đorđević,

Tomas Marangoni, Davide Bonifazi, Johannes V. Barth, Willi Auwärter. *"Supramolecular Spangling, Crocheting, and Knitting of Functionalized Pyrene Molecules on a Silver Surface."* ACS Nano, 2016, 10, 7665-7674.

14. Sushobhan Joshi, Tobias Hoh, David Ecija, Jonas Björk, Johannes V. Barth and Willi Auwärter. *"Formation, characterization and functionalization of cobalt-coordinated structure of quaterphenyl dicarbonitriles on boron nitride/Cu(111)."* (To be submitted)

Acknowledgements

First and foremost, I would like to thank Prof. Dr. Johannes V. Barth for giving me this opportunity to embark on the PhD journey. His guidance and utmost understanding during the whole period will be remembered as an example in my life. I would also like to greatly thank my supervisor Prof. Dr. Willi Auwärter for his invaluable support during stay at E20. BN was an unchartered research topic at the E20 and the LT-STM group, shaking up some initial confidence. However, with Willi's exemplary supervision, profound knowledge and ideas that he shared, the level of work presented here in this thesis became possible. I am also grateful for his tireless willingness to support me with answers to my questions, publications and conferences. I am extremely grateful to Dr. David Écija for introducing me to the STM. He was always there to help me with whatever questions I had regarding the research work as well as operations and maintenance of the STM.

Next, I thank my lab colleagues and friends Dr. Saranyan Vijayraghavan, Dr. Knud Seufert, Dr. Alissa Wiengarten, Dr. Jose Ignacio Urgel and Felix Bischof for sharing those friendly moments, knowledge sharing and help. You guys made my stay at the lab very prolific. I fortunately got to supervise Tobias Hoh's Bachelor thesis during my PhD. He is a gentle and capable student with whom much of the experiments and results presented in this PhD thesis were done. I thank him for his efforts.

I also would like to remember the enjoyable times I spent at E20 with amazing friends like Dr. Katharina Diller, Dr. Andreas Kim, Dr. Sybille Fischer, Dr. Nenad Kepcija, Dr. Raphael Hellwig and Peter Weber. Thank you guys for being there. Likewise, I also want to thank Dr. Hartmut Schlichting, Dr. Florian Klappenberger, Dr. Carlos Andres Palma and Dr. Anthoula Papageorgiou and Dr. Yiqi Zhang for the knowledge and support they offered whenever I needed. Also, I would like to thank my roommates Max and Borja with whom I had those refreshing talks and comradery. Karl Eberle is also a very helpful gentleman who I could always turn to for any technical help. Similarly, I want to thank Kamila Wilson and Viktoria